# Influence of Hot Carriers on Spin Diffusion in Gallium Arsenide

Dissertation zur Erlangung des naturwissenschaftlichen Doktorgrades der Julius-Maximilians-Universität Würzburg

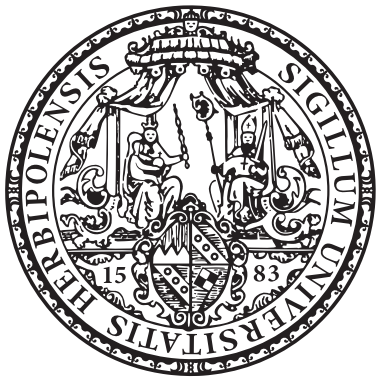


vorgelegt von
Jan-Henrik Quast
aus Lemgo

Würzburg, 2016

Eingereicht am 18. Juli 2016
bei der Fakultät für Physik und Astronomie

1. Gutachter: Prof. Dr. W. Ossau
2. Gutachter: Prof. Dr. J. Geurts
3. Gutachter: .....

der Dissertation

Vorsitzende(r): Prof. Dr. M. Kadler

1. Prüfer: Prof. Dr. W. Ossau
2. Prüfer: Prof. Dr. J. Geurts
3. Prüfer: Prof. Dr. H. Hinrichsen

im Promotionskolloquium

Tag des Promotionskolloquiums: 9. März 2017

Doktorurkunde ausgehändigt am: .....

# Zusammenfassung

Seit dem späten 20. Jahrhundert hat sich die sogenannte *Spintronik* zu einem sehr aktiven Forschungsgebiet entwickelt [ŽFS04]. Die Aussichten auf eine Spin-basierte Informationsverarbeitung mit stark reduziertem Energieverbrauch und eventuell möglichen Quantenrechenfähigkeiten hat das Forschungsinteresse erheblich angeheizt. Standard-Halbleiter-Materialien wie Galliumarsenid (GaAs) erfuhren in diesem Zusammenhang neue Aufmerksamkeit auf Grund von außergewöhnlich langen Lebensdauern für Nichtgleichgewichts-Spins, welche eine wichtige Voraussetzung für eine effiziente Spin-basierte Speicherung und Übertragung von Informationen darstellt. Weitere wichtige Faktoren sind die Distanz über die Spin-Information in einem gegebenen Material transportiert werden kann sowie die Rolle von äußeren Einflüssen. Beide Aspekte wurden experimentell mit innovativen optischen Methoden seit den späten 1990er Jahren durch die Gruppen von D. D. AWSHALOM und S. A. CROOKER untersucht [KA99, CS05, CFL$^+$05]. Obwohl diese zukunftsweisenden experimentellen Ansätze zu einer Vielzahl von Einsichten in die Ausbreitung und Dynamik von Nichtgleichgewichts-Spins führten, wurden auch einige Fragen aufgeworfen. Am deutlichsten fiel auf, dass die Einsteinsche Beziehung zwischen Mobilität und Diffusivität für Elektronenspins in einem Volumenhalbleiter verletzt zu sein scheint. Stark vereinfacht gesagt, scheinen Nichtgleichgewichts-Spins schneller zu diffundieren als sich die dazugehörigen Elektronen bewegen können. Dieser Widerspruch könnte allerdings auch daher stammen, dass das hier untersuchte Material $n$-Typ GaAs mit Dotier-Konzentrationen direkt am Metall-Isolator-Übergang war. In diesem Bereich ist die korrekte experimentelle Bestimmung der Elektronenbeweglichkeit aus praktischen Gründen schwierig. Folglich konnte nicht von vornherein der Schluss gezogen werden, dass die mit den neuen optischen Methoden bestimmten Spindiffusionsraten tatsächlich im Widerspruch zu etablierten elektrischen Transportdaten standen. Es gab somit keinen unmittelbaren Grund, die quantitativen Ergebnisse in Frage zu stellen.

Bei dem Versuch, die Datenlage zur optischen Spin-Mikroskopie an GaAs systematisch zu erweitern, hat sich allerdings gezeigt, dass die mathematisch-numerische Drift-Diffusions-Analyse, die gemeinhin verwendet wurde um laterale Spindichte-Messungen auszuwerten, grundlegende Probleme aufweist. Eine genaue Analyse der Thematik hat ergeben, dass das verwendete Modell bei sehr tiefen Temperaturen nur bedingt anwendbar ist (Kapitel 4). Dies äußert sich zum Beispiel in den oben erwähnten Publikationen bereits durch deutlich sichtbare Abweichungen zwischen dem Modell und den experimentellen Daten. In der vorliegenden Arbeit wird gezeigt, dass diese Diskrepanzen durch eine lokale Überhitzung der Leitungsband-Elektronen hervorgerufen wird, wie sie bei optischen Band-Band-Anregungen kaum zu vermeiden ist. Mit Hilfe von Erkenntnissen aus der zweiten Hälfte des 20. Jahrhunderts wird rekapituliert, warum Leitungselektronen bei kryogenen Temperaturen durch optische Anregung extrem leicht überhitzt werden. Der Grund dafür ist die schlechte thermische Kopplung zwischen den Elektronen und dem Kristallgitter (Kapitel 3). Außerdem wird experimentell direkt gezeigt, dass unter lokaler optischer Anregung von Elektron–Loch-Paaren deutliche thermische Gradienten im Leitungsband entstehen. Die daraus gewonnenen Informationen werden anschließend verwendet, um das mathematische Diffusionsmodell für die Auswertung optischer Spin-Mikroskopie-Daten zu verbessern. Dies ermöglichte schließlich, die Diffusion von Nichtgleichgewichts-Spins im Leitungsband über einen weiten Temperatur- und Dotierdichtebereich am Metall-Isolator-Übergang

zu untersuchen (Kapitel 4.4).

Die in dieser Arbeit vorgestellten Experimente wurden an einer Reihe von $n$-Typ Volumen-GaAs Proben mit Dotierdichten zwischen $7 \times 10^{15}\,\mathrm{cm}^{-3}$ und $7 \times 10^{16}\,\mathrm{cm}^{-3}$ bei Badtemperaturen zwischen $5\,\mathrm{K}$ und $40\,\mathrm{K}$ durchgeführt. Die lokale Elektronentemperatur wurde mit Hilfe verschiedener bildgebender Methoden vermessen, die auf der Photolumineszenz-Messung des Elektron–Akzeptor-Übergangs (e, $A^0$) basieren. Ortsaufgelöste Spindichte-Messungen wurden mit Hilfe der abrasternden magneto-optischen Kerr-Mikroskopie vorgenommen. Die numerische Auswertung basiert größtenteils auf der Finite-Elemente-Methode in Kombination mit der iterativen Anpassung der Modelle durch die Minimierung der quadratischen Abweichung. Die Arbeit ist wie folgt strukturiert.

Die Einleitung in Kapitel 1 fasst einige zurückliegende Forschungsergebnisse und Erkenntnisse zusammen, die für das Verständnis der vorliegenden Arbeit relevant sind. In Kapitel 2 werden anschließend grundlegende physikalische Konzepte erläutert, die für die nachfolgenden Erörterungen von Bedeutung sind. Insbesondere werden hier die Themen Halbleiter-Optik, Relaxation heißer Leitungselektronen und die dynamischen Eigenschaften von Nichtgleichgewichts-Elektronenspins in Halbleitern sowie die dazugehörigen experimentellen Methoden und Techniken diskutiert.

Kapitel 3 thematisiert die Heizwirkung, die sich bei lokaler optischer Anregung von Elektron–Loch-Paaren ergibt. Experimentelle Untersuchungen der Photolumineszenz von Akzeptor-gebundenen Exzitonen führen zu dem Schluss, dass das Kristallgitter in der Regel nicht signifikant überhitzt wird. Dies gilt auch bei relativ hohen Anregungsdichten, da die eingetragene Wärme auf Grund der guten Wärmeleitfähigkeit des Gitters effizient im Kristall verteilt und zum Wärmebad abgeführt wird. Des Weiteren wird der Wärmeeintrag ins Gitter durch die schlechte thermische Kopplung der Elektronen zum Gitter beschränkt. Dies ist zugleich auch der Grund, warum die Leitungsband-Elektronen bei Temperaturen unterhalb von ca. $30\,\mathrm{K}$ sehr leicht überhitzen können. Die räumlich-spektrale Abbildung der Photolumineszenz des Elektron–Akzeptor-Übergangs erlaubt es hier, den räumlichen Temperaturverlauf innerhalb des Leitungsbandes unter fokussierter Laseranregung sichtbar zu machen. Ein Wärmetransport-Modell wird formuliert, das bei niedrig dotierten GaAs Proben den experimentellen Verlauf der Elektronentemperatur gut wiedergibt. Bei hochdotierten Proben kann der räumliche Temperaturverlauf allerdings auch sehr gut durch eine Gauß-Kurve beschrieben werden. Diese Näherung hat den praktischen Vorteil, dass sie sich auf handhabbare Weise mit dem mathematisch Modell zur Beschreibung der Spindiffusion verbinden lässt.

Kapitel 4 befasst sich mit magneto-optischer Bildgebung von optisch induzierten Nichtgleichgewichts-Leitungselektronen-Spins in $n$-Typ GaAs am Metall-Isolator-Übergang. Zuerst wird die spektrale Abhängigkeit des magneto-optischen Kerr-Effekts in der spektralen Umgebung der Fundamentalbandlücke untersucht. Es wird gezeigt, dass trotz der deutlichen Unterschiede zwischen den untersuchten Proben die spektrale Form in allen Fällen sehr gut mit einem einfachen Lorentz-Oszillator-Modell angenähert werden kann. Basierend auf diesem Modell wird die Linearität des Kerr-Effekts in Bezug auf den Grad der Spinpolarisation untersucht, was für eine quantitative Auswertungen von entscheidender Bedeutung ist.

Des Weiteren wird in Kapitel 4 eine umfangreiche experimentelle Untersuchung von Spin-Relaxationszeiten in $n$-Typ GaAs am Metall-Isolator-Übergang vorgestellt. Dabei wurde die Abhängigkeit der Spinrelaxationszeit von der Badtemperatur und der Dotierungsdichte mit Hilfe von Hanle-MOKE Messungen ermittelt. Alle beobachteten Trends stimmen gut mit publizierten Daten überein, erwei-

tern jedoch die vorhandene Datenlage erstmals um einen zusammenhängenden Datensatz, der einen großen Temperatur- und Dotierdichtebereich abdeckt.

Zu guter Letzt wird die Diffusion von optisch erzeugten Nichtgleichgewichts-Leitungselektronen-Spins durch abrasternde MOKE-Mikroskopie untersucht. Hier wird erstmals gezeigt, dass das Standard-Diffusions-Modell in bestimmten Situationen nicht zur Auswertung verwendet werden kann. Eine systematische Übersicht über die Abweichungen zwischen diesem Modell und den experimentellen Daten zeigt, dass dies leider in einigen der oben erwähnten Veröffentlichungen der Fall ist. Des Weiteren deutet die Temperaturabhängigkeit der Abweichungen auf einen engen Zusammenhang zur lokalen Überhitzung der Leitungselektronen hin. Basierend darauf wird ein modifiziertes Diffusionsmodell vorgestellt, bei dem die Auswirkung der Elektronenüberhitzung berücksichtigt wird. Dieses Modell erweist sich als sehr viel zuverlässiger für die Ermittlung von Spindiffusionsraten, welche dadurch erstmals systematisch für einen großen Temperatur- und Dotierbereich erfasst werden konnten. Dies ist ein starkes Indiz dafür, dass die häufig beobachteten ungewöhnlich hohen Spindiffusionsraten zumindest teilweise auf die Überhitzung der Leitungselektronen zurückzuführen sind.

Zusätzlich zu diesen neuen Erkenntnissen wurden im Zuge dieser Arbeit einige experimentelle und technologische Optimierungen entwickelt und realisiert. Zunächst wurde die optische Auflösung der Raster-MOKE-Mikroskopie durch die Implementierung einer neuen Raster-Methode verbessert. Des Weiteren wurden zwei verschiedene Arten der bildgebenden Photolumineszenz-Spektroskopie implementiert und optimiert, um ortsaufgelöste Messungen der Elektronen- und Gittertemperatur durchzuführen.

In der vorliegenden Arbeit wird gezeigt, dass die oftmals angegeben sehr hohen Spindiffusionsraten zu einem großen Teil durch die Überhitzung des Elektronensystems verursacht werden. Obwohl eine effiziente Methode gefunden wurde, den Einfluss dieser Überhitzung mathematisch zu berücksichtigen, ist es dennoch offensichtlich, dass die klassische Einstein-Beziehung unter den gegebenen Versuchsbedingungen nicht immer erfüllt war. In diesem Fall kann jedoch argumentiert werden, dass die Ursache hierfür kein experimentelles Artefakt war, sondern eine Manifestation der fermionischen Natur der Leitungsbandelektronen.

# Summary

Since the late 20th century, spintroncis has become a very active field of research [ŽFS04]. The prospect of spin based information technology, featuring strongly decreased energy consumption and possibly quantum-computation capabilities, has fueled this interest. Standard materials, like bulk gallium arsenide (GaAs), have experienced new attention in this context by exhibiting extraordinarily long lifetimes for nonequilibrium spin information, which is an important requirement for efficient spin based information storage and transfer. Another important factor is the lengthscale over which spin information can be transported in a given material and the role of external influences. Both aspects have been studied experimentally with innovative optical methods since the late 1990s by the groups of D. D. AWSHALOM and S. A. CROOKER *et al.* [KA99, CS05, CFL$^+$05]. Although the pioneering experimental approaches presented by these authors led to a variety of insights into spin propagation, some questions were raised as well. Most prominently, the classical Einstein relation, which connects the mobility and diffusivity of a given particle species, seemed to be violated for electron spins in a bulk semiconductor. In essence, nonequilibrium spins appeared to move (diffuse) faster than the electrons that actually carry the spin. However, this contradiction was masked by the fact, that the material of interest was $n$-type GaAs with a doping concentration directly at the transition between metallic and insulating behavior (MIT). In this regime, the electron mobility is difficult to determine experimentally. Consequently, it was not *a priori* obvious that the spin diffusion rates determined by the newly introduced optical methods were in contradiction with established electrical transport data.

However, in an attempt to extend the available data of optical spin microscopy, another issue surfaced, concerning the mathematical drift-diffusion model that has been commonly used to evaluate lateral spin density measurements. Upon close investigation, this model appears to have a limited range of applicability, due to systematic discrepancies with the experimental data (chapter 4). These deviations are noticeable in original publications as well, and it is shown in the present work that they originate from the local heating of electrons in the process of optical spin pumping. Based on insights gained during the second half of the 20th century, it is recapitulated why conduction electrons are easily overheated at cryogenic temperatures. The main reason is the poor thermal coupling between electrons and the crystal lattice (chapter 3). Experiments in the present work showed that a significant thermal gradient exists in the conduction band under local optical excitation of electron–hole pairs. This information was used to develop a better mathematical model of spin diffusion, which allowed to derive the diffusivity of the undisturbed system, due to an effective consideration of electron overheating. In this way, spin diffusivities of $n$-GaAs were obtained as a function of temperature and doping density in the most interesting regime of the metal–insulator-transition.

The experiments presented in this work were performed on a series of $n$-type bulk GaAs samples, which comprised the transition between metallic conductivity and electrical insulation at low temperatures. Local electron temperature gradients were measured by a hyperspectral photoluminescence imaging technique with subsequent evaluation of the electron–acceptor (e,A$^0$) line shape. The local density of nonequilibrium conduction electron spins was deduced from scanning magneto-optic Kerr

effect microscopy. Numerical evaluations were performed using the finite elements method in combination with a least-squares fitting procedure.

Chapter 1 provides an introduction to historical and recent research in the field of spintronics, as far as it is relevant for the understanding of the present work. Chapter 2 summarizes related physical concepts and experimental methods. Here, the main topics are semiconductor optics, relaxation of hot conduction electrons, and the dynamics of nonequilibrium electron spins in semiconductors.

Chapter 3 discusses optical heating effects due to local laser excitation of electron–hole pairs. Experimental evaluations of the acceptor-bound-exciton triplet lines led to the conclusion that the crystal lattice is usually not overheated even at high excitation densities. Here, the heat is efficiently dissipated to the bath, due to the good thermal conductivity of the lattice. Furthermore, the heating of the lattice is inherently limited by the weak heat transfer from the electron system, which on the other hand is also the reason why conduction electrons are easily overheated at temperatures below $\approx 30\,\mathrm{K}$. Spatio-spectral imaging of the electron–acceptor-luminescence line shape allowed to trace the thermal gradient within the conduction band under focused laser excitation. A heat-diffusion model was formulated, which reproduces the experimental electron-temperature trend nicely for low-doped GaAs samples of $n$- and $p$-type. For high-doped $n$-type GaAs samples, it could be shown that the lateral electron-temperature profile is well approximated by a Gaussian. This facilitated easy integration of hot electron influence into the mathematical model of spin diffusion.

Chapter 4 deals with magneto-optical imaging of optically induced nonequilibrium conduction-electron spins in $n$-GaAs close to the MIT. First, the spectral dependence of the magneto-optic Kerr effect was examined in the vicinity of the fundamental band gap. Despite the marked differences among the investigated samples, the spectral shape of the Kerr rotation could be described in terms of a simple Lorentz-oscillator model in all cases. Based on this model, the linearity of the Kerr effect with respect to a nonequilibrium spin polarization is demonstrated, which is decisively important for further quantitative evaluations.

Furthermore, chapter 4 presents an experimental survey of spin relaxation in $n$-GaAs at the MIT. Here, the dependence of the spin relaxation time on bath temperature and doping density was deduced from Hanle-MOKE measurements. While all observed trends agree with established literature, the presented results extend the current portfolio by adding a coherent set of data.

Finally, diffusion of optically generated nonequilibrium conduction-electron spins was investigated by scanning MOKE microscopy. First, it is demonstrated that the standard diffusion model is inapplicable for data evaluation in certain situations. A systematic survey of the residual deviations between this model and the experimental data revealed that this situation unfortunately persisted in published works. Moreover, the temperature trend of the residual deviations suggests a close connection to the local overheating of conduction electrons. Consequently, a modified diffusion model was developed and evaluated, in order to compensate for the optical heating effect. From this model, much more reliable results were obtained, as compared to the standard diffusion model. Therefore, it was shown conclusively that the commonly reported anomalously large spin diffusivities were at least in parts caused by overheated conduction electrons.

In addition to these new insights some experimental and technological enhancements were realized in the course of this work. First, the optical resolution of scanning MOKE microscopy was improved

by implementing a novel scanning mechanism, which allows the application of a larger aperture objective than in the usual scheme. Secondly, imaging photoluminescence spectroscopy was employed for spatially resolved electron-temperature measurements. Here, two different implementations were developed: One for lattice-temperature measurements by acceptor–bound exciton luminescence and a second for conduction-electron temperature measurements via the analysis of the electron–acceptor luminescence line shape.

It is shown in the present work that the originally stated anomalously high spin diffusivities were caused to a large extent by unwanted optical heating of the electron system. Although an efficient method was found to compensate for the influence of electron heating, it became also evident that the classical Einstein relation was nonetheless violated under the given experimental conditions. In this case however, it could be shown that this discrepancy did not originate from an experimental artifact, but was instead a manifestation of the fermionic nature of conduction electrons.

# Danksagung

An dieser Stelle möchte ich all denjenigen herzlich danken, die mich auf die eine oder andere Art bei der Fertigstellung dieser Arbeit unterstützt haben. Dies sind

- Prof. Dr. W. Ossau
- Prof. Dr. L. Molenkamp und die Mitarbeiter des Lehrstuhls EP3
- Prof. Dr. A. Wieck (Uni Bochum)
- meine Arbeitsguppen-Kollegen Georgy Astakhov, Christoph Aulbach, Michael Beck, Steffen Bieker, Tobias Henn, Katharina Janßen, Tobias Kießling, Andreas Kreisel, Franz Münzhuber, Jürgen Schwittek, Heidi Seinige und Farida Veliev
- die Mitarbeiter der Wissenschaftlichen Werkstatt
- die Mitarbeiter der Fakultät für Physik und Astronomie
- die Deutsche Forschungsgemeinschaft (SPP 1285)
- die Geschäftsleitung und Mitarbeiter der Firma Accurion GmbH in Göttingen
- meine Eltern
- meine Schwestern, Schwager, Neffen und Nichte
- und ganz besonders meine langjährige Lebensgefährtin und Angetraute Tatjana Quast

Göttingen, im Juli 2016

# Contents

# 1 Introduction

Today's Information Age is characterized by an insatiable demand for ever faster digital information processing. The rapid advances in computer technology since the 1970s have laid the foundations for the development of the internet during the past two decades. By now, this virtual world at the same time facilitates and dominates so many aspects of human civilization that many individuals cannot imagine a life without it anymore. Another important aspect of the post-modern era definitely benefited from the efficient knowledge and information transfer permitted by the internet: There is a broad awareness of the limitedness of global energy resources and of the climatic impact of their consumption. Ironically, it is the computer technology itself that contributes non-negligibly to world-wide energy consumption. Actually, it is an unwanted side-effect that electronics devices turn electrical energy into waste heat. The reason is the ohmic resistance of the semiconductor materials and the necessity to move electrical charges at high frequencies, in order to perform logical operations with sufficient speed. One alternative approach envisions the use of spin polarization instead of excess electrical charge for encoding digital information. This *spintronics* concept has inspired its own field of research since the 1980s.

Historically, the famous experiment by O. STERN and W. GERLACH in 1922 was the first direct observation of the electron spin [GS22]. During the development of the quantum mechanical understanding of energy and matter in the 1920s, W. PAULI presented the correct interpretation for the Stern-Gerlach experiment in 1927 [Pau27]. In essence, the spin is an intrinsic quantum mechanical degree of freedom, inherent to elementary particles, composite particles (hadrons), and atomic nuclei, which has no equivalent in classical mechanics. Depending on the magnitude of the spin, particles are categorized as bosons (integer spin) or fermions (half-integer spin). Formally, the spin can be treated as a quantum mechanical angular momentum, which leads to relatively simple expressions for spin-orbit coupling. The electron spin has a fixed magnitude of 1/2 in natural units (multiples of the reduced Planck constant) and its direction is quantized to two possible orientations with respect to an external reference (for example a magnetic field or the propagation direction of light). The twofold quantization of its orientation makes the electron spin predestined for storing digital information, while in the historical context it presented the main obstacle for understanding the Stern-Gerlach experiment.

Even before the electron spin was observed by STERN and GERLACH, optical luminescence experiments of alkali metals gave evidence of a mysterious degree of freedom of the outer valence electron. The Zeeman effect, discovered in 1897 [Zee97], describes the energetic shift of spectral lines due to the influence of an external magnetic field. The historic term *anomalous Zeeman effect* was used whenever the electron spin was involved, and the splitting could not be explained by an orbital angular momentum of the electron alone. The Zeeman effect shifts the electronic states of atoms according to their total angular momentum, which is the sum of spin and orbital angular momentum. Due to the conservation of angular momentum, this shift is reflected in the polarization of the shifted spectral lines. The connection between the total angular momentum of electronic states and the optical polarization is usually expressed by optical selection rules, which form the basis of optical spin spec-

troscopy.

The connection between magnetism and the polarization of light was discovered even earlier. In 1845, M. FARADAY observed the rotation of the polarization of light which passes through a transparent medium immersed in a magnetic field [Far33]. In 1876, J. KERR observed that the light reflected from a ferromagnetic sample changed its polarization [Ker76]. In electrodynamics, the magneto-optic Kerr effect (MOKE) and the Faraday effect are related closely, which can be expressed mathematically through the Fresnel equations. Both effects have become important tools in science and technology.

Optical selection rules can be exploited for *optical orientation*, i.e. the creation of a nonequilibrium spin polarization via absorption of polarized light [MZ84]. Also, since the same selection rules apply for radiative recombination, the degree of polarization of luminescence light can reflect the net spin polarization of the excited state. In combination, both mechanisms give rise to the polarization sensitive photoluminescence technique.

In 1924, W. HANLE reported on an experiment, in which he investigated the fluorescence of an optically excited atomic vapor in the presence of a magnetic field [Han24]. He found that the direction of re-emission and the polarization were rotated due to the magnetic field by a characteristic amount. This effect is based on the combination of precession and radiative decay. Hanle's first semi-classical interpretation was already suited to determine the lifetime of excited electronic states. It is specifically remarkable that the *Hanle effect* provides experimental access to microscopical timescales via steady state experiments, i.e. without explicit temporal resolution.

In 1969, R. R. PARSONS was the first to employ the Hanle effect in semiconductor spectroscopy. He used it to determine the lifetime of nonequilibrium conduction electrons in $p$-type GaSb [Par69]. Since the 1970s, the Hanle effect has been applied extensively for the investigation of nonequilibrium spins in semiconductors [ES70, GES71, MZ84]. Especially, the microscopic mechanisms that cause relaxation of spins were identified [MZ84]. These mechanisms are discussed in chapter 2.7.

Macroscopically, a nonequilibrium spin ensemble can be described in the mathematical formalism introduced by F. BLOCH in 1946 in the context of nuclear magnetic resonance [Blo46]. This formalism covers relaxation, dephasing and precession of spins, subjected to a magnetic field. The Hanle effect can also be derived from the Bloch equations. In 1956, H. C. TORREY added the diffusion of spin carriers to this framework [Tor56]. The Bloch-Torrey formalism is discussed in chapter 2.6.

Optical investigations of spin dynamics in semiconductors relied strongly on the Hanle effect before pulsed lasers provided the necessary temporal resolution for direct time-domain observations. Transient luminescence polarization and magneto-optical spectroscopy with sub-picosecond resolution allowed direct observations of spin precession and relaxation [HRP94, OR95]. In contrast to Hanle effect studies, these experiments yield information about the electron $g$-factor as well, which is in fact required for a quantitative interpretation of the Hanle effect. However, $g$-factors in semiconductors have been measured before, for example by conduction electron spin resonance (CESR) [WH77].

A very interesting invention of the late 1990s is the spin-noise spectroscopy, which represents an almost non-invasive way of measuring spin relaxation times and $g$-factors of conduction electrons. In this technique, the random fluctuations of the equilibrium spin ensemble are probed off-resonantly via

the magneto-optic Faraday effect. An external magnetic field is used to shift the spin noise spectrally out of the low frequency background noise. The spin relaxation time is related to the spectral width of the measured noise peak and the $g$-factor can be calculated from the central frequency, which is the Larmor frequency corresponding to the applied magnetic field. This method has been employed intensively by M. OESTREICH *et al.* for systematic studies of conduction electron spins in GaAs [ORHH05, CCS09, MORH10, RBM$^+$10].

Magneto optical measurements in semiconductor systems were first performed in diluted magnetic materials [GOD$^+$88, CAS95] and shortly afterwards transferred to the investigation of optically oriented nonequilibrium conduction-electron spins in non-magnetic semiconductors [KSSA97, KA98]. The high sensitivity of this technique made it possible to detect the spatio-temporal evolution of individual spin packets with micrometer and sub-picosecond resolution. In 1999, J. M. KIKKAWA and D. D. AWSCHALOM presented drift and diffusion measurements of electron spins in $n$-type GaAs [KA99], which revealed an important effect. They found that the spin diffusivity exceeded the corresponding electron diffusivity by more than one order of magnitude.

In the beginning of the 21st century, spin drift and diffusion were investigated in detail by S. A. CROOKER *et al.* via scanning Kerr microscopy [CS05, CFL$^+$05]. They conducted thorough studies of external influences (strain, electrical and magnetic fields, etc.) on the propagation of optically and electrically injected nonequilibrium electron spins in $n$-GaAs under steady-state conditions. In these works, a classical drift-diffusion model, based on the Bloch-Torrey equations, was utilized, in order to obtain important spin transport parameters (diffusivity, mobility and relaxation time) from these data. Curiously, the spin diffusivity obtained from this model systematically exceeded the corresponding charge diffusivity, which was already recognized earlier [KA99].

This phenomenon of enhanced spin diffusivity was neither exclusively observed in optical experiments nor limited to GaAs as a material system. B. HUANG and I. APPELBAUM investigated drift and diffusion of spin-polarized electrons via time-of-flight spectroscopy in silicon transport devices [HA10]. Using the Larmor-clock technique, they measured the diffusive broadening and drift velocity of electrically injected electron spins. Their data clearly revealed spin diffusion in excess of the corresponding charge diffusion by approximately a factor of ten.

In the context of anomalous spin diffusion in semiconductors, the *spin Coulomb drag* was discussed frequently. As the name suggests, the Coulomb scattering with spin exchange between electrons leads to a suppression of the spin current. The effect was proposed and examined theoretically by I. D'AMICO and G. VIGNALE on the threshold to the 21st century [DV00, DV01, DV02]. In 2005, spin Coulomb drag was observed experimentally by C. P. WEBER *et al.* in GaAs/GaAlAs quantum well structures via another interesting technique, the optically induced spin grating [WGM$^+$05]. However, since the spin Coulomb drag systematically reduces spin currents, it cannot explain the experimentally observed enhancements of spin diffusivity. Moreover, the spin Coulomb drag is only of practical relevance in low-dimensional systems, where the necessary high carrier densities are reached more easily than in bulk materials.

In 2006, S. G. CARTER *et al.* investigated charge and spin diffusion in $n$-doped GaAs quantum wells by means of optically induced spin and charge density gratings [CCC06]. In particular, they observed a strong dependence of the spin and charge diffusivities on the excitation photon energy. From this, they concluded that optically excited hot electrons are partly responsible for the enhanced

spin diffusion observed in numerous optical orientation experiments. Moreover, the distinctly different temperature and excitation density dependencies of the electron $g$-factor suggested that the lattice temperature did not change significantly with the excitation intensity. As a final conclusion, CARTER *et al.* hypothesized about controlling spin transport by changing the excitation conditions. This kind of effect was indeed observed in 2007 [Qua07] and published in 2009 [QAO+09].

Shortly after the first discovery of anomalously enhanced spin diffusion in $n$-GaAs, M. E. FLATTÉ and J. M. BYERS presented theoretical revelations about spin and charge diffusion in doped and undoped semiconductors, in an attempt to explain this behavior. They first pointed out the relevance of *ambipolar diffusion*, which describes the necessity of co-propagation for mutually attractive particles (i.e. conduction electrons and valence band holes) in order to preserve charge neutrality. Nonequilibrium spin and charge carriers in an undoped semiconductor are inevitably subject to ambipolar diffusion. On the other hand, intrinsic electrons in an $n$-doped semiconductor can be spin polarized without the need for a charge imbalance. This distinction between single- and multi-band disturbances is summarized in figure 1.1. Additionally, FLATTÉ and BYERS demonstrated that in the case of high electron densities the fermionic nature of conduction electrons leads to a modified relation between diffusivity and mobility (*Einstein relation*), as compared to the classical case.

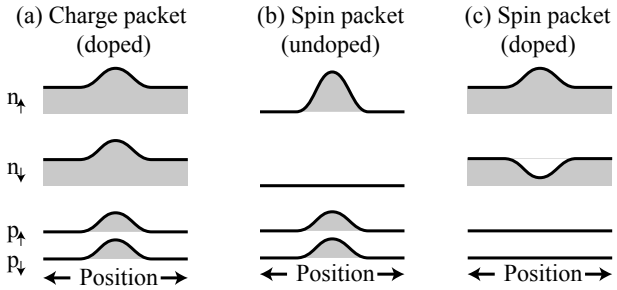


Figure 1.1: Schematic illustration of nonequilibrium spin and charge packets in doped and undoped semiconductors. (a) Pure charge packet. (b) Charge and spin packet. (c) Pure spin packet. Figure adopted from [FB00].

The quantitative theoretical analysis by FLATTÉ and BYERS yielded an enhancement of the spin diffusion coefficient of $eD_s/k_BT\mu_e \approx 12$ for a background electron density of $n = 1 \times 10^{16}\,\mathrm{cm}^{-3}$ and a temperature of $T = 1.6\,\mathrm{K}$. Although this result was in good agreement with the experimental findings in [KA99] it remained doubtful for at least two reasons. First, FLATTÉ and BYERS assumed that all $1 \times 10^{16}$ electrons per cubic centimeter are free to move in the conduction band. They neglected the fact that at $1.6\,\mathrm{K}$ most electrons are bound to donor sites. Secondly, the nearby occurrence of the metal-to-insulator transition (MIT) at $\approx 2.5 \times 10^{16}\,\mathrm{cm}^{-3}$ was entirely ignored. However, approximately at this doping concentration the donor atoms form an impurity band, which merges into the conduction band with increasing doping. Below this density, a complete freeze-out of electrons occurs at low temperatures.On the other hand, electrical conduction prevails even at zero temperature for higher densities.

To summarize, no satisfactory explanation for the anomalously enhanced spin diffusion in $n$-GaAs was given to date. Although CARTER *et al.* suggested elevated electron temperatures as the origin of this behavior, no further investigations of this particular matter have been performed. However, it is quite conceivable, and has also been known for a long time, that optical excitation, as well as electrical fields, can overheat conduction electrons significantly [Lyo86, EL87]. Therefore, the main objective of the present work is to establish a deeper understanding of the influence of hot electrons on spin diffusion in $n$-GaAs around the MIT.

Historically, the first investigations of hot electrons aimed at the understanding of the dielectric breakdown in solids, and began in the 1930s [LK34, Frö43, Sei49]. Two very thorough and comprehensive review articles, explicitely dedicated to photoexcited hot electrons in direct gap semiconductors, were written by S. LYON [Lyo86] as well as by S. E. ESIPOV and Y. B. LEVINSON [EL87] in the 1980s. A more recent and broader overview of hot electrons in semiconductors was given in the book by N. BALKAN [Bal98].

In the 1960s, it was realized that optical spectroscopy allows access to the energy distribution of charge carriers in semiconductors. J. SHAH and R. C. C. LEITE determined the energy distribution of photo-excited charge carriers in GaAs by measuring the high-energy tail of the band-to-band luminescence [SL69]. Their data showed that electrons and holes in GaAs are Maxwell-Boltzmann distributed under continuous optical excitation. Depending on the excitation intensity, they obtained charge-carrier temperatures between $14\,\mathrm{K}$ and $76\,\mathrm{K}$ at a bath temperature of only $2\,\mathrm{K}$. Moreover, SHAH and LEITE already noted that charge carriers are significantly overheated even for very moderate light intensities of a few Watt per $\mathrm{cm}^2$. For comparison, typical scanning-MOKE experiments utilized intensities of several hundred to thousands of Watts per $\mathrm{cm}^2$, which arised from the strong focusing of laser light [QAO$^+$08].

In 1973, R. ULBRICH systematically measured the thermal relaxation process of hot photoexcited conduction electrons in GaAs [Ulb73]. He introduced a new method which — in contrast to previous experiments [SL69] — yields the energy distribution of conduction electrons independently of the valence hole distribution. Here, the conduction-electron energy distribution was derived from the line shape of the conduction-band-to-acceptor luminescence. This method was also used in the present work for spatially-resolved conduction-electron temperature measurements.

In his paper, ULBRICH very nicely drew a coherent picture of conduction-electron thermal relaxation through a combination of steady-state and transient measurements, as well as thorough comparisons with well known theoretical concepts. Besides many more detailed insights about the topic, this work draws the same conclusion as given by SHAH and LEITE: Photoexcited electrons in high purity GaAs are almost always overheated at lattice temperatures below $\approx 20\,\mathrm{K}$. The main reason for this is the inefficient electron heat dissipation at low energies. This topic is discussed in detail in chapter 2.4.

Optically injected spin-polarized electrons are certainly no exception to this rule. It is shown in the course of this work that local optical excitation in spin-imaging experiments produces a thermal gradient in the electron system, which decisively influences lateral spin diffusion. Moreover, in order to account for this effect on a mathematical level a phenomenological approach is presented and shown to yield much better agreement with experimental data than the previously applied diffusion model.

The present work is structured in the following way. Chapter two summarizes important physical concepts for optical semiconductor studies and spin physics in GaAs. Chapter three deals with heating effects due to optical interband excitation. Here, the goal was to retrieve information about lateral thermal gradients under local laser illumination. The chapter begins with a detailed description of the experimental methods and techniques. Afterwards, the temperatures of the crystal lattice and the conduction electrons are studied separately. This was done with close reference to the experimental conditions of two-color MOKE experiments, in order to evaluate the influence of laser induced heating on optical spin studies. Chapter four focuses on two-color Hanle-MOKE and MOKE microscopy

investigations of spin dynamics in $n$-type GaAs. This chapter also begins with a detailed description of experimental techniques and procedures. This is followed by investigations performed on a series of $n$-type GaAs samples with doping concentrations close to the MIT. First, the optically induced exciton Kerr effect is discussed. It was evaluated on the basis of classical electrodynamics and a simple oscillator model of the excitonic resonance. Secondly, the doping and temperature dependence of the spin relaxation time was studied by Hanle-MOKE measurements. And thirdly, spin diffusion was investigated on the basis of spatially resolved two-color MOKE measurements. Here, the aforementioned shortcomings of the standard diffusion model became clearly noticeable. Based on the findings of laterally resolved electron temperature studies, a new spin diffusion model was developed, which overcame these issues and yielded more reliable spin transport data. After the main results, the most important conclusions from this work are summarized and put into context with some selected recent achievements and developments by other researchers. Finally, an overview of the investigated sample materials as well as supporting electron transport data are provided in the appendix of this work.

# 2 Fundamentals

This chapter presents an overview of the physical concepts and terminology needed for semiconductor spin optics. It begins with an introduction to the investigated material system, gallium arsenide (GaAs). After some general physical and technological remarks, the electronic band structure and spin–orbit coupling at the $\Gamma$-point are described. In chapter 2.3 the interaction of GaAs with light in the spectral vicinity of the direct band gap is discussed. The main topics here are the in-band excess energy that occurs from non-resonant photoexcitation as well as the importance of Coulomb interactions for spectroscopic luminescence investigations. Chapter 2.4 fills the gap between excitation and optical decay by discussing the intraband relaxation of photogenerated conduction electrons. Since the main topic of the present work is the influence of hot electrons on electron-spin properties it is motivated here how electron overheating occurs and why cooling of hot electrons is insufficient at cryogenic temperatures. This topic is closed with the description of an experimental method for the spectroscopic measurement of conduction electron temperatures.

Turning the discussion to spectroscopic spin studies, the method of *optical orientation* of conduction-electron spins is discussed in chapter 2.5. Here, the optical selection rules are exploited, which occur in GaAs and other zinc-blende type semiconductors due to the symmetry of the band states near the center of the Brillouin zone. Chapter 2.6 then presents a mathematical description of the dynamic behavior of a nonequilibrium spin ensemble. First, the commonly known Bloch formalism is presented, which is then reduced to a mathematical form that is better suited for lateral spin imaging. Following this phenomenological description of spin dynamics, the physical mechanisms which lead to relaxation of nonequilibrium spins in semiconductors are discussed in chapter 2.7. In the following section the Hanle effect is described, which presents an elegant method for measuring relaxation times under steady-state conditions, i.e. without explicit time resolution. Finally, chapter 2.9 gives a description of the magneto-optic effects that are exploited in the present work for optical detection of nonequilibrium conduction-electron spins with micrometer lateral resolution.

## 2.1 Properties of GaAs

Gallium arsenide (GaAs) is a binary compound from the family of the III-V semiconductors and one of the most important materials in semiconductor science and technology. Today, its main applications are settled in high-frequency electronics, light emitting diodes and laser diodes as well as high-efficiency solar cells [YC10]. Single crystals of high quality and purity with well defined doping concentrations are readily available. After more than half a century of intense research and development, a wealth of knowledge about its physical properties renders GaAs a perfect model system for experimental studies in basic research.

GaAs consists of equal amounts of gallium and arsenic atoms which crystallize in the zinc-blende structure with a lattice constant of $a_0 = 5.65\,\text{Å}$ at room temperature [MSDW76]. The zinc-blende

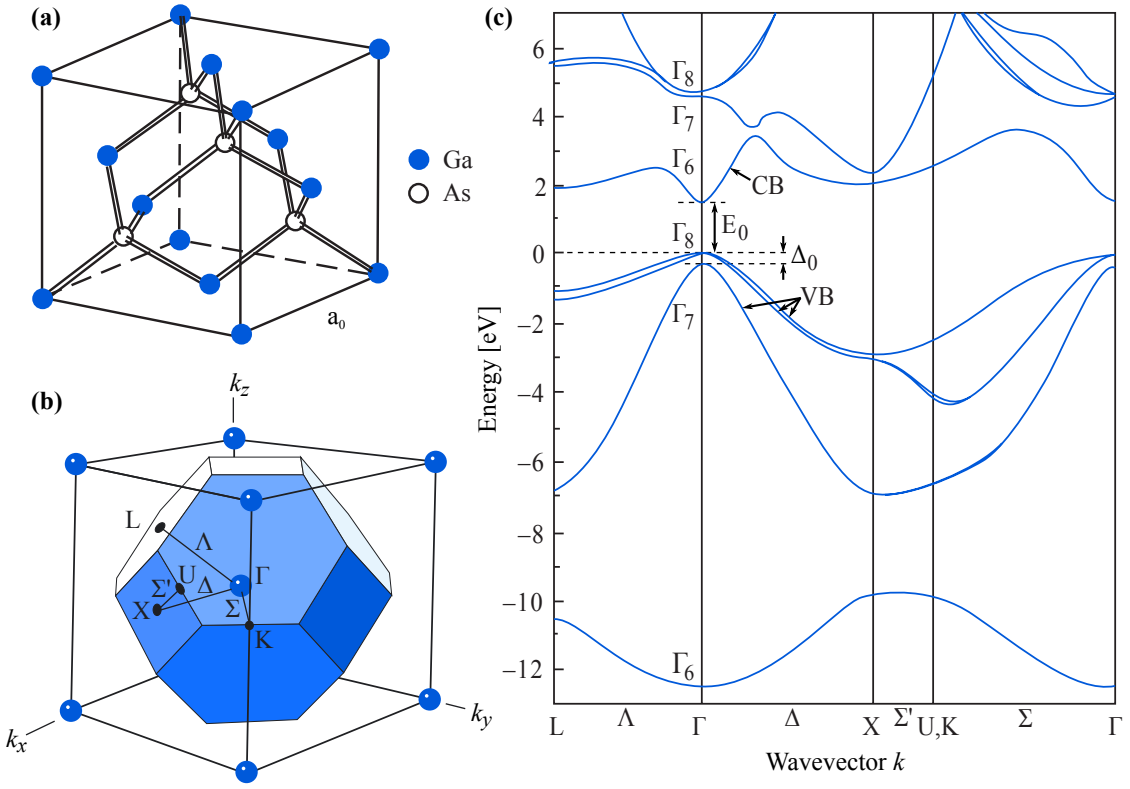


Figure 2.1: **(a)** Schematic drawing of the GaAs lattice structure. Each arsenic atom (white spheres) is tetrahedrally surrounded by four gallium atoms (blue spheres) and vice versa. **(b)** Schematic drawing of the first Brillouin zone of the zinc-blende lattice. Each blue sphere represents a zone center ($\Gamma$-point, $k = 0$). Further high-symmetry points are labeled L, X, K and U, while the connecting paths are designated $\Lambda$, $\Delta$, $\Sigma$ and $\Sigma'$. **(c)** Calculated band structure of GaAs [CC76]. The bands are labeled according to the double-group representations of the corresponding wavefunctions as $\Gamma_6$, $\Gamma_7$ and $\Gamma_8$. The zero of the energy scale is taken to be at the valence band maximum. The fundamental band gap between valence band (VB) and conduction band (CB) and the spin-orbit splitting are indicated by $E_0$ and $\Delta_0$, respectively. All figures inspired by [YC10].

structure can be constructed from two face-centered cubic (fcc) sublattices, each of which is occupied by one atomic species. These sublattices are shifted with respect to each other by $\frac{\sqrt{3}}{4}a_0$ along the volume diagonal. Each gallium atom is therefore tetrahedrally coordinated by four arsenic atoms and vice versa, as illustrated in figure 2.1 **(a)**.

The chemical bonds between adjacent atoms are formed by the outer valence electrons from the $4s$ and $4p$ atomic orbitals. The remaining electrons are tightly bound to their respective nuclei and therefore do not contribute to electrical transport and optical transitions in the visible range. The resulting $sp^3$-hybridized bonds are predominantly of covalent nature in III-V compounds, due to the very similar electronegativity of the atoms involved. However, the residual ionic character plays an important role for carrier–phonon interaction.

Due to the tetrahedral structure, the symmetric properties of the zinc-blende lattice are described by the $T_d$ point group. In contrast to the monoatomic diamond-lattice, which is described by the $O_h$ point group of the cube, binary compounds with zinc-blende structure do not exhibit inversion symmetry.

The evolution of the electronic states from atomic orbitals into continuous energy bands can be understood in the following way. If two atoms are in close proximity, the $s$- and $p$-orbitals split into bonding and antibonding $\Sigma$- and $\Pi$-orbitals, respectively. In the crystalline environment, the spatial proximity of many more atoms results in further energy shifts and, more importantly, to a delocalization of the electrons. The electronic states are therefore no longer characterized by their energy alone, but rather by the relation between energy and quasiparticle wave vector $k$, which is often interpreted as momentum. Hence, from each atomic orbital a pair of characteristic dispersion relations $E(k)$ can be derived, where one corresponds to the bonding and the other to the antibonding state.

Figure 2.1 **(b)** illustrates the first Brillouin zone of the zinc-blende lattice with lines and points of high symmetry labeled in accordance with figure 2.1 **(c)**, which shows the electronic band structure of GaAs. The lowest unoccupied band stems from the antibonding $\Sigma$-orbitals and is called conduction band. The corresponding wave functions are of $s$-like symmetry described by the $\Gamma_6$ representation of the tetrahedron double-group including the spin. The highest occupied band originates from the bonding $\Pi$-orbitals and is known as the valence band. The fact that the minimum of the conduction band coincides with the maximum of the valence band at $k = 0$ makes GaAs a direct-gap semiconductor.[1] At liquid-helium temperature ($4.2\,\mathrm{K}$), the fundamental band gap is $E_{\mathrm{gap}} = 1.5177\,\mathrm{eV}$ [AS73] and reduces with rising temperature approximately according to the empirical formula [Var67, Bla87]

$$E_{\mathrm{gap}}(T) = 1.519\,\mathrm{eV} - 5.408 \times 10^{-4}\,\mathrm{eV\,K^{-1}}\frac{T^2}{(T + 204\,\mathrm{K})} \tag{2.1}$$

## 2.2 Spin-orbit coupling

In atomic physics, the orbital electronic wave functions are classified as $s$, $p$, $d$, etc., according to the orbital angular momentum. The quantum mechanical state $|l, m_l\rangle$ is characterized by the quantum numbers $l$ and $m_l$, which correspond to the magnitude and $z$-projection of the orbital momentum. They are connected to the corresponding operators by the eigenvalue equations

$$\begin{aligned} \hat{\boldsymbol{l}}^2\,|l, m_l\rangle &= l(l+1)\hbar^2\,|l, m_l\rangle \\ \hat{l}_z\,|l, m_l\rangle &= m_l\hbar\,|l, m_l\rangle \end{aligned} \tag{2.2}$$

Mathematically, the quantum numbers $l$ and $m_l$ are the separation constants required for solving the equation of motion for a charged particle in the Coulomb potential of another point charge (hydrogen model). The quantum numbers can only assume integer values $l = 0, 1, 2, ...$ and $m_l = -l, ..., l$, respectively.

In real space, the eigenstates of the angular momentum operator can be represented by the spherical

[1] Due to the absence of inversion symmetry, the VB maximum is expected to be *not exactly* at $k = 0$. However, this effect appears to be so small that is was never observed experimentally.

harmonic functions $Y_{lm}$. For $p$-states, where $l = 1$ and $m_l = -1, 0, 1$, the eigenstates can be written

$$\begin{aligned} |1,1\rangle &= -\left(\sqrt{2}r\right)^{-1}(\hat{x} + \mathrm{i}\hat{y}) \\ |1,0\rangle &= r^{-1}z \\ |1,-1\rangle &= \left(\sqrt{2}r\right)^{-1}(\hat{x} - \mathrm{i}\hat{y}) \end{aligned} \tag{2.3}$$

with $r = \sqrt{\hat{x}^2 + \hat{y}^2 + \hat{z}^2}$ and $\hat{x}$, $\hat{y}$, $\hat{z}$ the quantum mechanical operators of the spatial coordinates.

Formally, the electron spin $\boldsymbol{s}$ can be treated like a quantum mechanical angular momentum with quantum numbers $s = 1/2$ and $m_s = \pm 1/2$. The corresponding eigenstates $|\uparrow\rangle$ and $|\downarrow\rangle$ are called spin-up and spin-down, respectively. Taking into account the magnetic interaction between the orbital angular momentum and the spin, $\boldsymbol{l}$ and $\boldsymbol{s}$ are no longer conserved quantities. Consequently, $l$, $m_l$ and $m_s$ are not anymore valid quantum numbers, i.e. $|l, m_l\rangle|\uparrow\rangle$ and $|l, m_l\rangle|\downarrow\rangle$ are not the eigenstates of the coupled system. However, the total angular momentum $\boldsymbol{j} = \boldsymbol{l} + \boldsymbol{s}$ is conserved over time and can be described by a new set of quantum numbers $j$ and $m_j$, with the half-integer values $l-s, ..., l+s$ and $-j, ..., j$, respectively. The corresponding eigenstates $|j, m_j\rangle$ can be expressed as linear combinations of the eigenstates of $\boldsymbol{l}$ and $\boldsymbol{s}$. These spin-orbit coupled $p$-states read

$$\begin{aligned} |3/2,3/2\rangle &= |1,1\rangle|\uparrow\rangle \\ |3/2,1/2\rangle &= 3^{-1/2}\left(|1,1\rangle|\downarrow\rangle + \sqrt{2}\,|1,0\rangle|\uparrow\rangle\right) \\ |3/2,-1/2\rangle &= 3^{-1/2}\left(|1,-1\rangle|\uparrow\rangle + \sqrt{2}\,|1,0\rangle|\downarrow\rangle\right) \\ |3/2,-3/2\rangle &= |1,-1\rangle|\downarrow\rangle \\ |1/2,1/2\rangle &= 3^{-1/2}\left(|1,0\rangle|\uparrow\rangle - \sqrt{2}\,|1,1\rangle|\downarrow\rangle\right) \\ |1/2,-1/2\rangle &= 3^{-1/2}\left(|1,0\rangle|\downarrow\rangle - \sqrt{2}\,|1,-1\rangle|\uparrow\rangle\right) \end{aligned} \tag{2.4}$$

which among others describe the valence-band states at the $\Gamma$-point in zinc-blende type semiconductors.

Due to the spin–orbit coupling, the otherwise sixfold degenerate valence band splits into the $j = 1/2$ and $j = 3/2$ states, which are described by the $\Gamma_7$- and $\Gamma_8$-representations, respectively. In GaAs, the spin–orbit splitting energy at the $\Gamma$-point amounts to $\Delta_0 = 341\,\mathrm{meV}$ [AS73]. The $\Gamma_8$ valence-band states decompose further into subbands with $m_j = \pm 3/2$ and $m_j = \pm 1/2$, which are called heavy-hole and light-hole bands, respectively. Without the presence of strain or external fields, the heavy and light-hole bands are degenerated at the $\Gamma$-point. For finite $k$ this degeneracy is lifted by the Dresselhaus effect [Dre55].

## 2.3 Near-band-gap optical transitions

In an undoped ideal semiconductor at zero temperature, the valence band is completely filled with electrons, while the conduction band is entirely empty. Absorption of photons with energy $E_{\text{photon}} \gtrsim E_{\text{gap}}$ excites electrons from the valence band into the conduction band, leaving behind holes in the valence band. Photon energies in the vicinity of the fundamental band gap of GaAs are found in the near-infrared spectral range. The wave vector of these photons is negligible on the scale of the Brillouin zone. Therefore, optical excitation leaves the wave vector of electrons essentially unchanged

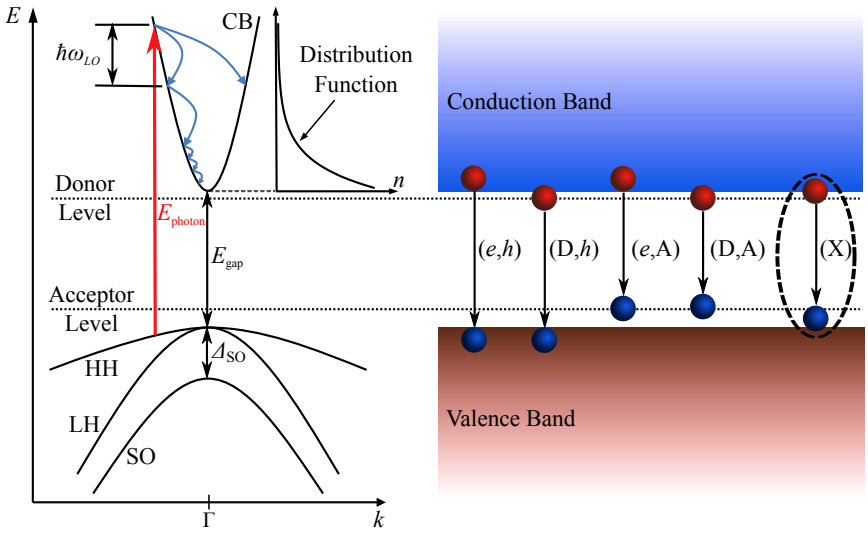


Figure 2.2: Schematic illustration of optical interband absorption, electron thermal relaxation and radiative electron–hole recombination. Optical absorption is depicted as a red vertical arrow in the left part of the figure. In-band relaxation through phonon emission is illustrated by the small blue arrows. The steady-state electron energy distribution is shown schematically in the small inset. Some important recombination channels are shown in the right part. Recombination of free electrons with free holes is labeled $(e, h)$. $(D, h)$ and $(e, A)$ represent recombination of free holes/electrons with the opposite species bound to donors/acceptors, respectively. Pair recombination of bound electrons and holes is labeled $(D, A)$. For the sake of completeness, excitonic recombination is depicted as $(X)$, although the correlated many-particle complexes, i.e. excitons and bound states, cannot be represented correctly in the single-particle band picture.

(dipole approximation). Figure 2.2 illustrates an electronic dipole transition by a vertical arrow with length $E_{\text{photon}}$, connecting an initial valence-band state with a conduction-band state in the dispersion diagram.

If excitation takes place with a photon energy exceeding the direct band gap, electrons and holes are put into the bands at some distance from the Γ-point. To obey conservation of wave vectors, the excess energy $E_{\text{photon}} - E_{\text{gap}}$ is distributed between electron and hole according to the ratio of their effective masses. For isotropic bands with $E(k) \propto k^2$, the initial electron excess energy can be calculated as

$$E_e = (E_{\text{photon}} - E_{\text{gap}}) \left(1 + \frac{m_e}{m_h}\right)^{-1} \tag{2.5}$$

For GaAs established values of the effective band masses near the Γ-point are listed in appendix C. In the above equation $m_h$ represents either light or heavy holes, depending on the initial state of the electron before excitation.

In the vicinity of the Γ-point, the conduction band is in good approximation isotropic, while the heavy-hole (HH) and light-hole (LH) bands exhibit a pronounced anisotropy and nonparabolicity in $k$-space. This *band warping* in combination with the valence-band splitting leads to a character-

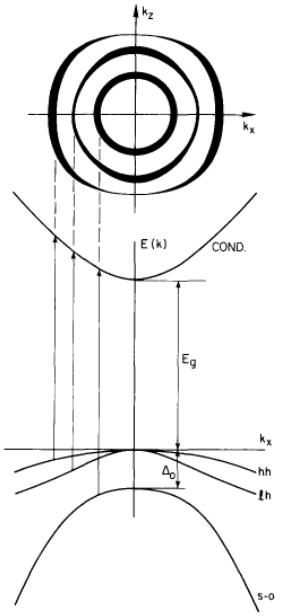


Figure 2.3: Illustration of the initial density of photoexcited electrons near $k = 0$. The lower part shows the heavy and light hole and split-off valence bands. The arrows show the possible transitions upon absorption of photons polarized in $z$-direction with an energy of $2\,\mathrm{eV}$. The upper part shows the distribution of electrons in $k$-space. The thickness of each ring represents the relative occupation of the corresponding $k$-state. The deviation of the rings from the circular shape reflects the distribution of the initial energy as discussed in the text. Figure adopted from [Lyo86]

istic distribution of photoexcited electrons. This effect is illustrated in figure 2.3. Excitation with monochromatic light produces a spread of electron energies of about 6% of $E_{\text{photon}} - E_{\text{gap}}$ for each valence band [Lyo86].

Charge carriers redistribute their excess energy among themselves by elastic scattering. At the same time, they dissipate their excess energy to the lattice by interaction with phonons. The energy distribution within the band (small plot in figure 2.2) that arises under steady-state conditions is a complicated result of the competition between these processes, which is discussed in chapter 2.4.

Finally, nonequilibrium electrons and holes annihilate each other by recombination. However, the probability for free-electron–hole recombination is rather small due to the requirement of wave-vector conservation. The main contributions to luminescence spectra at liquid-helium temperature therefore arise from excitons and impurity-bound charge carriers. Here, wave-vector conservation is effectively lifted due to the localization of charge carriers. However, since the binding energy of these complexes is only around $\approx 5\,\mathrm{meV}$ in GaAs, they tend to dissociate at temperatures above $\approx 50\,\mathrm{K}$. In the right half of figure 2.2 some typical electron–hole recombination channels are summarized schematically.

For near band-gap luminescence spectroscopy in GaAs and other direct gap semiconductors, substitutional impurities are of special interest. Depending on the valence of an impurity atom compared to the original host atom it replaces, one distinguishes donors, acceptors, and isoelectric impurities. By definition, donors contribute additional electrons to the crystal, while acceptors have a lack of such, and therefore provide holes to the valence band. Doping is commonly performed intentionally in order to provide additional charge carriers, which are easily activated for electrical transport.

Donor and acceptor atoms differ from the original host atoms in their nuclear charge number. This excess charge (positive for donors and negative for acceptors) contributes a local disturbance to the lattice periodic coulomb potential. The coulomb interaction between charge carriers and impurity atoms therefore creates bound states. Depending on whether or not the energy spectrum and wave

functions of these states are well described by the quantum-mechanical central-potential model (Bohr model), one distinguishes *shallow impurities* and *deep centers*. If the quasi-particle wave function extends over a sufficiently large number of unit cells the effective mass approximation is still valid. This implies that the crystal environment (lattice and other electrons) appears to the bound charge as a continuous and homogeneous medium, i.e. an average dielectric constant can be defined. This picture yields good agreement with experimentally observed donor levels in GaAs. On the other hand, acceptor bound holes cannot be described in the effective-mass approximation, due to the warping of the valence bands and their degeneracy at the $\Gamma$-point in tetrahedrally aligned systems.

For shallow impurities, the ground state energy and the lateral extend of the wave function can be expressed in terms of an effective Rydberg constant $R^*$ and a Bohr radius $a^*$

$$R^* = \frac{m^* e^4}{32\left(\pi\epsilon\epsilon_0\hbar\right)^2} \tag{2.6}$$

$$a^* = \frac{4\pi\epsilon\epsilon_0\hbar^2}{m^* e^2} \tag{2.7}$$

where $m^*$ is the bound quasi-particle effective mass, $\epsilon$ is the DC dielectric constant and $\epsilon_0$ is the vacuum permitivity. For donors in GaAs, this yields $R^* = 5.7\,\mathrm{meV}$, which is in good agreement with the experimentally observed binding energies of $\approx 5.9\,\mathrm{meV}$[Bla87]. The corresponding donor Bohr radius is $a^* \approx 10\,\mathrm{nm}$ and therefore about 20 times larger than the primitive unit cell. For acceptors in GaAs, numerical calculations yield a ground state energy of $25.6\,\mathrm{meV}$ [YC10], while experimental observations lie in the range of $\approx 27$ to $\approx 35\,\mathrm{meV}$ [Bla87].

The coulomb interaction between free electrons and holes leads to the formation of coulomb-correlated bound states known as *excitons*. By analogy with shallow and deep impurities, one distinguishes Wannier excitons and Frenkel excitons. While Wannier excitons extend over a large number of unit cells and can be approximated by the Bohr model, Frenkel excitons are strongly localized (in their own reference frame). Wannier excitons are the result of a significantly screened coulomb interaction, which is commonly found in semiconductors with large dielectric constant, while Frenkel excitons are usually found in more ionic compounds. Since the atomic bonds in GaAs are mostly covalent, excitons at the fundamental band gap of GaAs are Wannier excitons.

From a formal point of view, a shallow donor is the same as a Wannier exciton with the positive charge having an infinite mass. The energy spectrum and Bohr radius of the exciton are therefore very similar to those of the shallow donor. In fact, the Bohr model yields an exciton ground-state energy of $4.4\,\mathrm{meV}$ and the experimentally determined value is $4.9\,\mathrm{meV}$[YC10].

Excitons can be free to move in the crystal (*free excitons*) or localized at impurity sites through the coulomb interaction (*bound excitons*). The interaction with electromagnetic radiation is fundamentally different for free and bound excitons. While bound excitons behave almost like a two-level system with sharply defined energy levels, free excitons exhibit a continuous energy spectrum and must be described as *exciton-polaritons*.

**Free excitons** In contrast to impurity-bound charge carriers, free excitons are not localized in the reference frame of the lattice. The total energy of an exciton therefore consists of the coulomb contri-

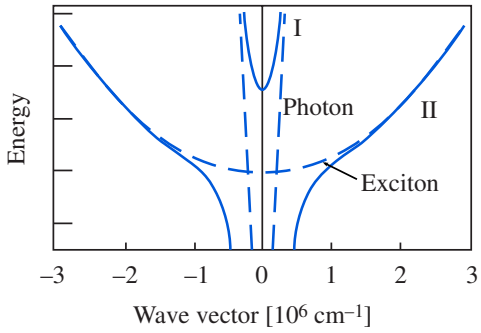


Figure 2.4: Dispersion curves of free excitons and photons (dashed curves) and the two branches of the coupled exciton-polariton wave (solid lines, labeled I and II). Figure adopted from [YC10].

bution and the center-of-mass kinetic energy. In a simple picture, the coulomb interaction leads to a series of quantized energy levels, which are superimposed by a parabolic free-particle dispersion.

In order to describe their interaction with electromagnetic radiation, excitons must be interpreted as excitations of a quantum-mechanical oscillator field, i.e. the electron-hole plasma in a semiconductor. This exciton field couples to the electromagnetic field by the finite dipole moment of the exciton ground state. Due to the conservation of energy and wave vector, conversion of photons into excitons and vice versa is only possible in the vicinity of the intersection of their dispersion curves. As shown in figure 2.4, the finite coupling leads to a new dispersion relation which exhibits an avoided crossing at the intersection of the pure photon and pure exciton dispersions. Since photon and exciton do no longer exist independently, the coupled state is called *exciton-polariton*. The upper polariton branch (I) has predominantly photonic character, while the lower branch (II) has more excitonic properties. The photon-like states are efficiently transformed back into photons at the sample surface, which is observable as free-exciton luminescence. On the other hand, the exciton-like states of branch II cannot be transformed into photons without losing some momentum to phonons first. Moreover, the probability of inelastic scattering is comparatively high, which leads to nonradiative destruction of the polariton.

Optical absorption, for instance, can be understood as a two-step process in the exciton-polariton picture. When a photon enters the crystal, it first exists on the photon-like branch I of the polariton dispersion. From there, it can scatter elastically into branch II. The exciton-like polariton wave has a good chance to be scattered inelastically by impurities, defects, phonons or other electrons, thereby dissipating its energy to the lattice or electron system. The absorption spectrum of free excitons is therefore determined by two factors. First, the conversion rate of photons into excitons and secondly, the rate of inelastic scattering of excitons at a given energy.

The luminescence spectrum of exciton-polaritons is dominated by the photon-like states. Radiative recombination is strong at energies where the polariton dispersion resembles the pure-photon dispersion closely. This is the case at rather high and rather low energies, compared to the energy of the pure exciton at $k = 0$. In the intermediate regime, the polariton dispersion is clearly separated from the pure-photon dispersion and radiative recombination is suppressed due to wave-vector conservation. This gap manifests as a double-peak spectral structure, which corresponds to the upper and lower polariton-branch contributions.

**Bound excitons** The finite dipole moment of the exciton ground state allows them to bind to lattice impurities. In this case, the exciton has no center-of-mass momentum and is therefore decoupled from the electromagnetic field in the sense that no polaritons can be formed. Hence, the bound exciton has a discrete energy spectrum in contrast to the continuous energy dispersion of the exciton-polariton.

## 2.4 Energy relaxation of photoexcited hot electrons

Optical interband excitation creates electrons in the conduction band and holes in the valence band. The excess energy $E_{\text{photon}} - E_{\text{gap}}$ is distributed between both quasi particles according to the effective-mass ratio (compare equation 2.5). If excitation took place from the heavy-hole band alone, 88% of the excess energy would be absorbed by electrons and only 12% by heavy-holes. In contrast, electrons excited from the light-hole band would obtain 54% of the optical excess energy.

For optical spin orientation in GaAs (see chapter 2.5), 75% of the electrons are excited from the heavy-hole band and only 25% from the light-hole band.[2] Consequently, the average electron absorbs ≈80% of the total excess energy under these conditions. As a matter of fact, photoexcited electrons are much hotter than the corresponding holes. However, both species exchange energy by scattering, which is discussed later in this chapter.

In spin-imaging experiments, the excess energy typically amounts to several tens of meV per electron–hole pair.[3] In comparison, the average thermal energy of a nondegenerate electron gas at liquid-helium temperature is only $\approx 0.5\,\mathrm{meV}$ per electron. Electrons with much higher kinetic energy than the average energy of the lattice are called *hot electrons*.[4] For bath temperatures below $\approx 30\,\mathrm{K}$, photoexcited hot electrons in GaAs stay overheated during their lifetime in the conduction band, because phonon emission is insufficient for the electron to dissipate its excess energy. The present chapter deals with hot-electron cooling and thermalization in the excitation regime of optical spin-imaging experiments. For a broader and more detailed discussion, the review articles by LYON [Lyo86], ESIPOV and LEVINSON [EL87] are recommended. In chapter 3.4, the picture of electron energy dissipation is extended by a diffusive component in order to gain a description of the lateral electron-temperature gradient under local photoexcitation.

Hot electrons in the conduction band dissipate their energy to the lattice by emission of phonons. Electrons with small wave vector $k$ can only interact with long-wavelength phonons due to wave-vector conservation. The wave vector of a conduction electron at $60\,\mathrm{meV}$ is less than 5% of the size of the first Brillouin zone. Figure 2.5 shows the energy–momentum dispersion of lattice vibrations in GaAs along selected high-symmetry axes. The 5%-range is highlighted by the green bars around the Γ-point. In this regime, optical and acoustical phonon modes are clearly separated on the energy scale. While long-wavelength optical phonons have a finite energy and a relatively flat dispersion, acoustic phonons have an almost linear dispersion and assume zero energy for $k = 0$. Both kinds of

[2] Here it is assumed that no electrons are excited from the spin–orbit split-off band due to the choice of the excitation photon energy (see chapter 2.5).

[3] For example, illuminating GaAs at $4.2\,\mathrm{K}$ with light at $785\,\mathrm{nm}$ wavelength corresponds to an excess energy of $\approx 60\,\mathrm{meV}$. This is a typical situtation in many published spin-orientation experiments [CFL$^+$05, CS05, FSC06, Qua07, CFL$^+$07].

[4] Although this designation seems to imply that a temperature can be defined for hot electrons, they do not necessarily have a thermal energy distribution.

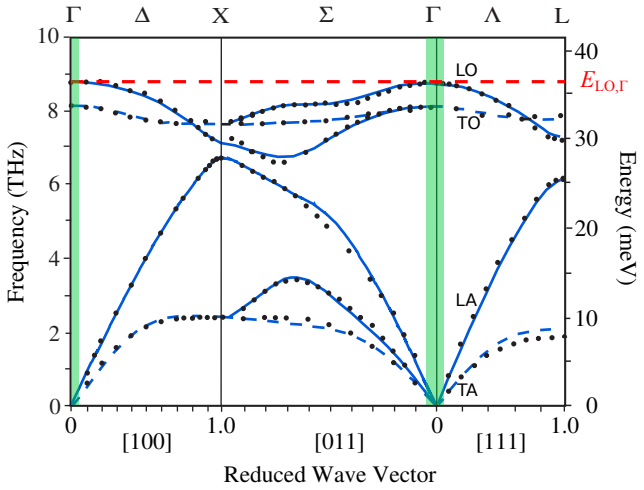


Figure 2.5: Phonon dispersion curves for GaAs along the high-symmetry directions $[100]$, $[011]$ and $[111]$. The experimental data points were measured by inelastic neutron scattering at 12 K. The lines represent calculations with an 11-parameter rigid-ion model. The letters on top of the figure name the directions and points in $k$-space. Longitudinal and transverse optical modes as well as longitudinal and transverse acoustic modes are labeled by LO, TO, LA and TA, respectively. The reduced wave vector is given in fractions of the Brillouin-zone size in the corresponding direction. The green-shaded areas around the Γ-point highlight the innermost 5% of the first Brillouin zone, which is the relevant range for electron–phonon interaction in the electron-energy range below $\approx 60\,\mathrm{meV}$. The dashed line at $E_{\mathrm{LO},\Gamma}$ marks the energy of LO phonons at the Γ-point, which plays an important role for electron energy dissipation. The figure was adopted in parts from [SD90].

phonon modes are important for electron cooling but they contribute quite differently.

Long-wavelength optical phonons in GaAs have an energy of $33.8\,\mathrm{meV}$ for the transverse and $36.7\,\mathrm{meV}$ for the longitudinal mode [Bla87]. The interaction between electrons and transverse optical (TO) phonons is suppressed because of the $s$-symmetry of the conduction-band states at $k = 0$ [Lyo86]. Electrons interact with longitudinal optical (LO) phonons through the *Fröhlich interaction*. The threshold for the emission of optical phonons is therefore determined by the energy of the longitudinal mode $E_{\mathrm{LO},\Gamma} = 36.7\,\mathrm{meV}$ (dashed red line in figure 2.5). Due to the flatness of the LO-phonon dispersion, this emission threshold is relatively sharp and the energy dissipated by high-energetic electrons through LO-phonons is quantized in steps of $E_{\mathrm{LO},\Gamma}$. Furthermore, LO-phonon emission is an inherently fast process which takes place on a sub-picosecond time scale [Lyo86].

LO-phonon emission is the dominant cooling mechanism for high-energetic hot electrons. However, conduction electrons below $E_{\mathrm{LO},\Gamma}$ can still be very hot with respect to the lattice, but emission of LO-phonons is not possible in this energy range. Here, the interaction with acoustic phonons provides further intra-band relaxation. According to the energy–momentum dispersion of acoustic phonons, an electron below $E_{\mathrm{LO},\Gamma}$ can lose only about 3% of its energy by back-scattering an acoustic phonon. Electron–acoustic-phonon interaction is therefore rather inefficient at cooling hot electrons. Energy

relaxation through acoustic-phonon emission takes place on a nanosecond timescale [Ulb73], which is comparable to the radiative lifetime of nonequilibrium charge carriers (about 7 ns in GaAs [Bla87]).

Due to the different contributions of optical and acoustical phonons, the conduction-band energy scale is roughly divided into two regimes for hot-electron relaxation. Above $E_{\mathrm{LO},\Gamma}$, fast LO-phonon emission cools electrons very efficiently, while below $E_{\mathrm{LO},\Gamma}$, acoustic-phonon emission is not fast enough to cool electrons down to lattice temperature during the radiative lifetime in the conduction band.

Hot electrons thermalize and reach a temperature $T_e$ that is larger than the lattice temperature $T_l$ if the energy exchange among them is faster than with the lattice. The rate of energy exchange through $ee$-scattering depends mainly on the electron density $n_e$, while the energy dissipation to the lattice depends strongly on the electron energy.[5] At very low electron densities ($\lesssim 10^{13}\,\mathrm{cm}^{-3}$), $ee$-scattering is even slower than energy dissipation through acoustic phonons. A thermal distribution with $T_e > T_l$ can therefore not be established during the radiative lifetime of nonequilibrium electrons. In the range of $10^{13}\,\mathrm{cm}^{-3} \lesssim n_e \lesssim 10^{16}\,\mathrm{cm}^{-3}$, electron energy exchange is faster than acoustic-phonon emission, but still much slower than LO-phonon emission. Consequently, a thermal distribution with $T_e > T_l$ is reached below $E_{\mathrm{LO},\Gamma}$, but not above $E_{\mathrm{LO},\Gamma}$, where LO-phonon emission efficiently depletes the electronic states at these densities. Above $10^{18}\,\mathrm{cm}^{-3}$, $ee$-scattering and LO-phonon emission become comparable in the vicinity of $E_{\mathrm{LO},\Gamma}$.

At low temperatures ($k_B T_l << E_{\mathrm{LO},\Gamma}$) and sufficient but moderate electron densities ($n_e$ between $10^{13}\,\mathrm{cm}^{-3}$ and $10^{17}\,\mathrm{cm}^{-3}$), a Maxwell-Boltzmann thermal distribution with $T_e > T_l$ can be expected below $E_{\mathrm{LO},\Gamma}$ for continuous excitation [SL69, MS81, Ehr60, Ulb73, Lyo86, GH78]. A stable electron temperature $T_e$ is reached under steady-state conditions when the cooling through phonon emission exactly balances the heating through optical excitation. Here, it is important to distinguish the initial excess energy $E_e$ (equation 2.5) from the energy $E_{\mathrm{heat}}$, which each electron actually contributes to heat the thermal part of the distribution. If excitation takes place above $E_{\mathrm{LO},\Gamma}$, a rapid initial relaxation through LO-phonon emission occurs, which removes most of the excess energy before it is distributed among other electrons. For low electron densities, i.e. when LO-phonon emission is faster than $ee$-scattering, the net heating per photoexcited electron can be estimated as

$$E_{\mathrm{heat}} = E_e - nE_{\mathrm{LO},\Gamma} \tag{2.8}$$

where $n$ is the largest possible integer for which $E_{\mathrm{heat}}$ is positive. For larger densities, when $ee$-scattering above $E_{\mathrm{LO},\Gamma}$ becomes comparable to LO-phonon emission, $E_{\mathrm{heat}}$ increases above that value, but cannot exceed $E_e$, of course. Under real experimental conditions, the net heating is somewhere between these boundaries. For excitation below $E_{\mathrm{LO},\Gamma}$, no initial relaxation through optical phonons can take place, and $E_{\mathrm{heat}}$ assumes its maximum value $E_e$.

For Maxwell-Boltzmann distributed electrons, an average energy-dissipation rate per electron can be calculated with equations given by ULBRICH [Ulb73]. Here, three mechanisms of electron–phonon interaction are taken into account. These are the *piezoelectric* (pe) and the *acoustic deformation-potential* (ac) scattering for the acoustic modes and the *polar-optical* (po) scattering (Fröhlich inter-

[5] $n_e$ includes both intrinsic and nonequilibrium conduction electrons.

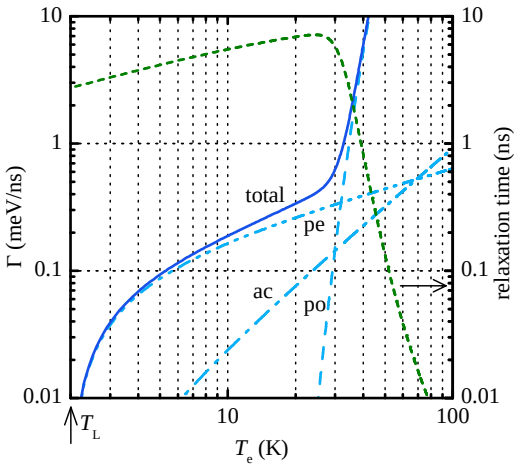


Figure 2.6: Energy relaxation rate per electron calculated for a Maxwell-Boltzman distribution with electron temperature $T_e$ and a lattice temperature of 2 K. The blue broken curves reflect the contributions from piezoelectric (pe), acoustic-deformation-potential (ac) and polar-optical (po) scattering. The solid blue curve shows the sum of these contributions. The green dashed curve shows the total energy dissipation expressed as a relaxation time. Note the marked onset of polar-optical scattering at around $T_e \approx 30\,\mathrm{K}$.

action) for the LO mode. The corresponding scattering rates can be written[6]

$$\Gamma_{\mathrm{po}} = \frac{\sqrt{2m_e}e}{4\pi\epsilon\hbar^2}\left(\epsilon_\infty^{-1} - \epsilon_0^{-1}\right) E_{\mathrm{LO},\Gamma}^{3/2}\left[\exp\left(-\frac{E_{\mathrm{LO},\Gamma}}{k_B T_e}\right) - \exp\left(-\frac{E_{\mathrm{LO},\Gamma}}{k_B T_l}\right)\right] \tag{2.9}$$

$$\Gamma_{\mathrm{pe}} = \frac{1}{e(4\pi\epsilon)^2}\left(\frac{64\pi^{1/2}e^2e_{14}^2m_e^{3/2}a(k_BT_e)^{1/2}}{\sqrt{2}\hbar^2\epsilon_0^2\rho}\right)\left(\frac{T_e - T_l}{T_e}\right) \tag{2.10}$$

$$\Gamma_{ac} = \frac{1}{e}\left(\frac{8\sqrt{2}E_1^2m_e^{5/2}(k_BT_e)^{3/2}}{\pi^{3/2}\hbar^4\rho}\right)\left(\frac{T_e - T_l}{T_e}\right) \tag{2.11}$$

where $\epsilon_\infty$ and $\epsilon_0$ are the high- and low-frequency dielectric constants of the material, while $\epsilon$ is the free-space permittivity. $e_{14}$ and $E_1$ denote the piezoelectric coupling constant and the deformation-potential constant, respectively. $\rho$ is the mass density of the crystal and $a$ is a dimensionless factor introduced and estimated to $\approx 0.4$ by S. M. KOGAN [Kog63]. The total energy-dissipation rate per electron is simply the sum of all contributions

$$\Gamma_{\mathrm{total}} = \Gamma_{\mathrm{po}} + \Gamma_{\mathrm{pe}} + \Gamma_{\mathrm{ac}} \tag{2.12}$$

Figure 2.6 shows the energy-dissipation rates as function of the electron temperature $T_e$ calculated for GaAs conduction electrons at a lattice temperature of 2 K. Note the knee in the total dissipation rate at $\approx 30\,\mathrm{K}$, which originates from the onset of LO scattering in the high-energy tail of the distribution. The relaxation time plotted in figure 2.6 was calculated as

$$\tau_{\mathrm{thermal}} = \frac{3}{2}\frac{k_BT_e}{\Gamma_{\mathrm{total}}} \tag{2.13}$$

This curve shows that the relaxation time drops quickly to the sub-nanosecond scale with the onset of LO scattering, which is faster than radiative recombination. Consequently, the electron ensemble can relax completely for lattice temperatures above $\approx 30\,\mathrm{K}$, while it stays permanently overheated at lower lattice temperatures. The experimental observations discussed in chapter 3.4 agree nicely with this interpretation.

[6] These equations were converted from the cgs form to SI units and yield electronvolts per second.

In the present work, the luminescence of the free-electron–neutral-acceptor transition $(e, A^0)$ is measured in order to determine the temperature of conduction electrons. Due to the strong localization of the acceptor wave function in real space, the quantum-mechanical uncertainty principle dictates a broad distribution in $k$-space. Wave-vector conservation is therefore effectively suspended for radiative recombination of conduction electrons with acceptor-bound holes. This is also the reason for the considerable spectral weight of free-to-bound transitions, even at small impurity concentrations.

The dipole-transition probability of $(e, A^0)$ can be assumed to be constant in the small region of interest around the $\Gamma$-point. Therefore, when assuming a Maxwell-Boltzmann energy distribution within the conduction band, the spectral intensity is well approximated by

$$I(E) = I_0 \sqrt{E - (E_{\text{gap}} - R^*)} \, \exp\left[ -\frac{E - (E_{\text{gap}} - R^*)}{k_B T_e} \right] \tag{2.14}$$

where the square root reflects the 3D density of states, $R^*$ represents the acceptor ground-state binding energy and $I_0$ includes all constant factors. In chapter 3.4, electron temperature measurements $T_e$ are obtained by fitting equation 2.14 to experimental data.

## 2.5 Optical spin orientation

At the $\Gamma$-Point, optical selection rules can be formulated analogous to electronic transitions in atoms. In the dipole approximation, the initial and final states must be of different parity in order to yield a non-zero transition probability. This implies that the orbital quantum number must change by $\Delta l = \pm 1$. Furthermore, conservation of angular momentum dictates a strong correlation between the $z$-projection of the total angular momentum, $m_j$, and the polarization state of absorbed or emitted light. Photons carry a spin (helicity) of $\pm 1$ for left and right circular polarization, respectively, and the projection onto the direction of propagation is $\pm\hbar$. Linearly polarized light can be understood as a coherent superposition of left and right circular polarizations, where the net spin $z$-projection amounts to zero. Therefore, $\Delta m_j$ must be $\pm 1$ for transitions involving circularly polarized light, and zero for linear polarization.

Circularly polarized light is routinely used for spin-selective excitation of electrons. This effect is based on different transition probabilities into states of opposing spin orientation. The expected ratio of the transition rates is proportional to the ratio of the transition dipole moments. Figure 2.7 summarizes these ratios for interband transitions at the $\Gamma$-point involving circularly polarized light. Since for the calculation of these numbers purely $s$- and $p$-like states are assumed, they are, strictly speaking, only valid at $k = 0$. However, at small but finite $k$, these values are still a good approximation, because the transition dipole moments vary only slowly with $k$.

From the numbers in figure 2.7 it becomes clear, that circularly polarized light excites three times as many electrons from the $|3/2, \pm 3/2\rangle$ valence band state to the $|1/2, \pm 1/2\rangle$ conduction band state as from $|3/2, \pm 1/2\rangle$ to $|1/2, \mp 1/2\rangle$. Consequently, if excitation takes place only from the heavy and light hole bands and not from the spin–orbit split-off band (SO), the excited conduction band electrons have a preferred spin orientation. The *net spin polarization* along the propagation direction of light

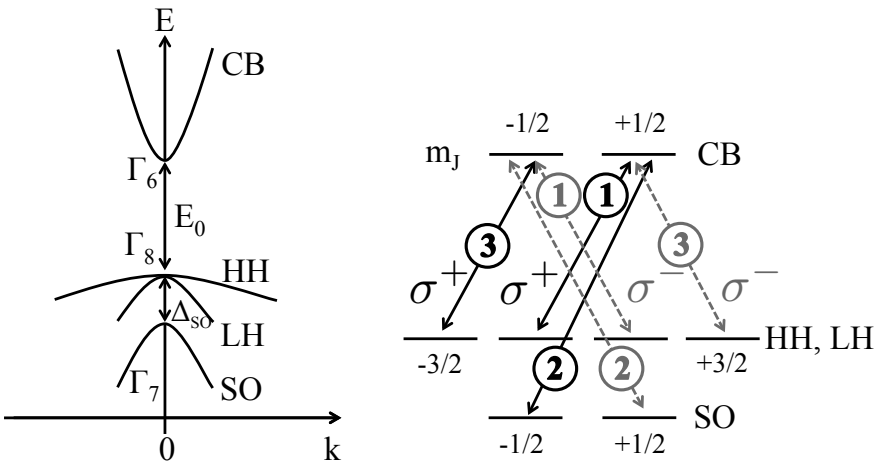


Figure 2.7: Allowed optical transitions between $p$-like valence band states and $s$-like conduction band states for interaction with circularly polarized light. The numbers in circles denote the relative transition probabilities as obtained from symmetry considerations alone. Note that only transitions with $\Delta m_j = \pm 1$ are allowed, due to the conservation of angular momentum.

can be expressed by the densities of spin-up ($n_\uparrow$) and spin-down ($n_\downarrow$) electrons as

$$S_z = \frac{n_\uparrow - n_\downarrow}{n_\uparrow + n_\downarrow} \tag{2.15}$$

For the theoretically predicted maximum ratio of 3:1, a net spin polarization of 50% is expected.

If excitation takes place from all six valence band states, the expected spin polarization should be zero, because both $m_j$-states in the conduction band become populated equally. Therefore, optical spin orientation is preferrably performed with photon energies between $E_{\text{gap}}$ and $E_{\text{gap}} + \Delta_{\text{SO}}$. However, although the interband matrix elements vary only slowly with $k$, it was shown that the net spin polarization decreases noticably with increasing excitation energy [MZ84, Qua07]. Furthermore, optical spin pumping at energies above $E_{\text{gap}} + \Delta_{\text{SO}}$ yields non-zero spin polarizations, against naive expectations. The following discussions will be limited to photon energies well below $E_{\text{gap}} + \Delta_{\text{SO}}$, where the experimentally obtained net spin polarization is $\gtrsim$20%.

In $n$-type GaAs, optically oriented electrons can relax into donor states, where the spin information can be preserved for rather long durations. Under steady-state conditions, recombination of donor electrons with valence-band holes takes place continuously, and therefore, non-spin-polarized donor electrons are partially replaced by spin oriented ones. This process of spin accumulation on donor states is termed *optical spin pumping*.

## 2.6 Spin dynamics

A mathematical description of the spatio-temporal dynamics of a nonequilibrium spin polarization or magnetization $\boldsymbol{M}$ in a magnetic field $\boldsymbol{B}$ is given by the Bloch-Torrey equations [Blo46, Tor56]:

$$\begin{aligned}
\frac{\partial M_x}{\partial t} &= \gamma(\boldsymbol{M} \times \boldsymbol{B})_x - \frac{M_x}{T_2} + \nabla D \nabla M_x \\
\frac{\partial M_y}{\partial t} &= \gamma(\boldsymbol{M} \times \boldsymbol{B})_y - \frac{M_y}{T_2} + \nabla D \nabla M_y \\
\frac{\partial M_z}{\partial t} &= \gamma(\boldsymbol{M} \times \boldsymbol{B})_z - \frac{M_z - M_{z0}}{T_1} + \nabla D \nabla M_z
\end{aligned} \tag{2.16}$$

Here, the cross-product terms represent precession of spins with the Larmor frequency $\omega = \gamma B$, where the gyromagnetic ratio $\gamma = \mu_B g/\hbar$ is defined through the Bohr magneton $\mu_B$ and the Landé $g$-factor. Due to fluctuations of the Larmor frequency, spins perform a random walk in phase-space. Thereby, coherence is lost on a timescale $T_2$, which is called *spin dephasing time*. The relaxation of $\boldsymbol{M}$ towards the thermal equilibrium state $M_{z0}$ takes place on a timescale $T_1$, which is known as *spin relaxation time*. In contrast to the process of dephasing, which conserves the total energy of the spin ensemble, relaxation involves a transfer of energy from the spin system to the environment. The diffusion terms on the right hand side of equation 2.16 are characterized by the isotropic diffusion coefficient $D$, and originate from a two-current model formulated by H. C. TORREY [Tor56].

Mathematically, the spin dephasing time $T_2$ is well defined only for a homogeneously broadened distribution of precession frequencies. However, inhomogeneous contributions are present in many experimental situations. In these cases the measured effective spin dephasing time is then denoted $T_2^*$ for clarity. In semiconductor systems at moderate magnetic fields (up to several Tesla), even $T_1$ and $T_2$ can usually be assumed to be equal, and a single spin relaxation time $\tau_s$ is introduced for the sake of simplicity [ŽFS04].

The Bloch-Torrey formalism was originally formulated for nuclear magnetic resonance experiments, in which $\boldsymbol{B}$ is traditionally composed of a strong static component $B_0\hat{\mathbf{z}}$ and a much smaller time dependent contribution $\boldsymbol{B}_1(t)$ in the equatorial plane. In the context of spin-imaging experiments, an alternative mathematical representation is more commonly used. When optical spin orientation and observation take place under normal incidence of light onto the surface of an isotropic sample, it is usually sufficient to distinguish an out-of-plane and an in-plane spin component. For convenience, a complex spin density $S$ is introduced, which represents these two spin components by its real and imaginary part, respectively. For an in-plane magnetic field, precession, relaxation, and diffusion of the spin density $S$ are then described by the complex partial differential equation (PDE)

$$\frac{\partial S}{\partial t} = G_s - S/\tau_s + i\omega S + \nabla D_s \nabla S \tag{2.17}$$

Here, $G_s$ is the generation term, which represents the source of spin polarization, $\omega$ is the spin precession frequency, $\tau_s$ is the spin relaxation time and $D_s$ is the spin diffusion coefficient. When spin pumping is performed with continuous excitation, $S$ has no explicit time dependence, and therefore, both sides of equation 2.17 are zero (steady-state condition).

Figure 2.8 illustrates the effects described by equation 2.17 for local optical spin orientation. Spins

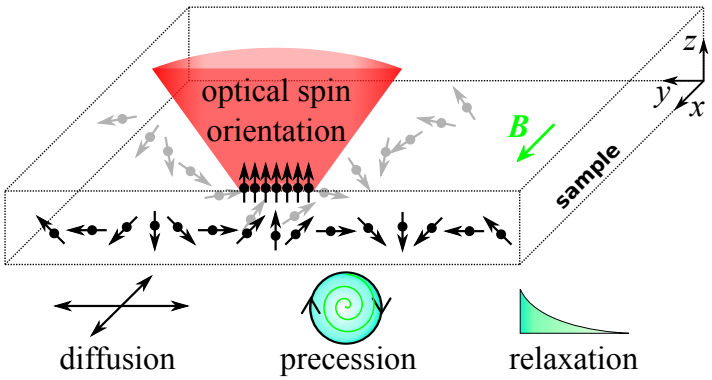


Figure 2.8: Illustration of diffusion, precession, and relaxation under local optical spin orientation. Spins are initially oriented along the $z$-direction by circularly polarized light under normal incidence on the sample surface. When a magnetic field $\boldsymbol{B}$ is applied in $x$-direction, spins precess in the $yz$-plane. The real and imaginary parts of the complex spin density $S$ describe the out-of-plane ($z$) and in-plane ($y$) spin components, respectively.

are initially oriented along the $z$-direction, which corresponds to the real part $S_z$ of the complex spin density $S$. When a magnetic field is applied in $x$-direction spins precess in the $yz$-plane. Due to this precession, the in-plane spin component $S_y$ becomes nonzero, which corresponds to the imaginary part of $S$.

Equation 2.17 presents a basic mathematical model for the description of spin relaxation–diffusion phenomena in the geometry described above. For a comparison between this model and experimental data, an explicit expression for $S(\boldsymbol{r})$ is needed. In general, there are two ways to obtain one, the analytical and the numerical approach. In the following, an analytical solution is presented, which is unfortunately too restrictive for the goals of this work. For the sake of flexibility with regard to lateral variations of the coefficients in equation 2.17, the *finite elements method* (FEM) was used to obtain numerical solutions efficiently and with good accuracy.

The characteristic length scale for diffusion–relaxation processes according to equation 2.17 is the spin diffusion length $l_s = \sqrt{D_s \tau_s}$. If the lateral extent of the generation term $G_s$ is much smaller than $l_s$, the solution of equation 2.17 can be obtained approximately by a Greens-function approach, where the inhomogeneity $G_s$ is reduced to a $\delta$-function $G_s(r) = G_{s0}\delta(r)$. In general, the lateral amplitude of $G_s$ is denoted $G_{s0}$. The generation term expresses the rate of spin orientation per unit volume. Moreover, if experiments are performed on a thin layer, with a thickness much smaller than $l_s$, it is sufficient to consider the in-plane lateral dependence of $S$. Moreover, if no anisotropies are present, the problem can be reduced further to one radial dimension.[7] The steady-state Greens-function solution of equation 2.17 for the two-dimensional case with radial symmetry can be expressed in terms of the Bessel-$K$ function $K_0$ as

$$S(r) = \frac{G_{s0}}{2\pi D_s} K_0 \left( r \sqrt{\frac{1}{D_s \tau_s} + \mathrm{i} \frac{g \mu_B B}{\hbar D_s}} \right) \tag{2.18}$$

[7] Anisotropic behavior can be induced externally through application of mechanical strain or an electrical field. Investigations in this direction can be found in [CS05] and [FSK+07].

The lateral shape and extent of the generation term can be taken into account by convoluting this solution with the original $G_s(r)$.

In order to account for electron heating caused by optical spin pumping, lateral variations of the coefficients in equation 2.17 must be considered. Especially the spin diffusivity obtains a lateral dependence $D_s(\boldsymbol{r})$ due to the optical heating of conduction electrons, which is shown in chapter 3.4. Note that the above form of equation 2.17 allows this, while the diffusion term more frequently given in the literature, $D_s\nabla^2 S$, implicitely assumes a homogeneous diffusion coefficient by permuting $D_s$ and the nabla operator [FSK$^+$07, FMAE$^+$07]. In the case of a lateral dependence of the diffusivity, an analytic solution of equation 2.17 is neither generally known, nor easily calculated. Here, a finite element solver is a convenient tool for calculating numerical solutions with good accuracy and low computational cost.

A finite element calculation operates on the spatial domain by dividing it into a triangular mesh. This structure is usually homogeneous in the beginning and adapted to local gradients in the course of the calculation. Thereby, and with the help of a set of arbitrary square-integrable test functions, the PDE under consideration is transformed into a set of integral equations. Based on the mesh, the solution function and the test functions are piecewise linearly approximated. This yields a system of linear equations from which the solution allows the approximate reconstruction of the PDE solution. A comprehensible introduction into FEM is given in [Say08]. The method is used in chapter 4.4 to obtain lateral profiles of the nonequilibrium spin density from various diffusion models.

## 2.7 Electron spin relaxation in semiconductors

For GaAs and other zinc-blende-type semiconductors, established literature distinguishes several mechanisms that cause relaxation of nonequilibrium electron spins [ŽFS04]. These are the *Dyakonov-Perel* [DP71], *Elliot-Yaffet* [Ell54, Yaf63], and *Bir-Pikus* [BAP75] *mechanisms* as well as the *hyperfine* and *anisotropic exchange* [Kav08] *interactions*. The relevance of each depends on material properties like band gap energy, spin-orbit coupling, and the doping conditions, as well as external influences like temperature or strain.

For localized charge carriers, as found at doping concentrations below the MIT and low temperatures, the dominant mechanism of spin relaxation in GaAs is the hyperfine interaction. Here, electrons are trapped quickly by impurities, which allows electron spins to interact only with a local subensemble of nuclear spins. From site to site, the magnetic field of the limited number $N$ of nuclear spins is subject to fluctuations proportional to $\sqrt{N}$. These lateral variations lead to a lateral variance of the spin precession frequency, which causes spin dephasing.

As electrons become more mobile due to increased doping or temperature, spin dephasing by hyperfine interaction is suppressed due to an effect called *motional narrowing*. This effect addresses the narrowing of the distribution of spin precession frequencies due to the delocalization of electrons. Itinerant electrons interact with a much larger number of atomic nuclear spins over time than localized ones, which efficiently smoothes the fluctuations of the nuclear magnetic field.

For the metallic regime, DYAKONOV and PEREL proposed spin relaxation through $k$-dependent

precession during phases of ballistic propagation. Due to the Dresselhaus spin-orbit interaction, conduction band electrons feel a magnetic field which in strength and direction depends on the electron wave vector. If the total scattering rate is low, electrons precess about their individual Dresselhaus fields for rather long times. Like in the case of hyperfine interaction, these individual precession frequencies lead to the dephasing of spins. On the other hand, if scattering times are short, motional narrowing suppresses this dephasing. Here, the localization that leads to spin dephasing, as well as the effect of motional narrowing take place in $k$-space.

In the intermediate regime, where donor density and temperature allow tunneling between neighbouring donors but not yet free movement of electrons, it was proposed by K. V. KAVOKIN that the anisotropic exchange interaction causes spin dephasing [Kav01]. He showed mathematically that the process of tunneling electron exchange between donor sites yields a phase shift of the spin wave function. Since this phase shift depends on the distance between the donor sites of origin and destination, this effect also causes spin dephasing.

The Elliot-Yaffet mechanism is predominantly responsible for the extremely short spin memory of valence band holes in GaAs and other zinc-blende-type semiconductors. Here, spin–orbit coupling causes a mixing of spin states, which leads to a finite probability for spin flips upon scattering with phonons or impurities. Since these spin flips occur randomly, they cause spin relaxation. For holes in the valence band, practically every scattering event has a chance to flip the spin. Theoretically, this effect should vanish for conduction band electrons, due to the s-like symmetry and the absence of orbital angular momentum. However, because of the finite admixture of valence band states at finite $k$, the probability for a conduction band electron to flip its spin upon scattering is approximately $10^{-5}$ in GaAs. This effect scales inversely with the energy gap and is therefore most pronounced for narrow-gap materials [FMAE$^+$07].

The Bir-Aronov-Pikus (BAP) mechanism describes relaxation of electron spins, mediated by the exchange interaction with valence band holes. Spin exchange between electrons as well as between electrons and holes initially preserves the total spin. Among electrons, the total spin of the ensemble is not affected by exchange scattering. However, if an electron and a hole exchange spins, the hole loses the spin information quickly due to the Elliot-Yaffet mechanism. Therefore, the Bir-Aronov-Pikus meachanism depends strongly on the density of holes. Sufficient numbers are not only reached in $p$-doped materials, but also under strong optical excitation.

Figure 2.9 presents an overview of the doping dependence of the spin relaxation time in $n$-type GaAs at low temperatures. In the insulating regime below $\approx 3 \times 10^{15}\,\mathrm{cm}^{-3}$, electrons are trapped at donor sites and spin relaxation is dominated by the hyperfine interaction. In the metallic regime above $\approx 2 \times 10^{16}\,\mathrm{cm}^{-3}$, the donor wave functions overlap and allow electrons to move more freely even at low temperatures. In the intermediate regime the donor wave functions overlap slightly, which allows tunneling of electrons between donor sites. This gives rise to spin relaxation by anisotropic exchange interaction. The overview from [DKK$^+$02] demonstrates that $n$-GaAs at the MIT is a promising material for spintronics research and applications, due to rather long spin relaxation times of up to a few hundred nanoseconds.

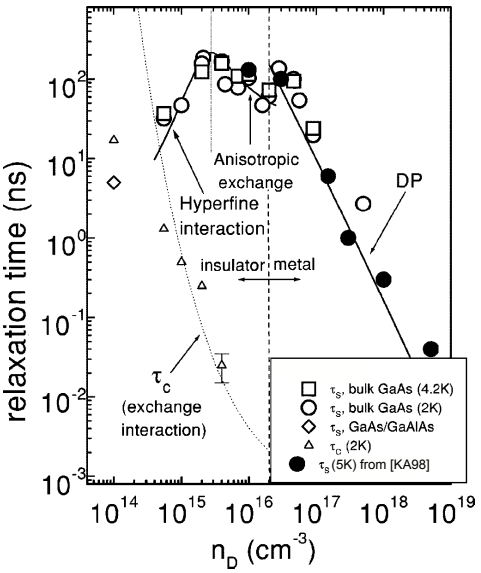


Figure 2.9: Doping dependence of the spin relaxation time in the vincinity of the metal-to-insulator transition. The solid lines represent theoretical calculations and the dashed vertical line indicates the MIT. This graph was taken from [DKK+02] and modified.

## 2.8 The Hanle effect

In 1924, W. HANLE observed the quenching of optical luminescence polarization by an external magnetic field. This effect originates from the combination of precession and dephasing of spins in the magnetic field. Therefore, equations 2.16 and 2.17 can be used for a mathematical description. The Hanle effect is frequently used for the experimental determination of spin relaxation times without explicit temporal resolution, i.e under steady-state conditions.

The Hanle effect can be understood in the following way. For continuous spin injection, i.e. steady state excitation, spins are oriented at random times, initially pointing in the direction dictated by the source. In the temporal domain, the probability for an individual spin to have maintained its polarization after a time $t$ decays exponentially with a characteristic timescale $\tau_s$. If a magnetic field is applied, spins start to precess in the plane transverse to the magnetic field immediately after excitation. Therefore, the expectation value of an individual spin describes a damped oscillation within this plane. Due to the random starting times of the individual spins, their phases are distributed randomly. In order to obtain the ensemble averaged spin in the steady-state situation, one must integrate this damped oscillation over time. This yields the steady-state spin polarization $S$ as function of the external magnetic field. The corresponding *Hanle curve* can be described by a Lorentz curve. Finally, the decay time is obtained from the measured half width of the Hanle curve.

Traditionally, the Hanle effect is observed without spatial inhomogeneities, i.e. drift and diffusion can be neglected. This situation is achieved if the injection and detection volume are much larger than the spin diffusion and drift lengths. On the other hand, it is possible to observe a *local* Hanle effect in spin imaging experiments. However, since in this situation diffusion accounts for an additional local spin loss or gain, it is not possible to deduce a local spin relaxation time hereby.

Neglecting diffusion and the spatial dependence, the magnetic-field dependence of the steady-state

solution of equation 2.17 reads

$$S(B) = \frac{S_0 \left(1 + \mathrm{i}\omega\tau_s\right)}{1 + \left(\omega\tau_s\right)^2} \tag{2.19}$$

where $S_0$ is the zero field net spin polarization, which points in $z$-direction. The real part, which is the $z$ component of the spin, describes the Hanle curve. The spin relaxation time is deduced from experimental data in the following way. The real part of equation 2.19 drops to one half of its initial value, when $\omega\tau_s$ reaches 1. In this case, $\omega$ equals $g\mu_B B/\hbar$, and the spin relaxation time can be calculated as

$$\tau_s = \frac{\hbar}{g\mu_B B_{1/2}} \tag{2.20}$$

where $\mathrm{Re}(S(B_{1/2})) = \mathrm{Re}(S_0)/2$. The half width $B_{1/2}$ is usually determined by a least-squares fit of equation 2.19 to the experimental data.

Strictly speaking, this method does not directly yield the spin relaxation time $\tau_s$, but instead a spin lifetime $T_s$, which also includes other spin loss channels like electron–hole recombination. Another effect due to the presence of valence band holes is the Bir-Aronov-Pikus mechanism described above. Experimentally, both influences are usually taken into account by extrapolating the Hanle-curve half width $B_{1/2}$ to the limit of zero optical power.

## 2.9 Magneto-optic effects and polarized light

In 1845, M. FARADAY observed that the polarization of light is changed by the propagation through a transparent medium in a magnetic field [Far33]. Some time later, in 1876, J. KERR discovered that the polarization state also changes when light is reflected by a ferromagnetic solid [Ker76]. Both effects can be described uniformly in terms of *magnetic circular birefringence* and *magnetic circular dichroism*.

Magnetic circular birefringence and dichroism describe the spectral splitting of the dielectric response function $\epsilon(\omega)$ with respect to the circular eigenmodes of the electric field, due to the presence of a magnetic field. Here, birefringence and dichroism refer to the change of the real and imaginary parts of the complex refractive index $\tilde{n} = \sqrt{\epsilon}$, respectively. Both effects are summarized as the *magneto-optical response function*

$$\Delta\tilde{n} = \tilde{n}_\mathrm{r} - \tilde{n}_\mathrm{l} \tag{2.21}$$

where $\tilde{n}_\mathrm{r,l} = n_\mathrm{r,l} - \mathrm{i}\kappa_\mathrm{r,l}$ are the complex refractive indices for left- and right-handed circular polarizations with the corresponding real refractive indices $n_\mathrm{r,l}$ and the absorption coefficients $\kappa_\mathrm{r,l}$.

In a semi-classical picture, circular birefringence and dichroism can be interpreted in the following way. Due to the Lorentz force, the electrons in a medium perform a spiral motion around the magnetic field lines. In the reference frame of the electrons, the optical frequencies of left- and right-handed polarizations appear shifted against each other, due to the Doppler effect. Consequently, the dispersion and absorption functions of the medium are splitted with respect to the handedness of the polariza-

tion. In quantum-mechanical terms, the magnetic field lifts the degeneracy of the angular-momentum states $m_J$. According to the selection rules for optical dipole transitions, this leads to an energetic splitting of the dielectric response function. The magnetic circular birefringence and dichroism are differential effects, which means that their magnitude scales with the spectral slope of the complex refractive index.

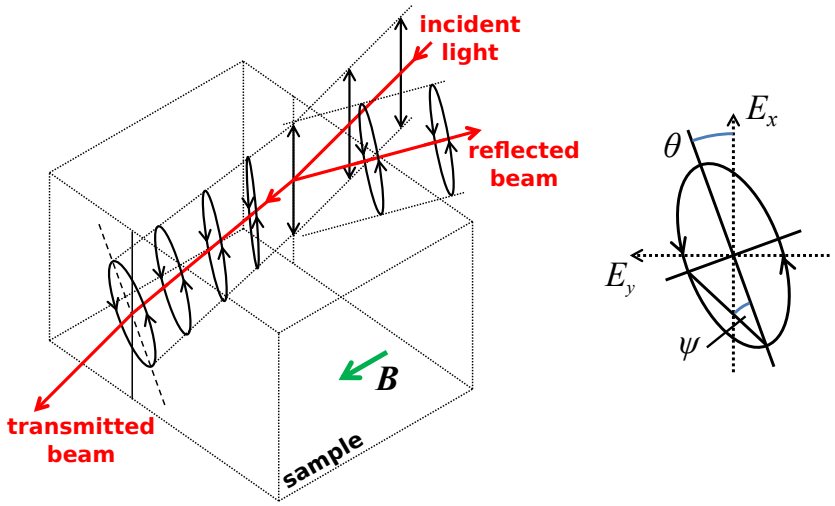


Figure 2.10: Schematic illustration of the magneto-optical effects. Linearly polarized light penetrates a magnetized transparent medium. The magnetic flux $\boldsymbol{B}$ can be of external origin or caused by an internal magnetization of the medium. The transmitted and reflected light beams are subject to the Faraday and Kerr effects, respectively. When leaving the medium, both beams have assumed an elliptical polarization state. Aside from intensity changes, the resulting polarization state of each beam can be described by a rotation angle $\theta$ of the main axis and an ellipticity $\pm \tan \psi$, where the $+$ and $-$ signs correspond to right- and left-handed polarizations, respectively. Note that the angle of incidence has been chosen to deviate from the surface normal for visual clarity only.

The polarization state of an electromagnetic wave can be visualized by the trajectory of the electric field vector $\boldsymbol{E}$ at a fixed point in space. In general, if a plane wave is propagating in $z$-direction, $\boldsymbol{E}$ describes an ellipse in the transverse $xy$-plane. Neglecting the absolute phase and amplitude of the wave, this *polarization ellipse* is fully described by an azimuth angle $\theta$ with respect to a fixed $x$-axis and an ellipticity $\pm \tan \psi$. The $+$ and $-$ signs correspond to right- and left-handed polarization states, respectively. The right hand side of figure 2.10 illustrates an arbitrary elliptical polarization. The concepts for the description and measurement of polarized light are described in detail in [AB77].

The left part of figure 2.10 illustrates the interaction of linearly polarized light with a transparent medium in a magnetic field $\boldsymbol{B}$. The linear input polarization can be constructed as a superposition of two copropagating circularly polarized waves of the same amplitude and phase but with opposite parity. The transmitted beam experiences a phase shift between these circular components due to the magnetic circular birefringence and a change of the amplitude ratio due to the magnetic circular dichroism. The phase shift rotates the main axis of polarization and the difference in absorption introduces an ellipticity. In transmission, the *Faraday rotation* $\theta_\mathrm{F}$ and the *Faraday ellipticity* $\psi_\mathrm{F}$ are

directly related to the magnetic circular birefringence and dichroism, respectively. For the reflected beam the situation is slightly more complicated. Expressions for the *Kerr rotation* $\theta_{\mathrm{K}}$ and the *Kerr ellipticity* $\psi_{\mathrm{K}}$ can be obtained from the complex reflection coefficients for left and right circularly polarized light. For normal incidence of light onto a sample in vacuum the reflection coefficients read

$$\tilde{r}_{\mathrm{r,l}} = |r_{\mathrm{r,l}}|\, e^{\mathrm{i}\phi_{\mathrm{r,l}}} = \frac{1-\tilde{n}_{\mathrm{r,l}}}{1+\tilde{n}_{\mathrm{r,l}}} \tag{2.22}$$

The phase jump and absolute value can be expressed in terms of the real refractive index $n_{\mathrm{r,l}}$ and the absorption coefficient $\kappa_{\mathrm{r,l}}$ as

$$\phi_{\mathrm{r,l}} = \arctan\left(\frac{-2\kappa_{\mathrm{r,l}}}{n_{\mathrm{r,l}}^2+\kappa_{\mathrm{r,l}}^2-1}\right) \tag{2.23}$$

$$|r_{\mathrm{r,l}}| = \frac{\sqrt{\left(\kappa_{\mathrm{r,l}}^2+n_{\mathrm{r,l}}^2-1\right)^2+\left(2\kappa_{\mathrm{r,l}}\right)^2}}{\left(n_{\mathrm{r,l}}+1\right)^2+\kappa_{\mathrm{r,l}}^2} \tag{2.24}$$

The Kerr rotation and ellipticity can then be written

$$\theta_{\mathrm{K}} = -\frac{1}{2}\left(\phi_{\mathrm{r}}-\phi_{\mathrm{l}}\right) \tag{2.25}$$

$$\psi_{\mathrm{K}} = \frac{|r_{\mathrm{r}}|-|r_{\mathrm{l}}|}{|r_{\mathrm{r}}|+|r_{\mathrm{l}}|} \tag{2.26}$$

The experimental scheme described in chapter 4.1 aims at measuring these quantities with highest precision.

The expression for the phase jump ( equation 2.23) reveals that a finite absorption $\kappa_{\mathrm{r,l}} \neq 0$ is required in order to obtain a nonzero Kerr rotation. On the other hand, a Kerr ellipticity can be observed without absorption. This is easily seen when setting $\kappa_{\mathrm{r,l}} = 0$ in equation 2.24, which is thereby reduced to

$$|r_{\mathrm{r,l}}| = \frac{n_{\mathrm{r,l}}-1}{n_{\mathrm{r,l}}+1} \tag{2.27}$$

This consideration may be helpful in cases in which absorption of light might affect the measurement, for example due to optical heating or an increased charge carrier density.

The experiments in the present work employ the magneto-optic Kerr effect in the polar geometry. Here, light is reflected from the sample surface under normal incidence, in order to measure the optically induced electron spin polarization (see chapter 2.5). In the polar configuration, the measured Kerr rotation is commonly assumed to be proportional to the out-of-plane spin density (compare chapter 2.6 and figure 2.8)

$$\theta_{\mathrm{K}} \propto S_z \tag{2.28}$$

This relation was tested experimentally in chapter 4.1 based on the measurement of optically induced excitonic MOKE spectra. Indeed, the comparison between these data and numerical results obtained

from a simple oscillator model for the excitonic resonance confirms the validity of this assumption under the experimental conditions applied here.

The next chapter discusses photoluminescence experiments with a focus on the quantitative characterization of lateral temperature gradients due to local optical interband excitation.

# 3 Photoluminescence measurements of optical heating effects

The goal of the present chapter is the investigation of heating effects due to optical interband excitation. Special attention is paid to lateral temperature gradients under local excitation in order to evaluate their relevance and influence on optical spin studies. Here, two different aspects of optical heating are investigated. First, the temperature of the crystal lattice is traced by the luminescence of the acceptor-bound-exciton triplet lines ($A^0$,X). And secondly, the temperature of conduction electrons is extracted from the line shape of the conduction-band-to-acceptor luminescence. Both kinds of measurements put different demands on the employed experimental techniques as well as limitations on the investigated materials. The ($A^0$,X) investigations require a high spectral resolution, which restricts them to very pure, not intentionally doped samples. For the (e,$A^0$) line shape analysis a much more moderate spectral resolution suffices, but $n$-type doping also hinders evaluation in this case. In the course of this work, two different photoluminescence setups were developed in order to meet these requirements. The technical details are given in this chapter, which is organized in the following way: First, photoluminescence spectra of high and low-doped GaAs are presented and visible features are discussed. Secondly, measurements of the lateral lattice temperature are described. Here, the experimental setup is described first, followed by the discussion of data. Thirdly, the technical details of the experimental setup for spatio-spectral photoluminescence imaging are presented. The next section discusses lateral electron-temperature data obtained by this setup. This is followed by an analysis of the temperature dependence of optical electron overheating. Finally, a mathematical model of electron heat diffusion is postulated and discussed.

## 3.1 Near band-gap low-temperature photoluminescence in GaAs

The photoluminescence (PL) experimental technique is an all-optical nondestructive probe that is sensitive to the energetic structure and occupation of electronic states as well as optical selection rules. Here, light serves two purposes. First, electrons are excited from the ground state (valence band) to an energetically higher state by optical absorption. Secondly, the light produced by spontaneous emission is measured and analyzed spectroscopically.

Figure 3.1 shows a typical near band-gap low-temperature photoluminescence spectrum of high-purity GaAs (sample G, see appendix A). Due to the purity of the material, the spectrum exhibits a large number of well separated lines and bands.

Free electron–hole recombination (e,h) would be expected at $\gtrsim 1.518\,\mathrm{eV}$, i.e. above the band-gap energy. However, at this low temperature ($4.2\,\mathrm{K}$) the band-to-band luminescence is efficiently suppressed because most charge carriers are trapped into bound states before recombination. A weak band at around $1.518\,\mathrm{eV}$ could be associated with band-to-band transitions, but also with recombination of excited excitons $(FX)^*$ and excited donors $(D^0,h)^*$. Recombination of the free-excitons ground

state (FX) is visible as a pair of bands between 1.515 eV and 1.516 eV, correspondig to the upper and lower polariton branches as discussed in chapter 2.3. Directly below, the recombination of excitons bound to excited donors ($D^0$,X)* is weakly visible at 1.515 eV. The next two, clearly distinguished lines at 1.5145 eV and 1.5137 eV originate from excitons bound to neutral donors in the ground state ($D^0$,X) and excitons bound to ionized donors ($D^+$,X), respectively. The distinction between ($D^+$,X) and recombination of donor-bound electrons with free holes ($D^0$,h) is primarily of semantic nature. Both designations are used in the literature [HH74].

The three lines at 1.5131 eV, 1.5129 eV, and 1.5127 eV are associated with excitons bound to neu-

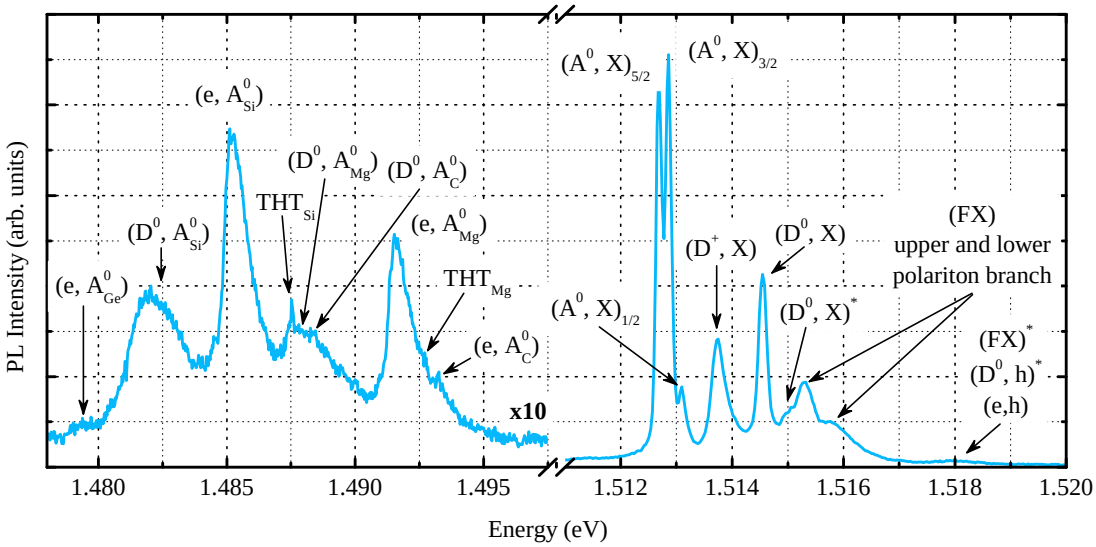


Figure 3.1: Photoluminescence spectrum of high-purity $p$-type GaAs (sample G, see table A.1). Bath temperature: 4.2 K, excitation energy: 1.577 eV ($\lambda = 786$ nm), laser power: 100 µW. The left part is scaled by a factor of ten. Visible features in the spectrum come from free excitons (FX), bound excitons (($D^0$,X) and ($A^0$,X)), free to bound transitions ((e,$A^0$) and ($D^0$,h)) and impurity pair transitions ($D^0$,$A^0$). Two hole transitions are labeled with THT.

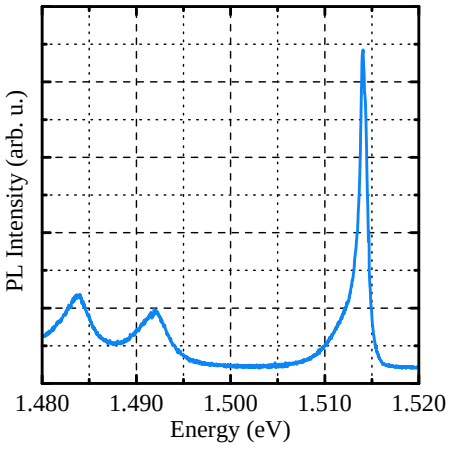


Figure 3.2: Photoluminescence spectrum of highly $n$-doped GaAs (sample C, see table A.1). Bath temperature: 1.6 K, excitation energy: 3.06 eV ($\lambda = 405$ nm), laser power: 10 µW, spot size: $\approx$ 200 µm. The two bands at around 1.484 eV and 1.492 eV originate from silicon and carbon acceptors, respectively. The peak at around 1.514 eV is associated with exciton and donor related transitions.

tral acceptors ($A^0$,X)$_J$.[1] The triplet structure originates from the different angular- momentum states $J = 1/2, 3/2, 5/2$ of the acceptor-bound hole. Since the occupation of these states is closely coupled to the temperature of the crystal lattice, it is possible to derive information about the latter from the relative spectral weights of the ($A^0$,X) triplet lines. This effect is exploited in the next section.

Transitions related to shallow acceptors are located in the lower part of the spectrum, due to the relatively large acceptor binding energies of approximately $25\,\mathrm{meV}$ to $40\,\mathrm{meV}$. For each acceptor species (i.e. C, Mg, Si and Ge in the present sample), there are two bands. The first band is the conduction-band-to-neutral-acceptor transition (e,$A^0$), with an onset energy of $E_{\mathrm{gap}} - E_{\mathrm{A}}$ and a lineshape following equation 2.14. The second band originates from neutral-donor-to-neutral-acceptor transitions ($D^0$,$A^0$). Its lineshape depends on the distribution of distances between donor and acceptor sites and is rather complicated to describe in mathematical terms [YC10].

Two hole transitions (THT) are duplicates of the acceptor-bound exciton ($A^0$,X), where the acceptor is left in an excited state. A THT is therefore shifted from the ($A^0$,X) downwards on the energy scale by the difference between the ground state and the first excited state. According to the Bohr model this amounts to $3/4$ of the corresponding acceptor binding energy.

For highly doped material like samples A to F (see table A.1) all of these sharp spectral features vanish and only a few broad bands remain. Figure 3.2 shows the photoluminescence spectrum of sample C. Closest to the band gap energy a relatively broad peak is formed by transitions related to donors and excitons. The other two bands can be roughly associated with silicon and carbon acceptors, respectively.

## 3.2 Spatial lattice-temperature tracing through acceptor-bound-exciton luminescence

The experimental setup shown in figure 3.3 was designed to combine high spectral resolution with lateral selectivity. The basic idea was to select the luminescence from a specific point on the sample by filtering an intermediate image through a pinhole. The observation spot was moved on the sample by scanning the focusing lens in the transverse plane. Due to the massive loss of light at the pinhole, the detector had to be as sensitive as possible. Therefore, a single-photon counting module (SPCM), based on a single channel avalanche photo diode, was chosen.

As a light source, a diode-pumped solid state laser (COHERENT CUBE) with an emission wavelength of $786\,\mathrm{nm}$ was used. The laser was filtered spectrally by a shortpass filter (THORLABS FEL800) in order to avoid non-coherent long-wavelength contributions from the laser. Furthermore, the laser was filtered spatially through a lens–pinhole–lens setup in order to achieve a clean $\mathrm{TEM}_{00}$ transverse mode for good focusing. A microscope objective (MITUTOYO M PLAN APO NIR 5X)

[1] HEIM and HIESINGER observed these lines at $1.5128\,\mathrm{eV}$, $1.5124\,\mathrm{eV}$ and $1.5122\,\mathrm{eV}$ at a temperature of $T = 1.6\,\mathrm{K}$. In figure 3.1 the weakest line with $J = 1/2$ is much closer to the other lines of the triplet than expected from these data. Ignoring this discrepancy and concentrating on the two stronger lines, the ($A^0$,X) spectrum in figure 3.1 is shifted by approximately $0.5\,\mathrm{meV}$ to higher energies with respect to the values from literature. The expected temperature change of the band gap (i.e. from $1.6\,\mathrm{K}$ in [HH74] to $4.2\,\mathrm{K}$ in figure 3.1) is by far too small ($0.04\,\mathrm{meV}$) to provide an explanation. Furthermore, it is highly unlikely that the here employed monochromator was misaligned by almost $3\,\mathrm{nm}$. Unfortunately, no satisfactory explanation can be given at this point.

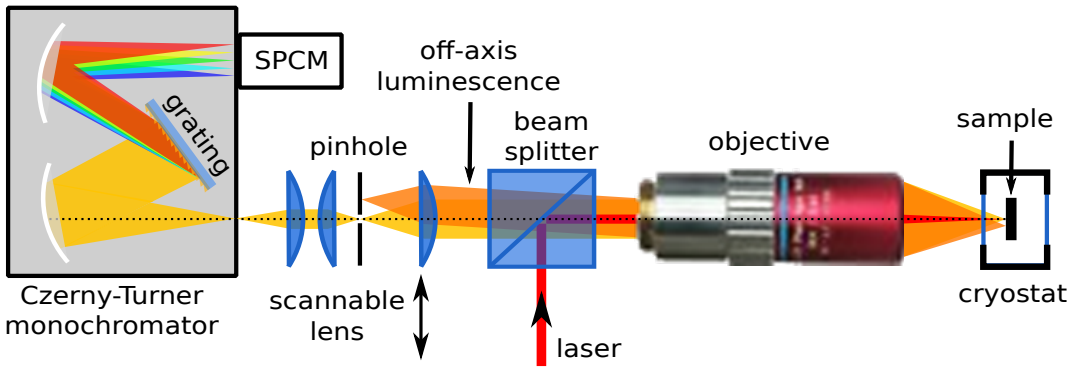


Figure 3.3: Experimental setup for spatially resolved photoluminescence measurements with a single-channel single-photon counting module (SPCM) and optical scanning mechanism.

was used to focus the laser on the sample surface to a spot size of $\approx 8\,\mu\mathrm{m}$ (1/e diameter).

The same objective was also used to collect the luminescence from the sample surface. An intermediate, magnified image of the luminescence was formed by a scannable lens and spatially filtered by a $30\,\mu\mathrm{m}$ pinhole. Two additional lenses collected the light from the pinhole and focused it onto the entrance slit of a Czerny-Turner monochromator (JOBIN YVON THR1000). Inside the monochromator, the light was collimated by a spherical mirror and reflected onto a rotatable reflective diffraction grating. The spectrally dispersed light was collected and focused by a second spherical mirror onto the exit slit, directly in front of the single-channel detector. Spectral curves were recorded by rotating the motorized grating.

In order to trace the influence of optical interband excitation on the temperature of the crystal lattice, the triplet of acceptor-bound exciton lines $(A^0,X)_J$ was investigated. The spectrum of bound and free excitons in a very pure $p$-type GaAs sample is shown in Fig. 3.1. The energetic splitting of the $(A^0,X)$ lines originates from the $JJ$-coupling between the hole on the acceptor and the exciton. Since the spin of optically active excitons is fixed to 1, the $JJ$ coupled total spin of the observed transitions depends on the spin of the remaining hole only. Consequently, the observed lines can be associated with a total spin of $1/2$, $3/2$ and $5/2$, respectively.

Due to the strong spin orbit coupling of valence band states, the spin of acceptor bound holes is thermally coupled to the crystal lattice. An exciton, which is bound to an acceptor, has no temperature dependence since its center of mass is at rest. Consequently, the occupation probabilities of the spin states associated with the triplet lines are expected to follow a Boltzmann distribution, corresponding to the lattice temperature. In principle, it should be possible to obtain the lattice temperature directly from the spectral weights of the $(A^0,X)_J$ lines.

Unfortunately, absolute temperatures cannot be obtained this way, because of the following limitations. On the theoretical side, the degeneracies and oscillator strengths of the $(A^0,X)_J$ transitions are not known. From [SM81] one obtains relative transition probabilities of 1:4:1 for the $1/2$, $3/2$ and $5/2$ lines, respectively. However, these ratios cannot account for the temperature dependence of the observed intensity ratios. On the experimental side, extraction of the $(A^0,X)$ spectral weights is complicated by the nearby $(D^+,X)$ transition. To some extent, this problem can be avoided by

investigating $p$-type material, where the ($A^0$,X) lines are stronger than the ($D^+$,X). Despite these limitations, the ($A^0$,X) triplet is a sensitive probe for changes of the lattice temperature on a relative scale.

Optical lattice heating depends critically on the excitation intensity. In order to establish an upper limit for lattice heating in MOKE studies, the intensity was set to $10^4\,\mathrm{W\,cm^{-2}}$, which is a typical probe intensity. However, it must be noted that the excitation wavelength probably also influences the heating of the lattice, which has not yet been investigated. The heating effect on the lattice is expected to increase with the photon excess energy. In the present photoluminescence experiment the excitation wavelength was $786\,\mathrm{nm}$, which was frequently used for optical spin pumping in GaAs. Therefore, the chosen configuration represents a "worst case" scenario, which is assumed to yield larger lattice heating than optical excitation in MOKE experiments.

The left panel of figure 3.4 shows the temperature dependence of the intensity ratio of $(A^0,X)_{5/2}$ to $(A^0,X)_{3/2}$ in the range of $1.6\,\mathrm{K}$ to $2.1\,\mathrm{K}$. Temperature changes of $\approx 0.2\,\mathrm{K}$ can be clearly resolved under these conditions. The intensities $I((A^0,X)_J)$ were obtained from the measured spectra by a multi-Gaussian fitting procedure. However, no absolute temperatures should be inferred from these data, because of the optically induced heating. This effect is directly visible in the right panel of figure 3.4, which shows the lateral dependence of the $(A^0,X)_{5/2}$ to $(A^0,X)_{3/2}$ ratio. At a bath temperature of $2\,\mathrm{K}$, the $(A^0,X)_{5/2}$ line gains spectral weight with increasing distance and saturates for $x \gtrsim 25\,\mu\mathrm{m}$. This indicates that the lattice is overheated in the vicinity of the excitation spot. However, the observed thermal gradient reduces with increasing bath temperature and vanishes almost for $T = 8\,\mathrm{K}$. This effect is ascribed to the increased thermal conductivity of the lattice at higher temperatures. Therefore, optically induced lattice heating can be neglected for temperatures above $8\,\mathrm{K}$, even at high excitation intensities.

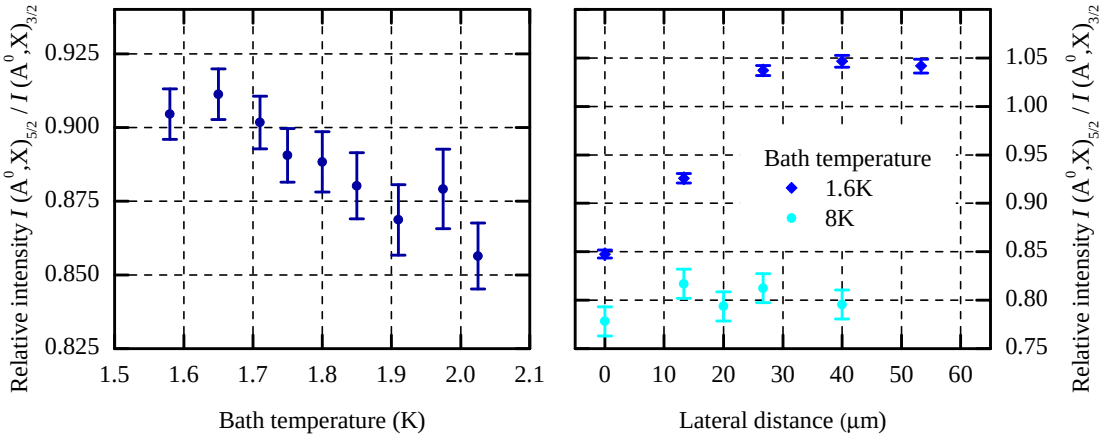


Figure 3.4: Intensity ratio of the acceptor bound exciton lines $I((A^0,X)_{5/2})/I((A^0,X)_{3/2})$ for sample G. **(left)** Bath temperature dependence. **(right)** Lateral dependence for local excitation.

## 3.3 Multi-channel imaging photoluminescence spectroscopy

This section presents a spatially resolved photoluminescence experimental setup based on a multi-channel imaging detector. The setup provides spectral and lateral information in a single shot, which reduces measurement times significantly, as compared to the concept described in section 3.2. This setup was used for the determination of lateral electron-temperature gradients, which is shown in section 3.4.

A diode-pumped solid-state laser (COHERENT CUBE) with continuous-wave emission at 786 nm wavelength served as a light source. In order to ensure sufficient beam quality for strong focusing, the laser beam was filtered and expanded by a lens-pinhole-lens setup as explained for example in [Qua07]. A shortpass interference filter (THORLABS FEL800, cut-off wavelength at 800 nm), was placed directly at the laser aperture, in order to suppress non-coherent low-energy luminescence from the laser. The filtered laser beam was guided over two alignment mirrors onto the central beam splitter, which was used to align the excitation and detection optical axes.

Figure 3.5 shows a schematic drawing of the experimental setup, starting with the central beam splitter. The reflected part of the laser beam was focused by an infinity-corrected apochromatic microscope objective (MITUTOYO M PLAN APO NIR 5X, $NA = 0.14$, $f = 40\,\mathrm{mm}$) onto the sample surface. The sample was mounted in an optical bath cryostat and immersed in liquid helium. The luminescence from the sample was collected by the objective and passed through the central beam splitter. A set of three plano-convex lenses focused the light onto the input slit of an optical grating monochromator (JOBIN YVON THR1000). The lenses were used to align the optical axis onto the monochromator, and to ensure the correct image scale and divergence angle for the given monochromator.

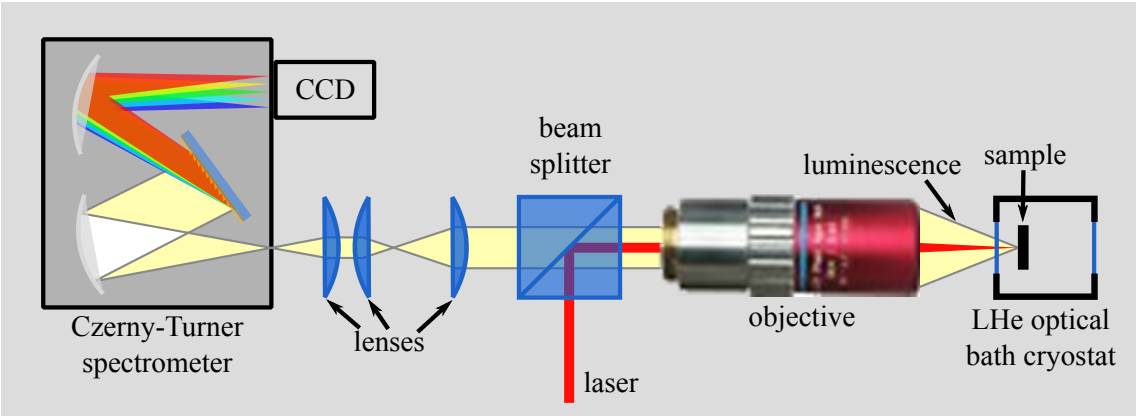


Figure 3.5: Schematic drawing of the imaging photoluminescence experimental setup. The laser beam (red line) enters the central beam splitter and is focused onto the sample surface by a microscope objective. The luminescence is collected by the objective and focused onto the entrance slit of a Czerny-Turner grating monochromator. An image of the sample surface is formed at the entrance slit. The lateral intensity profile along the slit is preserved while the light propagates through the monochromator. In the other direction, the light is dispersed by the grating and therefore projects the spectral information onto the detector.

The spectrometer was based on a Czerny-Tuner-type grating monochromator. The rotatable diffraction grating was blazed for $8000\,\text{Å}$ and had a line density of $1200\,\text{mm}^{-1}$. Light entering the input slit was collimated by a spherical mirror and directed onto the grating. A second spherical mirror collected the first order diffracted light and focused it onto the detector. A liquid-nitrogen cooled charge-coupled-device (CCD) array with 1752x532 elements (PRINCETON INSTRUMENTS) served as the multi-channel detector.

The line image of the entrance slit was dispersed by the grating in horizontal direction while the spatial resolution was preserved in vertical direction. Therefore, the image formed on the CCD contained spectral information in the horizontal direction and reflected the intensity pattern of the image at the entrance slit in the vertical direction.

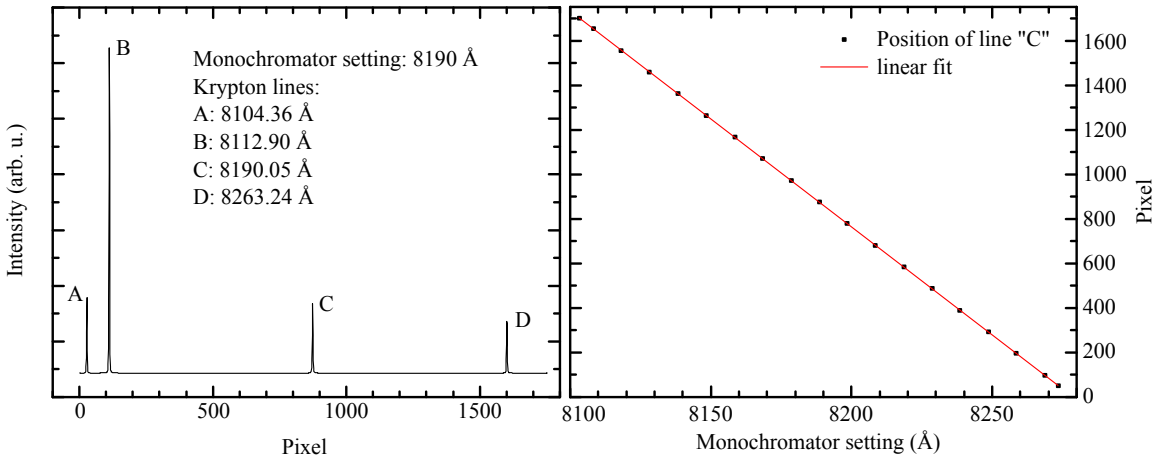


Figure 3.6: CCD calibration - spectral direction. **(left)** Line spectrum of a standard krypton discharge lamp at a nominal monochromator setting of $8190\,\text{Å}$. **(right)** Pixel position of line "C" vs. nominal monochromator setting.

**Spectral Calibration** In order to translate the column index of the CCD array to a wavelength or energy value, two things must be known. First, the pixel position of the nominal wavelength, which depends on the grating angle, and secondly, the dispersion along the CCD chip. Both quantities were found with the help of a krypton discharge lamp, which emited a large number of well-known and very narrow spectral lines [Kau93]. The left panel of figure 3.6 shows a horizontal cut through the CCD image under illumination with such a lamp. The right panel of the figure shows the trajectory of one of the krypton lines upon turning the grating. The dispersion along the horizontal direction of the CCD was determined by a linear fit of these data as $0.1026\,\text{Å}/\text{pixel}$, which yields a *digital* resolution of $\approx 20\,\mu\text{eV}$. The actual spectral resolution was determined from the width of the krypton lines to $\approx 0.1\,\text{meV}$ at $8200\,\text{Å}$.

**Spatial Calibration** Due to the design of the monochromator, the image along the entrance slit is mapped one-to-one onto the columns of the CCD array. Therefore, the magnification and the field of view are determined by the objective and the lenses in front of the monochromator, as well as the size

of the CCD array.

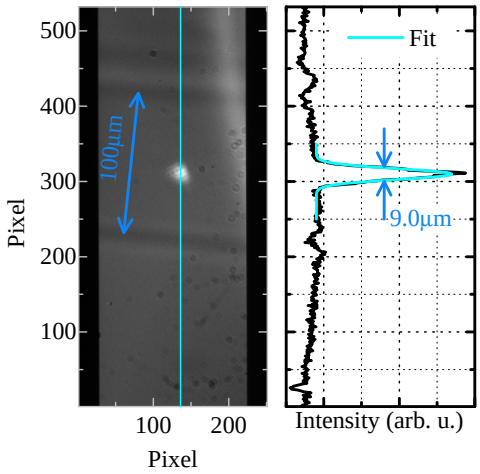


Figure 3.7: Illustration of the lateral calibration of the imaging PL setup. **(left)** Image recorded by the CCD with the monochromator set to zeroth order. The black borders originate from the widely open entrance slit. A sample with a well defined $100\,\mu\mathrm{m}$ GaAs stripe was used as a reference structure. From this image, a calibration factor of $1.86\,\mathrm{pixel}/\mu\mathrm{m}$ was obtained. The bright spot in the middle comes from the focused excitation laser. **(right)** Intensity profile along the vertical line through the laser spot. From the Gaussian fit of the laser profile, the optical resolution was derived as $4.5\,\mu\mathrm{m}$ half width at half maximum.

The spatial calibration was performed with the help of a lithographically structured sample. Figure 3.7 shows an image of a $100\,\mu\mathrm{m}$ wide GaAs stripe and the excitation laser spot in the center of it. The image was recorded with the monochromator set to zeroth order, i.e. the grating acted like a normal plane mirror. In this configuration, the spatial information was conserved in both directions. From the width of the GaAs stripe in the image, a calibration factor of $1.86\,\mathrm{pixel}/\mu\mathrm{m}$ was deduced. A vertical cut through the laser spot is shown in the right half of the figure. A Gaussian fit of this intensity profile yielded an optical resolution of $4.5\,\mu\mathrm{m}$ (half width at half maximum).

The raw data produced by the imaging PL setup unfortunately revealed some unwanted features, which made a direct analysis unfavorable. First, sharp spikes of usually only single pixels were visible in the data, which originated presumably from cosmic radiation or similar. Secondly, a small non-correctable misalignment of the diffraction grating caused a static distortion of the spatio-spectral image. Thirdly, etalon interference effects at the CCD itself produced an oscillating modulation along the spectral direction.[2] These issues were tackled by a sophisticated preprocessing procedure, implemented in MATLAB, which is discussed in the following paragraphs. Figure 3.8 illustrates the effect and quality of this procedure by comparing a typical raw data map with an intermediate state of correction and the final image.

**Spike detection and elimination** In order to identify individual pixels, whose intensity values were likely to be outliers, the deviation of each pixel from the mean value of a certain number of surrounding pixels was compared to the standard deviation of that neighborhood. If the deviation exceeded a predefined threshold, the value of the questionable pixel was set to the average value of the surrounding pixels.

[2] This is a well known effect in thinned, back-illuminated CCD sensors. According to data provided by the manufacturer, an oscillation period of $\approx 5\,\mathrm{nm}$ could be expected. However, the observed periodicity was in the range of $\approx 0.2\,\mathrm{nm}$ to $0.4\,\mathrm{nm}$, which suggests that a significantly thicker etalon must have been involved. A likely candidate is the cover glass of the CCD.

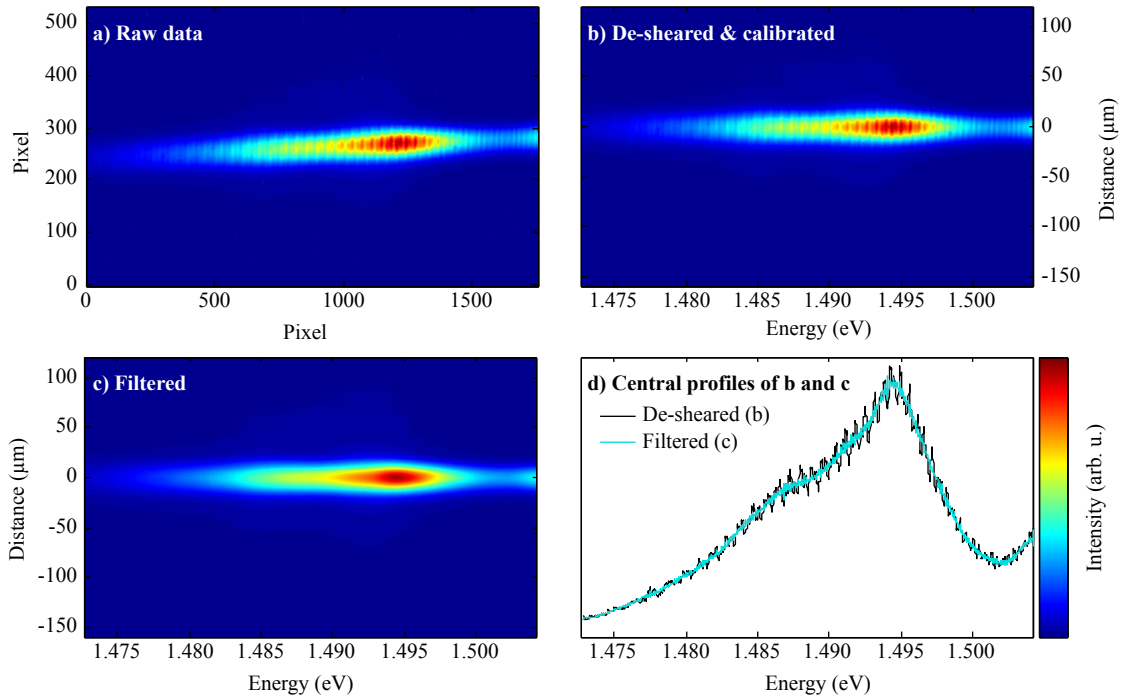


Figure 3.8: **(a)** Raw image recorded by the CCD for sample C with the grating set to 8330 Å. **(b)** Calibrated data corrected by spike-removal and de-shearing. **(c)** Calibrated data filtered by a dual-Gaussian band-reject function. **(d)** Spectral profiles at zero distance obtained from the filtered and unfiltered image (c and b).

**Compensating spatio-spectral image distortions** The distortion of the raw image originated from a small misalignment of the grating lines, with respect to the vertical axis of the focusing mirrors. This added a vertical angle component to the spectral dispersion, which manifested as a wavelength-dependent vertical shift of the slit image. Note that due to this effect, the image was not rotated but sheared. This could be seen by illuminating the entrance slit with a krypton-vapor lamp. When the slit was also reduced in vertical direction, the spectral lines appeared not only dispersed horizontally, but also slightly vertically. The vertical shift depended on the horizontal position on the CCD only, and could therefore be corrected by a shearing operation. The amount of the shearing was determined from the line-spectrum images of the krypton lamp. Sub-pixel vertical shifts were achieved by a Fourier-transform linear-phase method.

**Interference-modulation removal** The recorded raw images show strong intensity oscillations along the wavelength axis. The amplitude of these oscillations is proportional to the recorded signal, i.e. it is strongest where the signal was high. This suggests that the effect was indeed caused by etalon interference at parallel reflecting surfaces, rather than by stray light or something. A Fourier analysis revealed two distinct frequency components, one at 42/1752 per pixel and another at 90/1752 per pixel, which correspond to spectral oscillation periods of approximately 4.3 Å and 2.0 Å, respectively. In order to remove this modulation without disturbing the shape of the luminescence spectrum, a carefully adjusted dual-peak band-reject filter was applied to each row of the CCD image separately.

Panel (d) of figure 3.8 shows a spectral profile at zero vertical distance before and after the application of this filter.

Note that this correction procedure was designed and optimized for the line shape fitting of the (e,$A^0$) band, which is presented in the following section. It is unsuited by design for applications involving sharp spectral lines, like the investigation of the ($A^0$,X) triplet presented in the previous section.

## 3.4 Lateral electron temperature determination by spatio-spectral PL imaging

Electron temperatures were extracted from photoluminescence measurements of the conduction-band-to-acceptor transition (e,$A^0$). From the high energy flank of the corresponding luminescence band, the electron temperature was determined using the line shape model of equation 2.14. With the help of the experimental setup described in chapter 3.3, the (e,$A^0$) spectrum was measured as a function

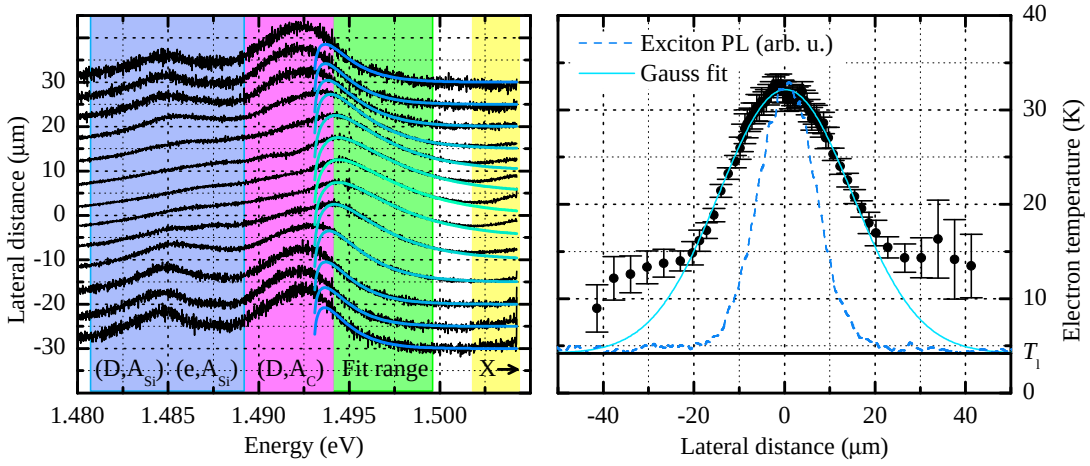


Figure 3.9: **(left)** Photoluminescence spectra of sample C for various distances from the excitation laser spot. The PL-intensity curves (black) are normalized and the vertical shift indicates the lateral distance. The blue-green curves represent best fits of the electron–acceptor line shape (equation 2.14) to the high-energy flank. The shown spectral range covers the electron–acceptor and donor–acceptor transition bands for the silicon and carbon acceptors at around 1.485 eV and 1.492 eV, respectively. Note that the spectral weight shifts from the (e,$A^0$) to the ($D^0$,$A^0$) transitions with increasing distance for both acceptor species. The green shaded area marks the range that was used for the least-squares fitting routine. The other colored areas roughly mark other transition bands as labeled. **(right)** Electron temperature (black dots) as obtained from the (e,$A^0$) line shape fits. The data is well described by a Gaussian up to approximately 20 µm, where the (e,$A^0$) gives way to the ($D^0$,$A^0$), which interferes with the line shape analysis. The blue dashed line shows the exciton luminescence intensity for reference.

of the lateral distance from the excitation source. Typical spectra are shown in figure 3.9 for sample C, together with the corresponding line shape fits. Since the sample is notably $n$-doped, the spectra clearly reveal contributions from donor–acceptor-pair transition ($D^0$,$A^0$). Unfortunately, this band overlaps with the (e,$A^0$) range, which complicates the determination of the electron temperature from the latter. Care must be taken to make sure that only the undisturbed part of the (e,$A^0$) high energy flank is used for data analysis. In figure 3.9 the colored areas roughly highlight the spectral ranges of the (e,$A^0$) line shape fit (green) as well as the neighboring bands (blue, red and yellow).

The spectra in figure 3.9 show that the influence of the ($D^0$,$A^0$) band is relatively small at the point of excitation ($0\,\mu m$) and increases with increasing distance. This effect is also visible in the lateral dependence of the electron temperature (right panel of figure 3.9). Here, a sharp bend appears at approximately $20\,\mu m$ distance. Most probably, this is the point from where on the (e,$A^0$) flank no longer dominates the fitted part of the spectrum. Within this $20\,\mu m$ boundary the electron temperature is well described by a Gaussian. The Gaussian fit was performed with a fixed "background" temperature of $4.2\,K$, which corresponds to the bath temperature during the measurement.

For comparison, the right panel of figure 3.9 also shows the intensity profile of the exciton luminescence. The width of this profile reflects the optical resolution of the experiment. Note that the exciton PL is much smaller than the electron-temperature profile. This is indicates the presence of heat diffusion within the conduction band.

The Gaussian fit to the lateral electron-temperature data was chosen as a phenomenological basis for the description of spin diffusion in the presence of hot electrons (chapter 4). A mathematical approach for the description of conduction-electron heat diffusion is presented in section 3.6. Unfortunately, the envisioned model yields a rather complicated formalism itself. Therefore both models (spin diffusion and heat diffusion) have not been successfully combined yet.

## 3.5 Temperature dependence of electron overheating

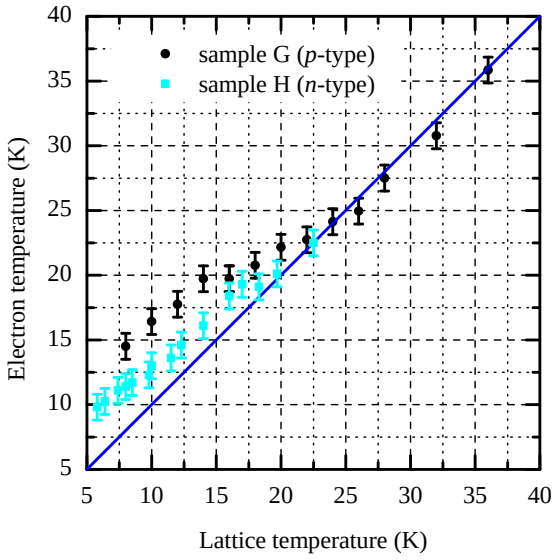


Figure 3.10: Electron temperature for samples G and H determined by (e,$A^0$) line shape fits of non-spatially resolved spectra as function of the lattice temperature. Note that the overheating vanishes for temperatures larger than $\approx$ 25 K in accordance with the energy relaxation rates in figure 2.6. The diagonal line indicates the equality of electron and lattice temperature.

The temperature dependence of the electron overheating was investigated for samples G and H, i.e. rather pure GaAs crystals with very low residual charge-carrier concentrations. For this purpose, spectra of the (e,$A^0$) transition were recorded in a non-spatially resolved configuration. The electron temperature was obtained from fitting equation 2.14 to these data. The results are summarized in figure 3.10.

Although the excitation power was very low ($10\,\mathrm{W\,cm^{-2}}$), electron overheating ($T_e > T_l$) is noticeable at low lattice temperatures for both samples, $p$-type and $n$-type. The $p$-type sample exhibits slightly stronger overheating than the $n$-type sample because the optical excess energy is distributed among fewer electrons. Therefore, the average energy per electron increases until the dissipation rate can compensate the heating.

For both samples, the electron overheating persists up to lattice temperatures of $\approx 20\,\mathrm{K}$ to $25\,\mathrm{K}$, which is consistent with the theoretical picture of electron energy dissipation presented in chapter 2.4. For lateral spin and electron diffusion, it is important to realize the consequence of this transition from the overheated regime ($< 20\,\mathrm{K}$) to the thermalized regime ($> 25\,\mathrm{K}$). First, when electrons are hotter than the nominal lattice temperature, diffusion takes place at a higher rate than expected. Secondly, at low lattice temperatures a lateral electron temperature gradient is established, which leads to a lateral variation of the diffusivity. This issue is discussed in chapter 4.4.

## 3.6 Conduction-electron heat diffusion

In the present section a mathematical model for the lateral diffusion of optically induced electron overheating is discussed. The basic idea is to combine a standard diffusion picture with the electron energy relaxation rate discussed in chapter 2.4. On the first glance, the resulting equation is very similar to the spin diffusion equation presented in chapter 2.6. However, the electron energy relaxation also depends strongly on the electron temperature, which adds an intrinsic feedback to the model.

The steady-state lateral profile of the electron temperature $T_e$ is assumed to follow the equation

$$\nabla(K(T_e)\nabla T_e) + a(T_e) = g \tag{3.1}$$

where $K$ is the diffusion coefficient, $a$ is the dissipation term and $g$ represents the heat source. For a $\mathrm{TEM}_{00}$ excitation laser spot with a $1/e$ half width $w_g$ and an absorption depth $z_g$ the generation term can be written in cylindrical coordinates as

$$g(r,z) = g_0\,(\pi w_g^2 z_g)^{-1} \exp\left[-\left(\frac{r}{w_g}\right)^2 - \left(\frac{z}{z_g}\right)\right] \tag{3.2}$$

The factor

$$g_0 = \frac{(1-R)P_{\mathrm{Laser}}}{E_{\mathrm{Laser}}} E_{\mathrm{heat}} \tag{3.3}$$

is given in terms of the laser power $P_{\mathrm{Laser}}$, the photon energy $E_{\mathrm{Laser}}$, the sample reflectance $R$ and the effective heat per photoexcited electron $E_{\mathrm{heat}}$. It represents the peak heating power in the center of the excitation spot.

Assuming Maxwell-Boltzmann distributed electrons under steady-state conditions, the dissipation term in equation 3.1 can be expressed in terms of the energy loss rates discussed in chapter 2.4 and reads

$$a(T_e) = n(r,z)\left(\Gamma_{\text{po}} + \Gamma_{\text{pe}} + \Gamma_{\text{ac}}\right) \tag{3.4}$$

Here, $n(r,z)$ is the local density of conduction-band electrons and the remaining terms are the average energy loss rates per electron due to polar-optical (po), piezoelectric (pe) and acoustic deformation potential (ac) scattering. The local rate of energy dissipation depends on the local electron density $n(r,z)$ which is approximated by a Gaussian of the form

$$n(r,z) = \frac{2(1-R)}{(\pi^{3/2}w_n^3)}\tau\frac{P_{\text{Laser}}}{E_{\text{Laser}}}\exp\left[-\frac{r^2+z^2}{w_n^2}\right] + n_{\text{int}} \tag{3.5}$$

where $n_{\text{int}}$ is the intrinsic electron density. The factor in front of the exponential describes the peak electron density under the given excitation conditions, where $\tau$ is the radiative lifetime and $w_n$ represents the photoelectron diffusion length.

The thermal diffusivity $K(T_e)$ in equation 3.1 describes the heat conduction of the electron system. Low-temperature heat conductivity of GaAs is almost entirely due to phonons and no data exist on the contribution of charge carriers. Therefore, the thermal diffusivity is approximated in the ideal gas picture as

$$K(T_e) = \frac{1}{3}\langle v\rangle\, l c_e n(r,z) \tag{3.6}$$

where $\langle v\rangle = \sqrt{\frac{3k_BT_e}{m_e}}$ is the average electron velocity, assuming a Maxwell-Boltzmann distribution. The mean free path $l = (\sigma n(r,z))^{-1}$ is given in terms of the scattering cross section, which in turn is approximated with the help of the quasi-particle de Broglie wavelength $\lambda_e = h/\sqrt{2\pi m_e k_B T_e}$ as $\sigma = \pi\lambda_e^2$. The heat capacity per electron is $c_e = \frac{3}{2}k_B$ in the ideal gas model.

This model does not account for the very fast processes during thermalization of newly excited electrons. These are the rapid initial relaxation through emission of LO-phonons as long as the electron energy is larger than $E_{\text{LO},\Gamma}$, as well as fast diffusion of very hot electrons. Due to the initial emission of LO-phonons, the effective heat that each photoexcited electron contributes to the conduction-band population is less than the excitation excess energy (see equation 2.8). The diffusion of not-yet-thermalized electrons distributes the excess heat over a larger volume as the pure excitation volume. Therefore, the relevant length scale for the heat source $g$ is in fact the photoelectron diffusion length $w_n$ instead of the excitation source width $w_g$.

Equation 3.1 was evaluated numerically using the finite element method. The left panel of figure 3.11 shows an illustration of a simulated sample volume. The right panel of the figure compares the model to experimental data of samples G and H. The experimental data shown in the figure were obtained with the experimental setup described in chapter 3.2.

Although there are no actual free parameters in this model, the effective heat per photoexcited electron $E_{\text{heat}}$ and the electron diffusion length $w_n$ are not directly accessible. Both quantities were

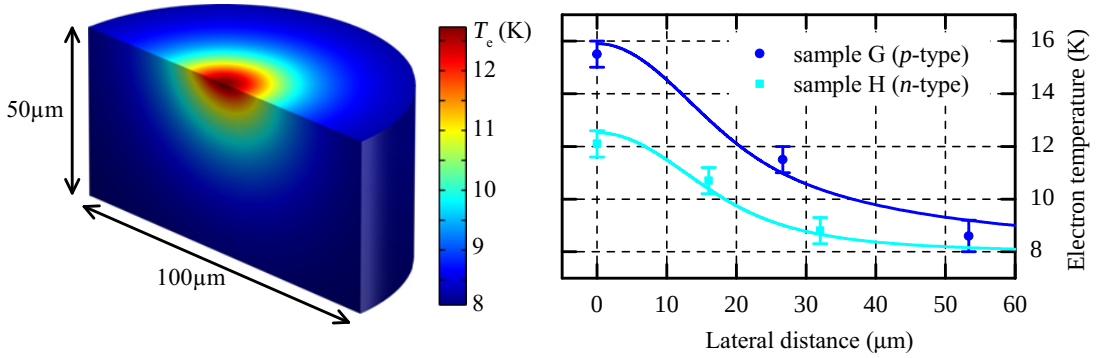


Figure 3.11: Electron heat diffusion in GaAs. **(left)** Pseudo-3D illustration of the lateral electron temperature gradients under local optical interband excitation. The picture shows a cut through a cylindrical model volume with the electron temperature coded in color. **(right)** Measured data and model calculations in comparison. The data points were measured with the setup described in section 3.2. The excitation spot size was $4\,\mu\mathrm{m}$. The solid lines represent radial surface profiles from the 3D model calculation. For sample H the model profile corresponds directly to the data shown in the left panel of the figure.

therefore adjusted for optimal agreement between experiment and model. The best fitting values were found to be within the boundaries of expectation, as discussed below. All final model parameters, that were used to generate the curves in figure 3.11, are summarized in table 3.1 as far as they are not already included in table C.1.

The effective heating is the result of the competition between $ee$-scattering and electron–phonon scattering during the rapid initial relaxation as discussed in chapter 2.4. Due to the very low electron density of the material, the best-fitting value for $E_{\mathrm{heat}}$ was found very close to the theoretical minimum described in chapter 2.4.

The photoelectron diffusion length was found to be $w_n = 13\,\mu\mathrm{m}$, which is approximately three times larger than the excitation laser spot. This value is consistent with low-temperature electron mobilities in very pure GaAs as found in the literature [Wil75].

## 3.7 Conclusion

It was shown in section 3.2 that the crystal lattice is overheated at very low temperatures of around $2\,\mathrm{K}$ on length scales of several tens of micrometers. At a slightly higher temperature of $8\,\mathrm{K}$, this thermal gradient vanishes mostly and the lattice remains in thermal equilibrium with the heat bath. Since the spin imaging experiments in the remainder of this work were performed mostly above $\approx 8\,\mathrm{K}$, lattice heating is not taken into account any further.

In contrast, local electron heating is cannot be avoided for temperatures below $\approx 25\,\mathrm{K}$, due to the limited thermal coupling between electrons and lattice. It was shown in section 3.4 that the electron temperature is significantly higher than the lattice temperature over length scales of several tens of

Table 3.1: Model parameters

| Scope | Parameter | Value |
|---|---|---|
| general | $E_{\text{Laser}}$ | $1.579\,\text{eV}$ |
| | $w_n$ | $13\,\mu\text{m}$ |
| | $z_g$ | $0.7\,\mu\text{m}$ |
| | $R$ | $0.3$ |
| | $\tau$ | $7\,\text{ns}$ |
| | $E_{\text{heat}}$ | $18\,\text{meV}$ |
| sample G | $P_{\text{Laser}}$ | $0.8\,\mu\text{W}$ |
| | $n_{\text{int}}$ | $7 \times 10^{12}\,\text{cm}^{-3}$ |
| sample H | $P_{\text{Laser}}$ | $1.6\,\mu\text{W}$ |
| | $n_{\text{int}}$ | $5 \times 10^{11}\,\text{cm}^{-3}$ |

micrometers, even at low excitation densities.

Furthermore, it was shown in section 3.4 that the lateral electron temperature profile in $n$-doped GaAs is well approximated by a Gaussian. In chapter 4, a spin diffusion model is proposed, that makes use of this empiric approximation in order to take the lateral electron temperature gradient into account.

# 4 Magneto-optical spin imaging in $n$-GaAs at the MIT

The goal of this chapter is to draw a coherent picture of conduction-electron spin dynamics in $n$-GaAs at the metal-to-insulator transition, and to point out the role of photogenerated hot electrons. The study was conducted for the doping-series samples A to F. First, an experimental setup is presented, which allows all-optical spin studies with micrometer spatial resolution at cryogenic temperatures. In order to gain an insight into the optical probing technique, the optically induced exciton Kerr effect is discussed. Next, the temperature and doping dependence of the spin relaxation time is investigated. These data are required for the following evaluation of lateral spin diffusion, and - as a coherent set - contribute to the picture of spin relaxation at the MIT. Subsequently, the influence of hot electrons on optical spin studies in GaAs is illustrated on the basis of the diffusion model from chapter 2.6. Finally, an empirically modified version of the spin diffusion model is presented, which shows efficient compensation of the hot-electron influence. Therefore, undisturbed extraction of the spin diffusion coefficient was facilitated by this model for the first time in the investigated temperature range.

## 4.1 Experimental methods and techniques

The experimental basis for spatially resolved spin imaging and Hanle-MOKE studies was the two-color pump-probe technique, which was first presented in [KSSA97]. Optical spin pumping was performed by a circularly polarized laser, while the nonequilibrium spin polarization was probed by a second laser via the magneto-optic Kerr effect. Spatial resolution was realized by focusing both lasers to small spots, and scanning the probe spot with respect to the pump spot over the sample surface. A magnetic field for Hanle-MOKE studies was provided by an electro-magnet installed in Voigt-geometry [MZ84].

### 4.1.1 Experimental setup

Figure 4.1 shows a schematic drawing of the experimental setup. The sample was located inside a liquid-helium cooled continuous-flow cold-finger cryostat (OXFORD INSTRUMENTS MICROSTAT HE) with special narrow rectangular tail and optical access windows. Strain-free sample mounting was achieved by clamping the sample on a copper plate with good thermal contact to the cold finger of the cryostat. A thin-film resistance cryogenic temperature sensor (LAKE SHORE CRYOTRONICS CERNOX CX-SD) was clamped to the back side of the copper plate in order to monitor the temperature as close to the sample as possible. A proportional–integral–derivative (PID) controller was used to actively stabilize the temperature by adjusting the current of a heating wire, located at the heat exchanger of the cryostat. The input signal for the PID-controller came from a second temperature sensor located at the heat exchanger, which was sufficiently accurate for stabilization, but too far away from the sample to monitor the sample temperature correctly at very low temperatures. Sample temperatures between $\approx 8\,\mathrm{K}$ and $300\,\mathrm{K}$ could be achieved and stabilized to better than $\pm 0.05\,\mathrm{K}$. The

lowest achievable temperature varied slightly on a daily basis, probably due variations of the isolation vacuum. The difference between the internal temperature sensor and the sample sensor varied between 3 K and 6 K at maximum cooling. The cryostat was mounted on a 3-axis manual translation stage for precise sample positioning.

Two independently tunable Ti:sapphire continuous-wave lasers were used for optical spin orientation (pumping) and magneto-optic Kerr measurements (probing). They were driven by two diode-pumped solid-state (DPSS) lasers (COHERENT VERDI V10 and V12). Both Ti:sapphire lasers produced a maximum output power of approximately 1 W. The light was attenuated by motorized reflective variable neutral-density filters. The optical powers $P_{\mathrm{pump}}$ and $P_{\mathrm{probe}}$ at the sample were monitored by calibrated Si-photodiodes.

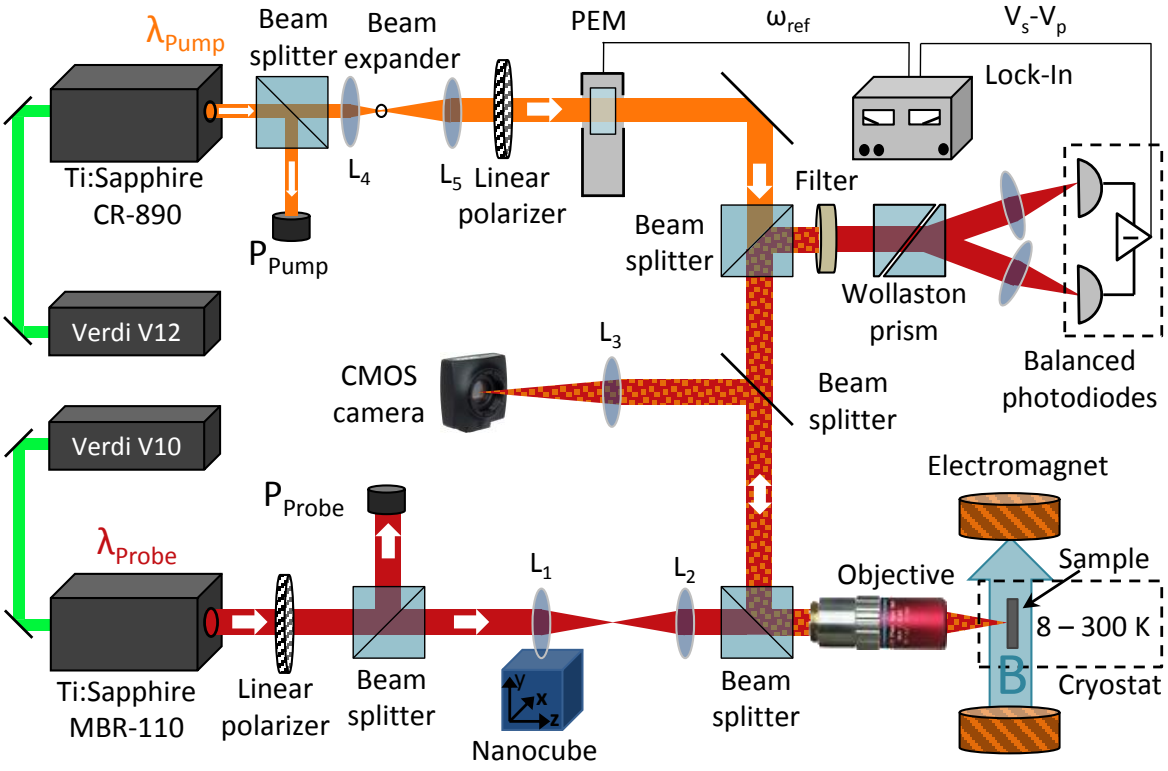


Figure 4.1: Experimental Setup for scanning Kerr microscopy. Two tunable Ti:sapphire lasers served as light sources for optical spin orientation and magneto-optical probing. Both laser beams were focused on the sample surface by a microscope objective. The probe beam passed two aspheric lenses in front of the objective to facilitate lateral scanning. The reflected probe beam was collimated by the objective and the Kerr rotation was measured by a pair of balanced photodiodes. The pump beam was modulated between left- and right-handed circular polarizations by a photoelastic modulator (PEM). Therefore, the desired Kerr rotation signal was modulated with the same frequency (see section 4.1.3). The signal was finally demodulated by a Lock-in amplifier. A complementary metal-oxide semiconductor (CMOS) camera was used to record microscope images of the sample surface and the laser spots.

Optical spin orientation was performed by the *pump laser* (COHERENT CR890), the output wavelength ($\lambda_{\mathrm{pump}}$) of which could be tuned between $770\,\mathrm{nm}$ and $840\,\mathrm{nm}$. In order to improve the spatial resolution, the beam of the CR890 was expanded by the lens-pair $\mathrm{L_4/L_5}$ (focal lengths $f_4 = 40\,\mathrm{mm}$ and $f_5 = 60\,\mathrm{mm}$) and filtered by a $75\,\mu\mathrm{m}$ pinhole located in the fourier plane of the two lenses. The polarization of the pump beam was prepared by a Glan-Taylor linear polarizer (extinction ratio $10^5$:1), followed by a photoelastic modulator (PEM, HINDS INSTRUMENTS PEM-100). The fast axis of the PEM was oriented under $45°$ with respect to the transmission axis of the polarizer, and the phase retardation of the PEM was set to $\lambda/4$ in order to obtain modulated circular polarization [Kem69]. The details of the modulation scheme are discussed in section 4.1.3.

The optically induced spin polarization was measured through the magneto-optic Kerr effect, which was introduced to the beam of the *probe laser* (COHERENT MBR-110E) upon reflection from the sample. The probe wavelength $\lambda_{\mathrm{probe}}$ was tunable from $750\,\mathrm{nm}$ to $900\,\mathrm{nm}$. The polarization of the probe laser was prepared by a Glan-Taylor linear polarizer (extinction ratio $10^5$:1) in vertical direction. In this configuration, the polarization was perpendicular to the plane of incidence at the reflecting elements in the beam path, i.e. $s$-polarized. The pure $s$-polarization eliminated artifacts due to polarization sensitive reflectivity of the optical components (mirrors, beam splitters, etc.).

As discussed in chapter 2.9, the magneto-optic Kerr effect introduces a rotation of the polarization axis and an ellipticity upon reflection from the sample surface. For the measurement of the Kerr rotation, the reflected probe beam passed through a Soleil-Babinet compensator (SBC) and a Wollaston prism (WP) onto a pair of balanced photodiodes. The SBC was set to a fixed phase retardation of $\lambda/2$ and an angle of $22.5°$ with respect to the nominal incident linear polarization. In this configuration, the SBC rotated the frame of reference for the polarization by $45°$. The Wollaston prism split the beam into two orthogonal linear polarization components, each of which was detected by one of the balanced photodiodes. The signal produced by the difference amplifier was then directly proportional to the Kerr rotation angle. It was demodulated by a lock-in amplifier (STANFORD RESEARCH SR530) with the PEM frequency as reference. An $800\,\mathrm{nm}$ long-pass filter (THORLABS FES0800) in front of the balanced detector suppressed residual pump light.

### 4.1.2 Lateral scanning scheme and optical resolution

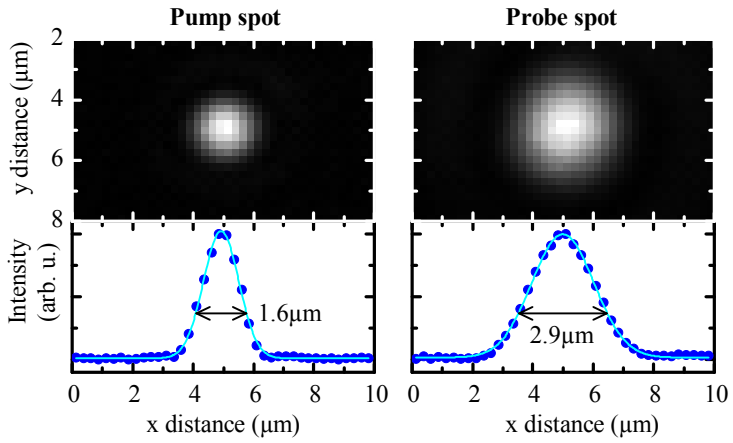


Figure 4.2: Microscope images of the pump and probe spots on the sample surface recorded with a CMOS camera. The lower panels show cuts through the center of each spot (dots) and least-squares fitted Gaussians (lines). The arrows indicate the $1/e$ full width.

Lateral resolution was realized by focusing both laser beams with a microscope objective (MITUTOYO M PLAN APO NIR 50X, NA $= 0.42$, $f_{\mathrm{O}} = 4\,\mathrm{mm}$) under normal incidence onto the sample surface. The probe spot was scanned with respect to the pump spot by a pair of aspheric lenses ($\mathrm{L}_1$ and $\mathrm{L}_2$ with $f_1 = f_2 = 4\,\mathrm{mm}$), which were placed in the probe beam path in front of the objective. Lens $\mathrm{L}_1$ was mounted on a 3-axis piezo translation stage (PHYSIK INSTRUMENTE NANOCUBE P-611.3) for sub-micrometer positioning, while lens $\mathrm{L}_2$ was fixed at a distance of $2f = 8\,\mathrm{mm}$ from $\mathrm{L}_1$. The intermediate image in the Fourier plane between the two lenses was mapped directly onto the sample surface. Therefore, a lateral translation of $\mathrm{L}_1$ resulted in an equal shift of the probe spot on the sample surface. The accessible field of view (FOV) was determined by the travel range of the piezo stage ($100\,\mu\mathrm{m} \times 100\,\mu\mathrm{m}$). The pump beam entered the microscope objective without passing through $\mathrm{L}_1$ and $\mathrm{L}_2$, and the pump spot was therefore stationary while the probe spot was scanned.

This scanning scheme was an innovative improvement of older designs, which employed two seperate microscope objectives for focusing the pump and the probe beam separately [CS05, CFL$^+$07, FSK$^+$07, QAO$^+$09]. Due to mechanical hindrances, the numerical aperture of these objectives was limited, which restricted the optical resolution to $\approx 4\,\mu\mathrm{m}$. For comparison, the setup presented above yielded an optical resolution of $1.7\,\mu\mathrm{m}$, because this restriction was eliminated by the use of only one objective. Another improvement was the introduction of a second tunable Ti:sapphire laser as a pump source, which allowed to investigate the influence of the excitation excess energy on spin dynamics.

During measurements, the focused laser spots on the sample surface were monitored by a complementary metal-oxide semiconductor (CMOS) camera (THORLABS DCC1645M). This camera was also used to determine the optical resolution of the setup. Figure 4.2 shows images of the pump and probe spots on the sample surface. The line cuts through the spots are well fit by Gaussians, which yields a $1/e$ half width of $0.80 \pm 0.10\,\mu\mathrm{m}$ for the pump spot and $1.45 \pm 0.10\,\mu\mathrm{m}$ for the probe spot, respectively. These numbers were also confirmed by the knife edge scanning method. Consequently, the net optical resolution was $1.66 \pm 0.14\,\mu\mathrm{m}$, which is the result of the convolution of both laser spots. The slightly worse focus size of the probe spot originates from distortions introduced by the aspheric lenses. The uncertainties stated above represent estimates on the basis of the manual focusing reproducibility.

### 4.1.3 Modulated Kerr-angle detection

When the pump laser polarization is modulated between left and right circular, the spin orientation of excited electrons alternates between up and down. This modulation is further imprinted on the polarization of the reflected probe laser due to the magneto-optic Kerr effect. The modulation with the working frequency of the PEM ($\omega_{\mathrm{PEM}} \approx 50\,\mathrm{kHz}$) is usually done for two reasons. First, the build up of a nuclear spin polarization by the Overhauser effect is avoided [MZ84, SPW97]. A nonzero nuclear field would interfere severely with the study of electron spin relaxation and diffusion. Secondly, lock-in technique can be used to measure very small Kerr signals with high sensitivity. The lock-in amplifier basically shifts the desired signal spectrally away from the ever present $1/f$-noise background. The present section shows how the detector output signal can be calculated in the Jones-matrix formalism.

The time dependence of the modulated Kerr rotation $\theta$ and ellipticity $\phi$ is

$$\theta\,(t) = \theta_K \sin\left(\omega_{\mathrm{PEM}} t\right) \tag{4.1}$$

$$\phi(t) = \phi_K \sin(\omega_{\text{PEM}} t) \tag{4.2}$$

In the Jones notation [Jon41], the polarization of the probe laser before the sample is

$$\boldsymbol{E}_{\text{in}} = \frac{E_{\text{in}}}{\sqrt{2}} \begin{pmatrix} 1 \\ 1 \end{pmatrix} \tag{4.3}$$

The introduction of the Kerr effect upon reflection from the sample surface can be expressed as the matrix product

$$\tilde{\boldsymbol{M}}_K(t) = \tilde{\boldsymbol{R}}(\pi/4) \cdot \tilde{\boldsymbol{R}}(\theta(t)) \cdot \tilde{\boldsymbol{\phi}} \cdot \tilde{\boldsymbol{R}}(-\pi/4) \tag{4.4}$$

where

$$\tilde{\boldsymbol{R}}(\alpha) = \begin{pmatrix} \cos(\alpha) & -\sin(\alpha) \\ \sin(\alpha) & \cos(\alpha) \end{pmatrix} \tag{4.5}$$

is the rotation matrix and

$$\tilde{\boldsymbol{\phi}} = \begin{pmatrix} \cos(\phi(t)) & 0 \\ i\sin(\phi(t)) & 0 \end{pmatrix} \tag{4.6}$$

introduces the ellipticity. The polarization of the probe beam after the reflection from the sample can then be written

$$\boldsymbol{E}_{\text{out}} = r \cdot \tilde{\boldsymbol{M}}_K(t) \cdot \boldsymbol{E}_{\text{in}} \tag{4.7}$$

where

$$r = E_{\text{out}}/E_{\text{in}} \tag{4.8}$$

is the amplitude reflection coefficient for normal incidence. Carrying out the matrix multiplications yields

$$\boldsymbol{E}_{\text{out}} = \frac{r \cdot E_{\text{in}}}{\sqrt{2}} \begin{pmatrix} e^{-i\phi(t)}\cos(\theta(t)) - e^{i\phi(t)}\sin(\theta(t)) \\ e^{i\phi(t)}\cos(\theta(t)) + e^{-i\phi(t)}\sin(\theta(t)) \end{pmatrix} \tag{4.9}$$

The two orthogonal linear polarization components $E_{x,y}$ are split by the Wollaston prism and directed to the balanced photodiodes. The measured photocurrents $I_{x,y}$ are proportional to the corresponding intensities, i.e.

$$I_{x,y} \propto \left| (\boldsymbol{E}_{\text{out}})_{x,y} \right|^2 \tag{4.10}$$

The photocurrent difference $I_x - I_y$ is transformed into a voltage signal by an electronic amplifier. The time-dependent detector output signal is proportional to the photocurrent difference and reads

$$V_{\text{det}}(t) \propto \frac{1}{2} |E_{\text{out}}|^2 \left[ \sin\big(2(\theta_K - \phi_K)\sin(\omega_{\text{PEM}} t)\big) + \sin\big(2(\theta_K + \phi_K)\sin(\omega_{\text{PEM}} t)\big) \right] \tag{4.11}$$

Using the Jacobi-Anger identity [AS65]

$$\sin(z\,\sin(x)) = 2\sum_{n=0}^{\infty} J_{2n+1}(z)\,\sin((2n+1)x) \tag{4.12}$$

expression 4.11 can be expanded in terms of odd harmonics of the PEM frequency. Here, $J_k$ denotes the Bessel function of $k$th order. The calculation yields

$$V_{\text{det}}(t) \propto |E_{\text{out}}|^2 \sum_{n=0}^{\infty} \big(J_{2n+1}(\theta_k - \phi_k) + J_{2n+1}(\theta_k + \phi_k)\big)\sin((2n+1)\,\omega_{\text{PEM}}\,t) \tag{4.13}$$

The output voltage $V_{\text{det}}(t)$ of the balanced photodetector is demodulated by a lock-in amplifier, which uses $\omega_{\text{PEM}}$ as reference. The lock-in amplifier mixes the input signal with a sinusoidal signal with frequency $\omega_{\text{PEM}}$ and applies a low-pass filter. The output voltage $V_{\text{out}}$ is then proportional to the zero order term of equation 4.13 only. Moreover, the expected Kerr rotation and ellipticity are very small, i.e. $\theta_K \ll 1$ and $\phi_K \ll 1$. In this case the first-order Bessel function can be approximated as $J_1(x) \approx \frac{x}{2}$. The obtained expression for the lock-in signal reads

$$V_{\text{out}} = g \cdot |E_{\text{out}}|^2\,\theta_K \tag{4.14}$$

Here, $g$ is a constant which depends on the internal details of the balanced photodetector and the lock-in amplifier. In order to perform absolute Kerr angle measurements, $g$ must be determined by a calibration procedure described in [Hen11]. Note that in this approximation and configuration the lock-in output signal is explicitly independent of the Kerr ellipticity.

### 4.1.4 Hanle-MOKE measurements

Hanle-MOKE measurements were performed with the experimental setup described above in two different ways. First, with defocused pump and probe spots, the spin relaxation time $\tau_s$ was measured in the classical way, i.e. without the influence of spin diffusion. Such data are presented in chapter 4.3. Secondly, with focused laser spots the *local* Hanle effect was observed. When diffusion cannot be neglected, the shape of the Hanle curve is not Lorentzian anymore. This section shows the procedure for the experimental determination of spin relaxation times with the experimental setup presented above using the Hanle effect as described in section 2.8.

For measurements of the intrinsic spin relaxation time of conduction band electrons, three things must be considered. First, the probed sample volume must well exceed the spin decay length $l_s = \sqrt{D_s\tau_s}$ in order to avoid unwanted contributions from spin diffusion. This was achieved by moving the sample slightly out of focus until the pump and probe spots were spread over $\approx 100\,\mu\text{m}$. Secondly, the presence of optically excited holes gives rise to additional spin relaxation through the BAP-mechanism (see chapter 2.7), as well as radiative recombination of spin polarized electrons with holes. These influences were eliminated by measuring the pump power dependence of the Hanle effect and extrapolating towards zero power. Thirdly, resonantly excited excitons by the probe laser seemed to have a severe influence on the measured spin relaxation time. In an attempt to minimize this effect, the probe laser power was reduced as much as technically feasible. However, further research is needed in order to identify the precise role of the probe illumination.

With the experimental setup described above, the Hanle effect was observed by measuring the Kerr rotation $\theta_K$ as function of the transverse magnetic field $B$. As described in chapter 2.8, the expected shape of $\theta_K(B)$ is a Lorentzian, and the spin lifetime $T_s(P_{\mathrm{Pump}})$ can be extracted from its width. The left panel of figure 4.3 shows a typical pump-power series of Hanle curves for sample E. From each curve, the half width $B_{1/2}(P_{\mathrm{Pump}})$ was extracted by a least-squares fit and plotted in the right panel as a function of the pump power. This pump power dependence of the Hanle half width was extrapolated linearly to $P_{\mathrm{Pump}} = 0$ in order to obtain the spin relaxation time $\tau_s$ for the undisturbed system.

For the calculation of spin relaxation times from measured Hanle data, the effective Landé $g$-factor must be known. For conduction electrons in GaAs, the commonly accepted value at liquid-helium temperature is $g = -0.44$ [Bla87]. This value changes very little in the temperature range between $4.2\,\mathrm{K}$ and $50\,\mathrm{K}$ [OHH$^+$96]. A slightly stronger dependence on the electron density was observed by OESTREICH *et al.* in the range between $10^{15}\,\mathrm{cm}^{-3}$ and $10^{17}\,\mathrm{cm}^{-3}$ [OHH$^+$96]. However, due to the large uncertainty on these data and the lack of independent comparative sources, a possible density dependence of the $g$-factor was not taken into account here. It is assumed that any residual influence of photoexcited electrons was eliminated by the extrapolation of the Hanle half width to zero power. Furthermore, the $g$-factor was assumed to be constant in the present work.

The experimental methods and techniques presented in this section were primarily employed to gain a deeper insight into spin dynamics in $n$-GaAs doped close to the MIT. However, the optically induced excitonic Kerr effect itself turned out to be worth of investigation. Although this effect is of fundamental importance for optical spin studies, it was not yet analyzed in detail. The following section discusses this topic.

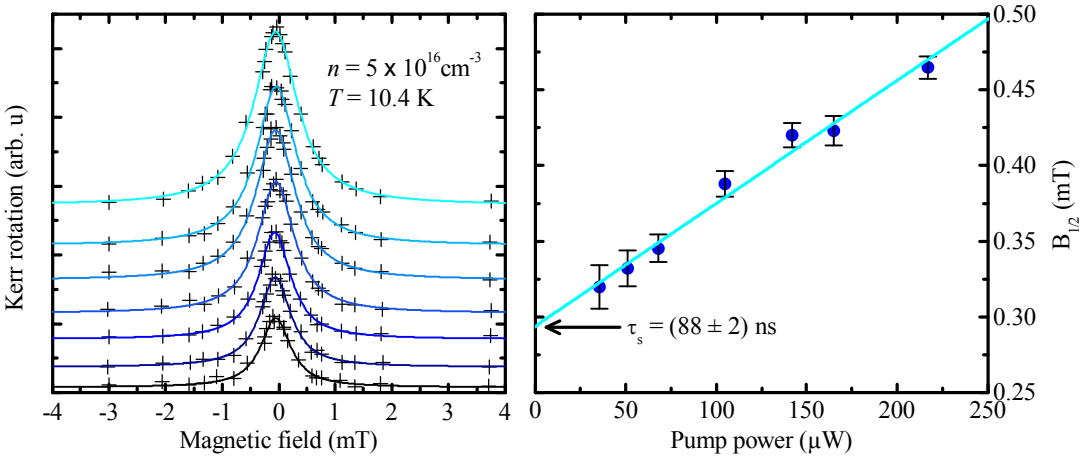


Figure 4.3: Typical example of a Hanle-MOKE pump power series. **(left)** Measured Hanle effect data (crosses) with least-squares fitted Lorentzians (solid curves). The data sets are shifted vertically for clarity. The pump power increases from the lowest to the top most curve. **(right)** Half width $B_{1/2}$ of the Lorentzian fits as function of the pump power. The linear extrapolation towards $P_{\mathrm{Pump}} = 0$ yields the spin relaxation time, which in this example is $\tau_s = 88 \pm 2\,\mathrm{ns}$.

## 4.2 Optically induced exciton Kerr effect

Traditionally, magneto-optic effects describe the interaction of polarized light with magnetic media. A magnetization $\boldsymbol{M}$ can be either intrinsic (ferromagnetic medium) or induced externally by a magnetic field $\boldsymbol{B}$ (paramagnetic medium). The polarization sensitive optical response is caused by the energy splitting of the electronic states with respect to the total angular momentum (spin and orbital). In the case of optically induced nonequilibrium conduction-electron spins, the macroscopic description of the magneto-optic effects, given in chapter 2.9, is still valid, but the microscopic interpretation is not straightforward. For example, the magnetization that could be ascribed to optically oriented spins is several orders of magnitude too small to cause a noticeable energy splitting.

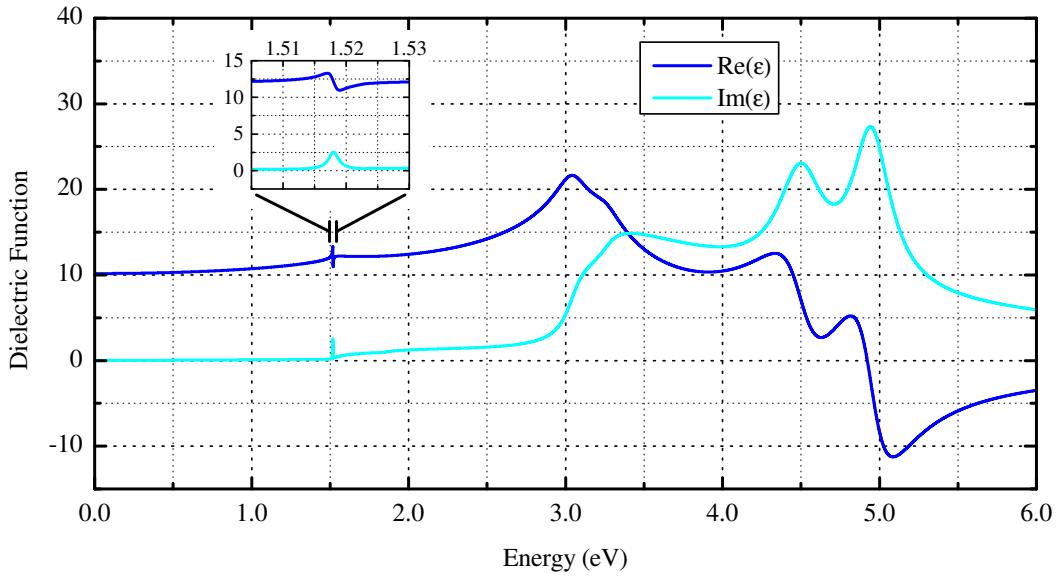


Figure 4.4: Calculated real and imaginary parts of the dielectric function of GaAs according to analytical expressions given in [Ada90]. The distinctive features are caused by critical point transitions (i.e. Van Hove singularities). The inset shows a close-up of the excitonic resonance at the $E_0$ critical point.

In the present chapter, the optically induced Kerr effect is studied in the spectral vincintiy of the exciton at the fundamental band gap. Figure 4.4 shows the dielectric function $\epsilon(\omega)$ of GaAs as obtained from analytical expressions given by S. ADACHI [Ada87, Ada90]. Here, the contribution of the exciton states at the fundamental band gap (small inset in the figure) is represented as a series of Lorentz oscillators

$$\epsilon_X(\omega) = \epsilon_0 + \sum_{n=1}^{\infty} A_X^n \left(E_0 + E_X^n - \hbar\omega - i\Gamma\right)^{-1} \tag{4.15}$$

where $E_0$ is the fundamental band-gap energy and $\Gamma$ is the broadening (damping) parameter. The

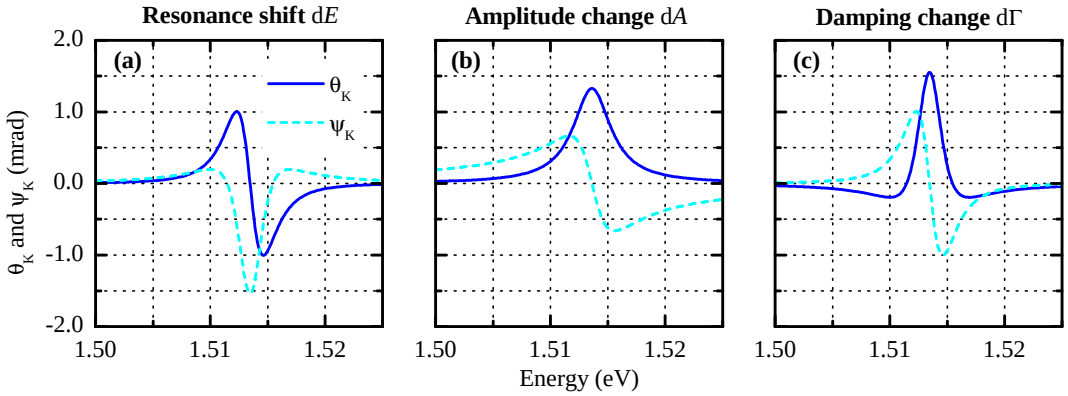


Figure 4.5: Calculated spectral dependence of the Kerr rotation $\theta_K$ and Kerr ellipticity $\psi_K$ for isolated changes of the Lorentz-oscillator parameters. **(a)** Simulated energetic shift of the resonance frequency $dE = \pm 100\,\mu eV$. **(b)** Simulated oscillator strength change $dA = \pm 100\,\mu eV$. **(c)** Simulated change of the damping $d\Gamma = \pm 100\,\mu eV$. The $\pm$ sign corresponds to the parameter change for left- and right-handed circular polarization, respectively. Note that the shape and amplitude also depends on the damping. In this case it was set to $\Gamma = 2.0\,meV$.

oscillator strength $A_X^n$ and the binding energy $E_X^n$ of the excited exciton states can be written

$$A_X^n = A_X^1/n^3 \tag{4.16}$$

$$E_X^n = -R_X^*/n^2 \tag{4.17}$$

where $R_X^*$ is the effective exciton Rydberg constant ($4.7\,meV$ in GaAs), $A_X^1 = 2.35\,meV$ [Ada90], and $\epsilon_0 = 11.95$ is the background permittivity. Within this approximation, the optically induced excitonic Kerr effect can be expressed as spin-dependent changes of the oscillator parameters $E_0$, $A_X^1$, and $\Gamma$. However, it must be noted in advance that no higher exciton states ($n > 1$) are observed in the experimental data presented here. Therefore, the following evaluation only uses the $n = 1$ contribution to the dielectric function.

The exction Kerr effect can be calculated from equations 2.25 and 2.26 by using expression 4.15 for the dielectric function. In order to obtain a non-zero Kerr rotation or ellipticity, one or more of the oscillator parameters must experience a polarization splitting. Figure 4.5 shows the spectral dependence of the Kerr rotation and ellipticity, as obtained for an energy splitting $dE$, a change of the oscillator strength $dA$, and a damping change $d\Gamma$, respectively.

Figure 4.6 shows experimentally measured Kerr-rotation spectra for samples A to F ($n_d$-series, see table A.1 on page 73). Although the spectral shape changes significantly with the doping concentration, all data are well approximated by the Lorentz-oscillator model described above. The parameters for the best fits are summarized in table 4.1. These data reveal a blue shift of the exciton energy and an increase of the damping with increasing doping concentration. However, although the spectral shape of the Kerr rotation spectrum changes systematically with the donor concentration, this behavior is not directly reflected in the doping dependence of the energy, amplitude and damping splittings. It

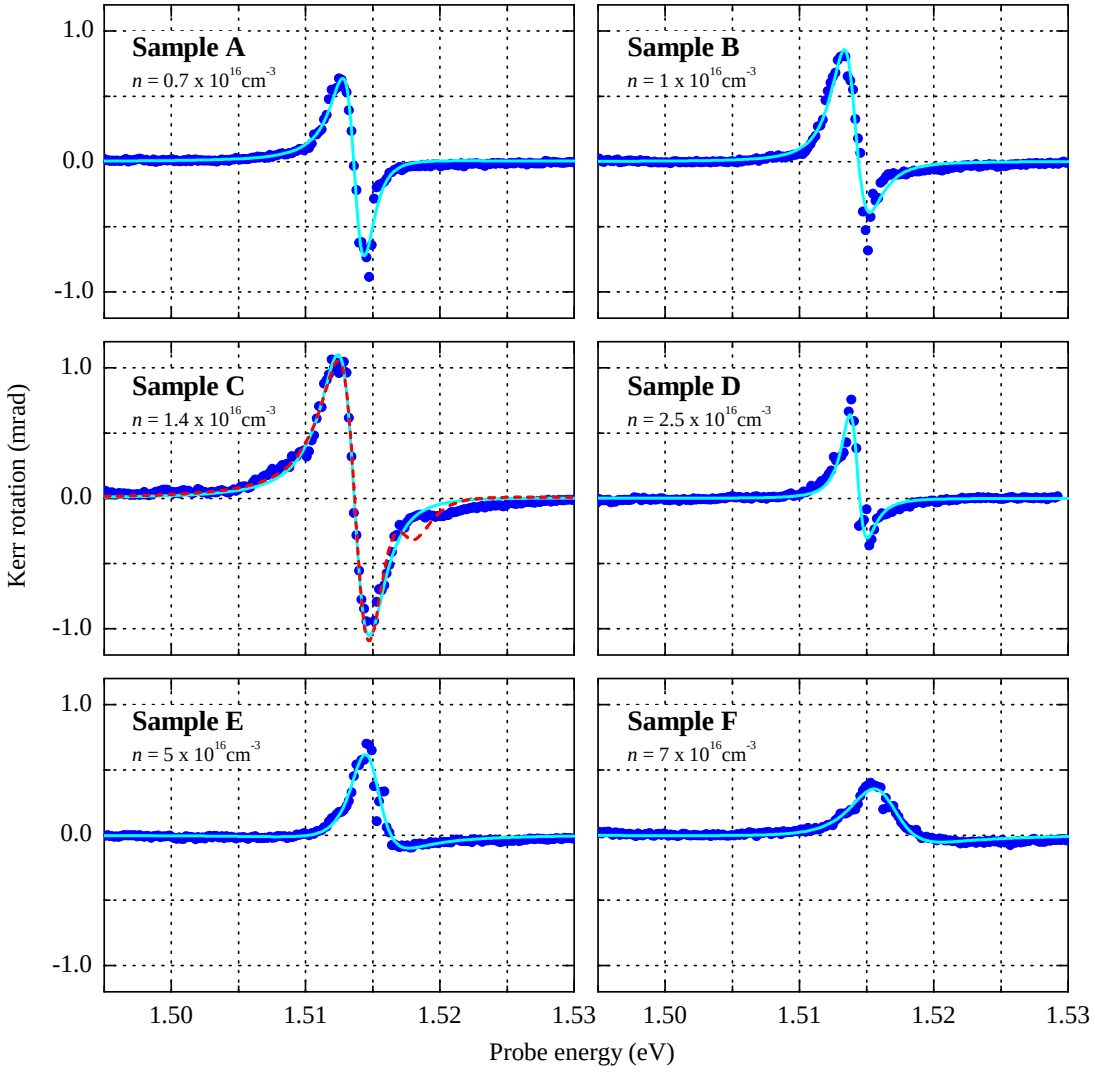


Figure 4.6: Spectral dependence of the Kerr rotation (Kerr fingerprint) of samples A to F at a bath temperature of $10\,\mathrm{K}$. All measured data are well described by the Lorentz-oscillator model. For sample C, the dashed curve shows the best fit of the Lorentz-oscillator model when excited exciton states are taken into account.

must also be noted that, although sample C nominally fits well into the series, it may deviate from any systematic behavior because it originates from a different MBE facility than the other samples.

All fits shown in figure 4.6 were obtained with only the $n = 1$ term of equation 4.15, because no contributions from higher exciton states were visible in most of the spectra. Only for sample C there is a feature at around $1.520\,\mathrm{eV}$ that might be associated with higher exciton states. The dashed line in this plot shows a best fit including higher order contributions (up to $n = 3$). In the presented form, the multi-oscillator model (equation 4.15) is unable to reproduce the observed feature correctly. However, FEHRENBACH *et al.* reported about a blue shift of the $n = 2$ exciton state under strong pho-

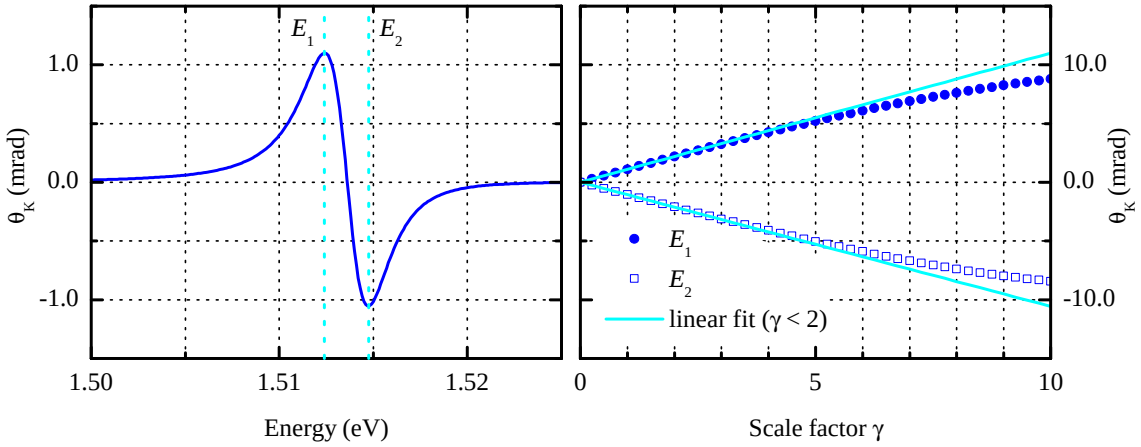


Figure 4.7: Linearity study of the exciton Kerr effect. **(left)** Calculated Kerr rotation spectrum for the best fit parameters of sample C. The vertical lines indicate the photon energies for which the linearity is investigated in the right panel, $E_1 = 1.5124\,\mathrm{eV}$ and $E_2 = 1.514\,75\,\mathrm{eV}$. **(right)** Dependence of the Kerr rotation on the scaling parameter $\gamma$ at the photon energies indicated in the left panel. The scaling factor indicates the common change of the oscillator parameters. $\gamma = 1$ yields the parameters as listed in table 4.1 for sample C. For $\gamma = 2$ the parameters $\mathrm{d}E$, $\mathrm{d}A$ and $\mathrm{d}\Gamma$ are doubled. The Kerr rotation spectrum shown on the left corresponds to $\gamma = 1$.

toexcitation [FSU85]. It was also shown in this publication that higher exciton states are suppressed in absorption spectra of thin layers ($\lesssim 2\,\mu\mathrm{m}$), while their contribution is observable in thicker layers. The doped layers of the investigated samples A to F have a thickness of $1\,\mu\mathrm{m}$, which could explain the absence of higher order exciton states in the measured Kerr rotation spectra.

Table 4.1: Fit parameters for the exciton Kerr rotation spectra shown in figure 4.6.

| Sample | $E_\mathrm{X}$ (meV) | $\Gamma$ (meV) | $\mathrm{d}E$ (meV) | $\mathrm{d}\Gamma$ (meV) | $\mathrm{d}A$ (meV) |
|---|---|---|---|---|---|
| A | 1.51359 | 1.37702 | -0.03125 | -0.01224 | -0.00754 |
| B | 1.51391 | 1.58306 | -0.0384 | 0.0064 | -0.01399 |
| C | 1.51354 | 2.007 | -0.10811 | -0.02122 | -0.0148 |
| D | 1.51409 | 1.06134 | -0.01315 | 0.0027 | -0.00617 |
| E | 1.51463 | 2.14719 | -0.01959 | 0.03536 | -0.00825 |
| F | 1.51605 | 3.36433 | -0.03187 | 0.04371 | -0.01038 |

The response of the exciton resonance to a spin imbalance $S$ can be understood in the following way. The fermionic nature of the electrons causes a repulsive potential among excitons. Therefore, an increase of the exciton density leads to an energetic blue shift and broadening as well as a reduction of the oscillator strength of the exciton states [FSU85]. According to the Pauli principle, these effects appear separately for each spin orientation. In the case of an excess of one spin species, the observed spin splitting of energy, damping and amplitude of the exciton resonance occurs.

The presence of donor atoms plays an important role for the excitonic Kerr effect, which is shown in the doping dependence of the Kerr rotation spectra in figure 4.6. In GaAs, the excitonic Kerr effect is most pronounced at doping densities around the metal-to-insulator transition. The reason is the strongly enhanced spin lifetime in this doping regime compared to higher and lower doping levels (see chapters 2.7 and 4.3). Above $\approx 2 \times 10^{16}\,\mathrm{cm}^{-3}$ the electronic donor wave functions begin to overlap and form an impurity band, which facilitates metallic conductivity (i.e. finite resistance at $T = 0$). Due to the fermionic nature of the electrons, the wave-function overlap leads to an energetic broadening and blue shift of the donor level. Essentially, this effect is very similar to the change of the exciton resonance with the exciton density. It is also comparable to the formation of anti-bonding molecular orbitals.

As elaborated in chapter 2.3, excitons and neutral donors have some formal similarities. Broadly speaking, the wave function of a conduction electron bound to a donor site is very similar to that of an electron bound to a valence-band hole. In phase space, donor-bound electrons and excitons compete for the same finite set of states, which leads to an interaction between both species. In combination with the rather long spin lifetime, spin-pumped donor electrons therefore give rise to the exciton Kerr effect in a very efficient way.

For quantitative spin studies by means of the exciton Kerr effect, it is important that the Kerr rotation signal scales linearly with the spin polarization $S_z$. Figure 4.7 illustrates the Kerr-rotation response to changes of the oscillator parameters. The left panel shows the best-fit Kerr rotation curve for sample C with the parameters listed in table 4.1. When the Kerr effect is employed as a tool for quantitative spin-polarization measurements, the spectral point with the largest response is usually chosen. In order to demonstrate the linearity, the right panel of figure 4.7 shows the Kerr rotation at the extrema of the spectral curve as a function of a scaling factor $\gamma$. This factor simply scales the values of $\mathrm{d}E$, $\mathrm{d}A$, and $\mathrm{d}\Gamma$ from table 4.1. It can be deduced from this plot that the response is in good approximation linear up to approximately five times the observed maximum signal of $\approx 1\,\mathrm{mrad}$.

This demonstrates that the Kerr response to changes of the oscillator parameters is sufficiently linear. However, it remained unclear at this point, how the oscillator parameters in turn respond to the spin polarization $S_z$. This relation was investigated in more detail later on by HENN *et al.* and published in [HHB$^+$13]. In essence, it was shown there that the exciton splitting energy is a good measure of the spin density, while the damping parameter reacts on changes of the electron temperature.

## 4.3 Electron spin relaxation

The spin relaxation time is a central parameter for the characterization of conduction-electron spins in semiconductors as described in chapter 2.6. For spin-based computing, the spin relaxation time determines the durability of potential spin memory in a given system. In the case of steady-state spin imaging, as in the present work, knowledge of the spin relaxation time is mandatory, in order to obtain information about diffusivity and mobility of conduction-electron spins from lateral spin-density profiles. However, the spin relaxation time is a highly nonmonotonic function of temperature and doping density. It is therefore advisable to determine the corresponding trends accurately prior to the evaluation of lateral spin drift and diffusion.

The doping dependence of electron spin relaxation in $n$-GaAs at the MIT was investigated in detail by DZHIOEV *et al.* for temperatures below 5 K [DKK$^+$02]. They were able to identify the relaxation mechanisms described in chapter 2.7. Another survey of the doping and temperature dependence of spin relaxation in $n$-GaAs was published by RÖMER *et al.* [RBM$^+$10]. They discussed in detail the interplay between localization and thermal activation for doping concentrations in a wide range around the MIT.

Figure 4.8 shows the temperature dependence of the spin relaxation time for samples B to F as determined by the Hanle-MOKE technique described in chapter 4.1.4. Due to the unavoidable presence of photoexcited carriers, the spin relaxation time of sample A could not be determined unambiguously with this method. This is a known issue for samples with low donor concentrations and discussed in [RBM$^+$10] and [CCS09]. For the other samples, it was possible to ensure that the measured spin relaxation times were not corrupted by photoexcitation [Hen11].

The spin relaxation times obtained for samples B to F at 10 K are in good quantitative agreement with data published by CROOKER *et al.* and RÖMER *et al.* [CCS09, RBM$^+$10]. The general temperature trend agrees mostly with the observations of RÖMER *et al.* except for sample B (see below). The inset in figure 4.8 shows the doping dependence of the spin relaxation time at 10 K. The trend here is similar to the picture drawn by DZHIOEV *et al.* (figure 2.9), although unfortunately in the present case only for 10 K the full doping trend data were available.

An interesting behavior is visible in the data for sample B in figure 4.8. For all other samples (C to F), the spin relaxation time decreases monotonically with rising temperature, while for sample B it first increases steeply and reaches a maximum at $\approx 12.5\,\mathrm{K}$. After that, it decays with further rising temperature like the other samples. A similar behavior was observed by FURIS *et al.* for an $n$-GaAs sample doped to $4 \times 10^{15}\,\mathrm{cm}^{-3}$ (figure 3d in [FSC06]). This nonmonotonic behavior is the result of enhanced averaging of the inhomogeneous nuclear fields due to thermal activation of donor electrons. The effect is very similar to the increase of the donor concentration in the regime of hyperfine

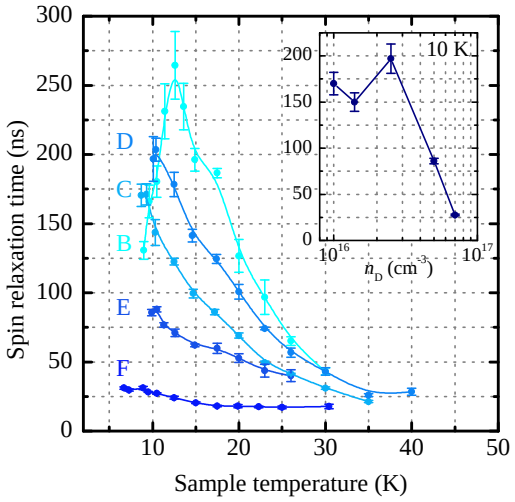


Figure 4.8: Temperature dependence of the spin relaxation time for the series of $n$-doped samples B to F obtained from Hanle-MOKE measurements. The lines only serve better visual orientation. The inset shows the doping dependence derived from these data at 10 K.

interaction as discussed in section 2.7 and [DKK$^+$02]. The example of sample B illustrates vividly that the spin relaxation time is a highly nonmonotonic function of temperature and doping in $n$-GaAs around the MIT. Therefore, it is rather difficult to compare data from different methods, samples and researchers despite nominally similar preconditions.

In the following section, the data summarized in figure 4.8 are used in the evaluation of lateral spin diffusion for this set of samples. Furthermore, these data help to establish a consistent picture of electron spin relaxation in $n$-GaAs at the MIT.

## 4.4 Hot-electron assisted spin diffusion

Spin transport properties of a given system are usually expressed in terms of a spin diffusivity $D_s$ and a spin mobility $\mu_s$. In combination with the spin relaxation time $\tau_s$ they determine how fast and how far nonequilibrium spin information can be transferred and how much it degrades on the way.

In order to determine the spin diffusivity of GaAs at the MIT, lateral spin density profiles were recorded for samples A to F with the scanning Kerr microscopy setup described in chapter 4.1. In the standard configuration, optical spin pumping was performed with an excitation wavelength of $\lambda_{\text{pump}} = 780\,\text{nm}$. The probe wavelength $\lambda_{\text{probe}}$ was adjusted to the low-energy peak of the respective Kerr-rotation spectrum for each sample and temperature (see figure 4.6). In order to ensure a linear response, it was verified that the peak signal scales proportionally with pump and probe power.

Due to the absence of external influences (magnetic field, electric field, strain, etc.) the shape of each measured spin profile was determined only by diffusion and relaxation of nonequilibrium spins. In order to extract the spin diffusivity $D_s$, the model given by equation 2.17 was evaluated numerically and fitted to each data set. Besides $D_s$, only a scaling factor $G_s^0$ and a small signal offset were adjusted for least-squares optimization. For each fit, the spin relaxation time $\tau_s$ was fixed to the corresponding value presented in section 4.3 for each sample and temperature. For sample A, the spin diffusivity could not be evaluated, due to the lack of reliable spin relaxation time data (see section 4.3).

Equation 2.17 was evaluated numerically in three spatial dimensions using a finite element solver. Due to the in-plane radial symmetry of the experimental situation, the solver was configured on a cylindrical domain. In contrast to the one dimensional evaluation presented in [FSK$^+$07], this approach allowed to take into account the vertical sample structure and light absorption. For all samples (B to F), the simulated domain was $1\,\mu\text{m}$ thick in accordance with the thickness of the epitaxial layers. The bottom interface to the intermediate AlGaAs barrier as well as the sample surface were represented by zero-flux boundary conditions. The radial size of the simulated domain was $250\,\mu\text{m}$ and the long-distance limit was represented by a Dirichlet boundary condition with a limiting value of zero.

The generation term was modeled in accordance with the lateral shape of the excitation laser as

$$G_s(r) = G_s^0 \, \exp\left(-\frac{r^2}{w_G^2} + \frac{z}{z_G}\right) \tag{4.18}$$

where $w_G = 1.7\,\mu\text{m}$ was fixed to the net optical resolution and the penetration depth $z_G$ varied from $0.7\,\mu\text{m}$ at $780\,\text{nm}$ to $1.4\,\mu\text{m}$ at $812.5\,\text{nm}$. Before fitting this model, each measured curve was centered

with the help of a second order polynomial fit of a small region around the maximum.

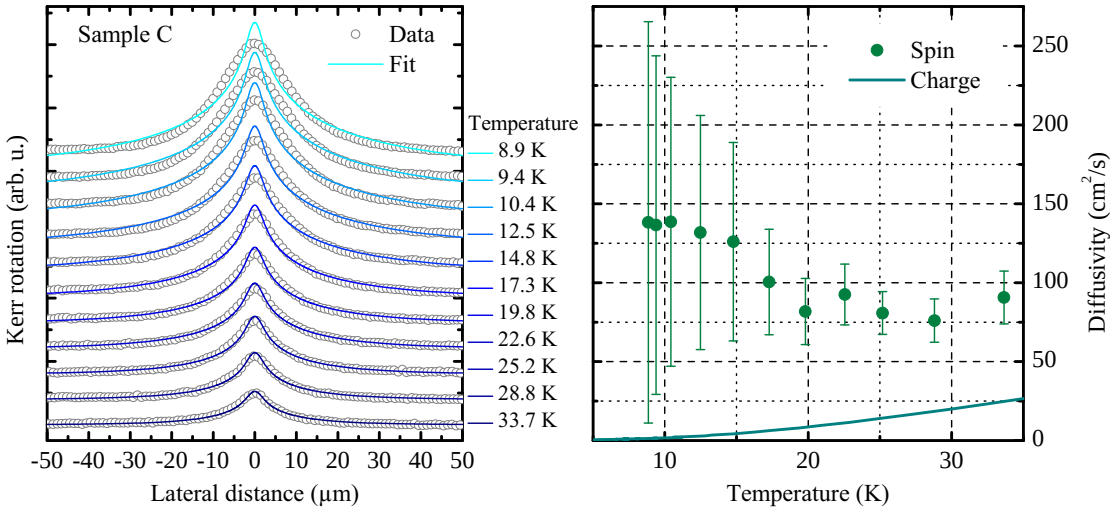


Figure 4.9: **(left)** Lateral spin density profiles measured for sample C (circles) with least-squares fitted profiles (lines) of the standard diffusion model (equation 2.17). Curves are shifted vertically for clarity. Temperature increases from top to bottom. **(right)** Spin diffusivity obtained from the fit and charge diffusivity calculated from electron-mobility data. The error bars indicate the 95% confidence interval calculated from the covariance matrix. As discussed in the text, this model does not describe the data very well.

Figure 4.9 shows a temperature series of lateral scans for sample C together with the corresponding fits of the model described above. The right panel of the figure shows the obtained spin diffusivities $D_s$ together with the electron (charge) diffusivity $D_c$.[1] As discussed earlier in this work, the agreement between data and model is not always satisfactory and yields extraordinarily large spin diffusivities. At temperatures around 30 K, the lateral profiles were reproduced adequately well, while deviations became increasingly pronounced for lower temperatures. However, even for high temperatures, where the fit appears to be reasonable, the obtained spin diffusivity is much larger than the corresponding charge diffusivity. One possible reason for this may be the presence of degeneracy in the conduction band.

Consequently, the systematic deviations between data and model make the fit insensitive with respect to the diffusivity. This is expressed by the large error bars in figure 4.9, which represent the 95% confidence interval calculated from the covariance matrix.

In order to investigate the systematic deviations produced by the standard diffusion model, figure 4.10 shows the summed residuals (squared differences) for all measured samples and temperatures. The data show that the deviations are largest for sample C, and decrease for both larger and smaller donor concentrations. In general, the residuals appear to be largest at the MIT and diminish into both

[1] See appendix B. The diffusivity $D_c$ was calculated from the Hall mobility via the Einstein relation for nondegenerate particles. Note that these values may underestimate the electron diffusivity in the case of degenerate conduction electrons.

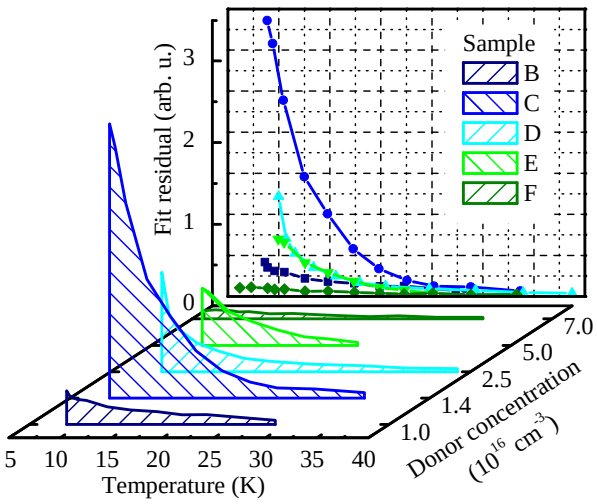


Figure 4.10: Residuals of the fit of equation 2.17 to lateral spin density profiles (see figure 4.9) for samples B to F at all measured temperatures. The residual is the sum of the squared differences between data and fit. Note that the residuals are largest, i.e. the agreement between fit and data is worst, close to the MIT at low temperatures.

adjoining regimes. On the temperature axis, the residuals decrease for all samples with rising temperature and disappear towards $\approx 30\,\mathrm{K}$. This point coincides with the transition between overheated and thermalized electrons in GaAs as discussed in chapter 2.4. Therefore, it stands to reason that local electron overheating is responsible for the observed deviations and the anomalously large spin diffusivities.

In order to obtain more realistic values for the spin diffusivity, the mathematical diffusion model was modified to include a lateral electron temperature gradient. In principle, there are two susceptible quantities in equation 2.17: the spin relaxation time $\tau_s$ and the spin diffusivity $D_s$. However, preliminary investigations showed that a lateral gradient in the spin relaxation time has almost no effect at all. The reason is that, close to the point of exctitation, the main contribution to the total spin loss is not the intrinsic spin relaxation but outdiffusion of spin polarized electrons. This assumption is also supported by local Hanle-effect data [QAO$^+$09]. In other words, electron spins do not stay long enough within the excitation spot to actually experience significant relaxation there. Instead, they diffuse away before they would take notice of a locally reduced spin relaxation time. Consequently, a homogeneous spin relaxation time $\tau_s$ is assumed to describe the spin system even in the presence of local electron overheating.

In contrast to the spin relaxation time, which is not influenced noticeably by the lateral electron temperature gradient, the spin diffusivity is altered massively in the vicinity of the excitation. The increased thermal energy of the electrons at the center of the excitation accelerates the diffusive outward motion. In principle, this effect can be considered as a kind of Seebeck effect.[2] Traditionally, the thermocurrent is related to the temperature gradient by the product of the electrical conductivity $\sigma$ and the Seebeck coefficient $S$. However, for the description of spin currents, these quantities are not available. As an alternative, the locally enhanced outward flow is interpreted as a local increase of the spin diffusivity $D_s$.

A usable parametrization of the lateral shape of $D_s(r)$ was constructed with the following assump-

[2]The Seebeck effect describes the appearance of an electrical current due to the presence of a thermal gradient.

tions. First, the lateral electron temperature profile follows a Gaussian. This is strongly suggested by the data shown in chapter 3. Secondly, the temperature dependence of the spin diffusivity is proportional to a power of the electron temperature in the range of interest. This would simply reflect the typical behavior of Brownian motion. Consequently, the spin diffusivity itself adopts the Gaussian shape of the temperature profile, but with a different lateral width.

The lateral shape of the spin diffusivity is modeled as

$$D_s(r) = D_s^0 \left(1 + A_D \exp\left[-\frac{r^2}{w_D^2}\right]\right) \tag{4.19}$$

The new parameters can be interpreted in the following way: $D_s^0$ is the *intrinsic* spin diffusivity, which would be expected in the undisturbed system as well as far away from the excitation. $A_D$ is an amplitude factor that describes the enhancement of the spin diffusivity due to the local disturbance. The decay length $w_D$ characterizes the length scale of the heating influence. Since none of these parameters were known *a priori*, reasonable approximations were found by a least-squares fit. The full diffusion model was obtained by inserting expression 4.19 into equation 2.17. Here, it is essential that the diffusivity and the nabla operator must not be permuted.

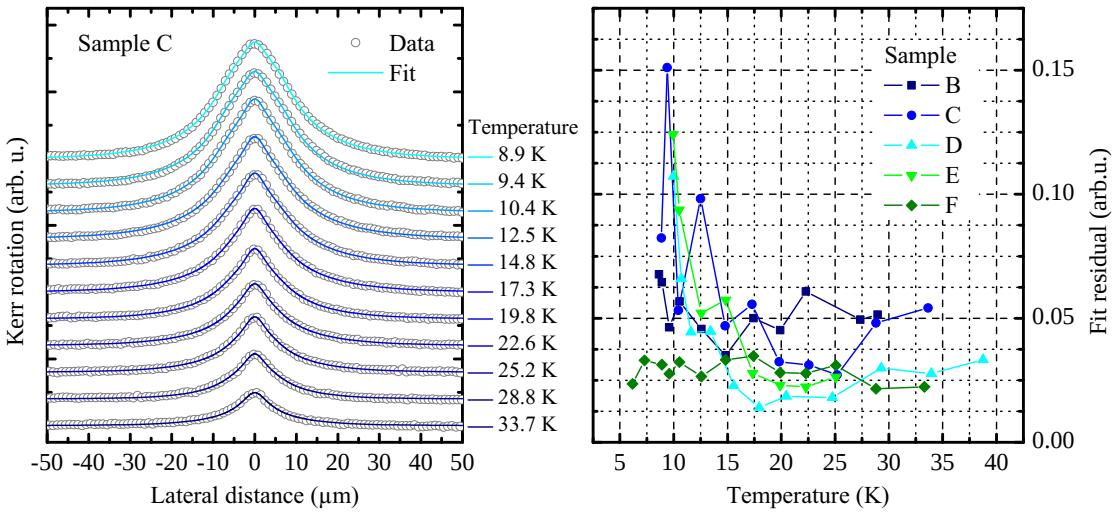


Figure 4.11: **(left)** Lateral spin density profiles of sample C with least-squares fitted curves of the modified diffusion model. **(right)** Fit residuals for samples B to F at all measured temperatures. Note that these residuals are more than an order of magnitude smaller than those of the standard diffusion model (figure 4.10).

Figure 4.11 shows the spin density profiles measured on sample C again, but this time with fitted curves from the modified diffusion model. The procedure to obtain the best fits was essentially the same as for the standard diffusion model, except for the new set of parameters. The agreement between data and fit was much better with this model, which is expressed quantitatively by the residuals shown in the right panel of the figure. The absolute values of the residuals were reduced by more than one order of magnitude. Moreover, the temperature trend was strongly diminished, which suggests

that this model effectively compensates for the influence of local electron heating.

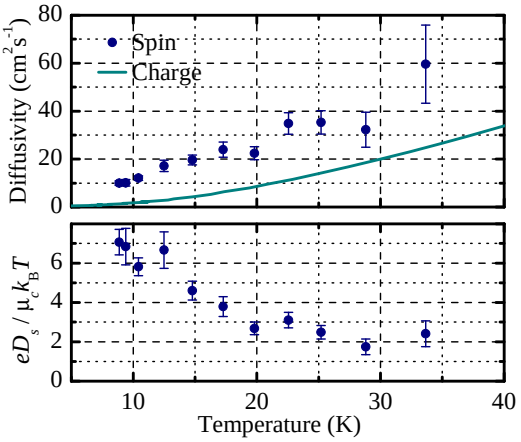


Figure 4.12: **(top)** Intrinsic spin diffusivity $D_s^0$ for sample C as obtained by the modified diffusion model. **(bottom)** Ratio between spin diffusivity and electron mobility.

The intrinsic spin diffusivity $D_s^0$ of sample C is shown in figure 4.12 together with the charge diffusivity obtained from the Hall mobility by application of the nondegenerate Einstein relation. First, the temperature trend of the spin diffusivity has changed fundamentally as compared to the data from the standard diffusion model in figure 4.9. Secondly, the uncertainties are much smaller. And thirdly, the values are much closer to the corresponding charge diffusivities. However, there is still a significant discrepancy between spin and charge diffusivities. As suggested earlier, this may be caused by electron degeneracy in the conduction band. For nondegenerate particles, the Einstein relation between diffusivity and mobility suggests that $eD = k_B T \mu$. However, depending on density and temperature, this relation must be modified for fermionic particles due to Pauli blocking. As alternative origins of a discrepancy between charge and spin transport, ambipolar diffusion or spin coulomb drag might be considered. However, both effects can be ruled out for several reasons in the present case of $n$-doped bulk GaAs.

Ambipolar diffusion describes the correlated transport of conduction electrons and valence holes due to the requirement of local charge neutrality. If electrons and holes are present in equal numbers, they must diffuse together. In this case, the total diffusivity is limited to that of the slower species, namely the holes. First of all, in the present experiments on $n$-doped GaAs, the number of photogenerated holes is negligible compared to the total number of conduction electrons. Consequently, the generated nonequilibrium spin polarization represents a single-band perturbation in the terminology of [FB00]. Secondly, ambipolar spin diffusion would perform at lower rates than expected from the classical Einstein relation, which is the opposite of the observations discussed here.

Spin coulomb drag, as presented for example in [DU10], can also be ruled out in the present case for two reasons: First, the electron densities were too low in the investigated bulk materials. Secondly, this effect would reduce the spin diffusivity, i.e. spin transport would be expected to perform slower than charge transport.

In order to investigate degeneracy as a possible cause of the enhanced spin diffusivity, figure 4.12 shows the ratio $eD_s/\mu_c k_B T$. For nondegenerate electrons, a ratio of one would be expected, if spin transport performed with the same mobility as electron transport. On the contrary, the observed values

are much larger than one for the lowest temperatures and decrease towards one with rising temperature. This trend is fully compatible with the thermal smearing of the Fermi edge. Furthermore no mechanism is known that would allow spins to propagate faster than the electrons. Therefore, electron degeneracy is the most probable candidate to explain the experimental observations.

Figure 4.13 provides further evidence to support the validity and physical significance of the proposed spin diffusion model. Here, lateral spin density profiles were measured for two different excitation conditions on sample C. In order to investigate the influence of the optical excess energy, $\lambda_{\text{pump}}$ was set to $780.0\,\text{nm}$ for high excess energy and $812.5\,\text{nm}$ for low excess energy, respectively.

For better comparison, the the raw spin profiles in figure 4.13 were normalized and shifted vertically. These data already revealed significant differences for different excitation conditions, which were most pronounced at low temperatures and vanished with rising temperature. The best fitting parameters in the right panel of the figure quantify these differences. Interestingly, the lateral width parameter $w_D$ remained almost constant for all temperatures and both excitation conditions. On the other hand, the diffusivity amplitude parameter $A_D$ showed a pronounced temperature dependence, which also changed strongly with varying optical energy. This suggests that the optical heating indeed

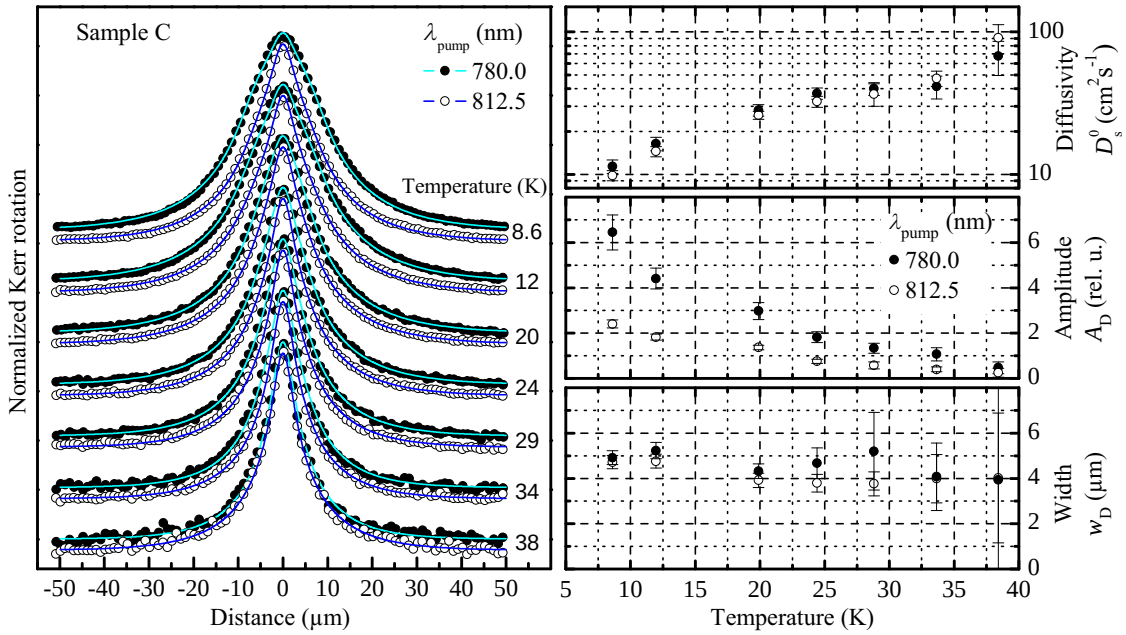


Figure 4.13: Influence of the excitation energy on spin diffusion for sample C. **(left)** Lateral spin density profiles with fits of the modified diffusion model for two different excitation wavelengths and several temperatures. Excitation with high and low excess energy was performed at $780.0\,\text{nm}$ and $812.5\,\text{nm}$ laser wavelength, respectively. **(right)** Fit parameters for these profiles. Note that the intrinsic diffusivity is robustly obtained from the modified diffusion model, regardless of the excitation condition. On the other hand, the local diffusivity enhancement ($A_D$) varies strongly, which reflects different overheating of electrons in both situations.

increases the spin diffusivity locally. On the temperature axis, the amplitude parameter $A_D$ decreased towards zero when approaching $\approx 40\,\mathrm{K}$. At low temperatures, $A_D$ diminished noticeably when the excess energy was reduced. Both findings are in perfect accordance with the picture of hot electron cooling presented in chapters 2.4 and 3.

But most importantly, the intrinsic spin diffusivity parameter $D_s^0$ did not vary beyond error bounds, when the excitation conditions were changed. This result is most satisfactory, because it strongly supports the confidence in these values as the true spin diffusivity of the undisturbed system.

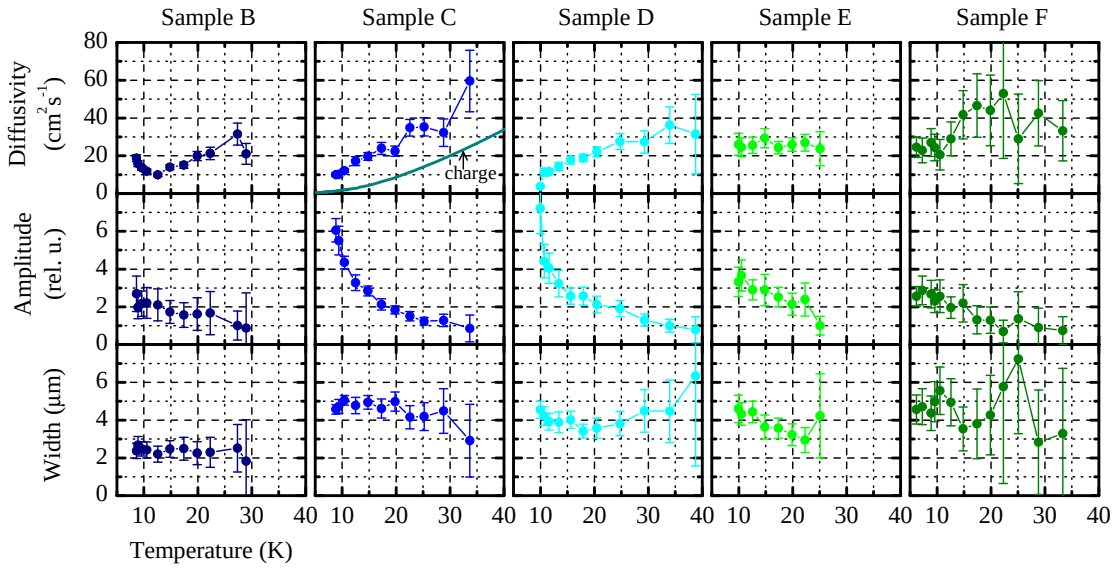


Figure 4.14: Fit parameter of the modified diffusion model for samples B to F (columns). **(top row)** Intrinsic spin diffusivity $D_s^0$. **(central row)** Diffusivity amplitude $A_D$. **(bottom row)** Lateral width of the diffusivity enhancement.

Figure 4.14 summarizes the best fitting parameters of the modified diffusion model for the whole doping series. Unfortunately, there were no charge transport data available for these samples, except for sample C. Therefore, only a few general remarks are possible about the obtained spin diffusivities. The temperature trends for samples C and D are very similar for all model parameters. Consequently, it stands to argue that both samples are governed in a similar way by degenerate electron diffusion, as discussed above for sample C. The temperature trends for samples B, E and F deviate noticeably from this picture. The spin diffusivity of sample B appears to assume a minimum at about $12.5\,\mathrm{K}$, while that of sample E seems to be constant over the entire temperature range. For sample F, the relatively large uncertainties allow various interpretations. There could be either an increase, like for samples C and D, or it could be approximately constant, like for sample E. The latter scenario appears more plausible because it would fit better to the overall trend. Summarizing, the temperature trend of the spin diffusivity begins at the lowest doping density with a peculiar minimum. It then shows a monotonic increase for the samples closest to the MIT and behaves constant for the samples clearly above the MIT.

Note that the minimum of the spin diffusivity of sample B occurred at the same temperature as the maximum of the corresponding spin relaxation time in figure 4.8. Despite all precautions, this could be an artifact due to the tendency of Hanle measurements to overestimate the spin relaxation time in low doped materials, as mentioned in chapter 4.1.4.

The central row of plot panels in figure 4.14 shows the temperature trends of the amplitude parameter $A_D$. Here, the picture is much clearer than for the spin diffusivities. For all samples, the general trend of this parameter was to decrease with temperature. The range of this decrease is compatible with the picture of hot electron cooling. However, for some samples (C and D) the slope of $A_D$ was more pronounced than for others. Again, the samples closest to the MIT reveal the strongest temperature trend.

Finally, the bottom row in figure 4.14 shows the lateral width parameter $w_D$ as a function of the bath temperature. Here, the overall tendency for all samples was to attain an almost constant value over the entire temperature range. The value varied from $\approx 2.5\,\mu\mathrm{m}$ for sample B to $\approx 5\,\mu\mathrm{m}$ for samples C and F. Samples D and E were situated around $\approx 4\,\mu\mathrm{m}$. The most remarkable feature of these data is the apparent jump between samples B and C.

To summarize the present chapter, it was first shown that the standard diffusion model is inadequate for the evaluation of optically induced electron spins in $n$-type GaAs and yields an inaccurate description of spin transport. This must have been at least partially responsible for the extraordinarily large spin diffusivities reported in the literature [KA99, FSK$^+$07]. Based on the insights about lateral electron temperature gradients in GaAs gained in chapter 3, the diffusion model was modified to account for the influence of hot electrons. This phenomenological approach yielded a much better agreement with the primary data and more realistic (smaller) spin diffusivities. The additional parameters could be interpreted in a physically meaningful way. They contain information about the spatial extent of the hot electron influence as well as the quality of the model itself. For one sample (C), it was furthermore possible to compare the obtained spin diffusivities with electron transport data. It turned out that the classical Einstein relation was still not fulfilled. However, the residual discrepancy between electron mobility and spin diffusivity could be explained by degeneracy in the conduction band. Finally, the spin diffusivity and the other model parameters were obtained as a function of the doping density and bath temperature. These data represent the first systematic characterization of spin diffusion in an undisturbed regime.

# 5 Conclusions and outlook

The goal of the present work was to illustrate the influence of hot electrons on spin spectroscopy in semiconductors. It was found that locally photoexcited conduction electrons are considerably overheated on length scales of several micrometers. This lateral electron-temperature gradient locally increases the diffusivity of electrons, and therefore modifies the shape of steady-state spin-density profiles with respect to the expectations drawn from a standard diffusion–relaxation model. As a consequence, the spin profiles calculated from the standard diffusion model do not reproduce the trend of experimental data under certain conditions. If in these cases this model is nevertheless used to evaluate experimental data, the obtained spin diffusivities will be systematically too large. Neglecting this influence of hot electrons is one important reason for the anomalously large spin diffusivities reported in the literature [KA99, CS05].

It was furthermore shown that the influence of the lateral electron-temperature gradient on the steady-state spin profile can be modeled as a local enhancement of the spin diffusivity. In this picture, the intrinsic spin diffusivity can be separated cleanly from the excess diffusivity due to electron overheating. With this modified model at hand, the spin diffusivity of bulk $n$-type GaAs was deduced from spin imaging experiments as a function of temperature and doping density. Together with the presented spin relaxation times, this survey represents a coherent set of data for spin dynamics in $n$-GaAs doped closely to the MIT.

Despite the correction for hot electron effects in the diffusion model, Einstein's relation is still not satisfied when comparing charge mobility and spin diffusivity at the MIT. In essence, electron spins appear to diffuse too fast for the corresponding electron mobilities. However, this apparent discrepancy can be explained by the fermionic nature of conduction electrons. When the electron concentration approaches the metallic regime, the electronic wave functions begin to overlap. In thermal equilibrium, electrons must then follow a Fermi-Dirac distribution, which leads to a different form of Einstein's relation as compared to the classical case of a Maxwell-Boltzmann distribution. In general, the ratio between diffusivity and mobility exceeds unity for degenerate particles. The experimental observations in the present work are fully consistent with this interpretation.

The numerical relation between spin diffusivity and electron mobility was successfully established for one medium-doped bulk GaAs sample of the investigated set. In order to verify the influence of degeneracy, it would be worthwhile to obtain further data on electrical transport in the remaining samples. However, all attempts to perform electrical measurements on these samples failed so far. Here, difficulties arose from the rather low doping concentrations which rendered it a non-trivial task to establish working electrical contacts to the bulk of the samples. Alternatively, electron diffusion could be investigated experimentally by means of a spatially resolved photoreflectance technique. A quick proof of principle was performed in the course of this work, which demonstrated that the local electron density can be probed by the change of reflectance on the exciton resonance. This effect is observed when non-spin-polarized electrons are excited and the reflectivity change is probed with linearly polarized light. The physical mechnanism is very similar to the excitonic MOKE described

in chapter 4.2. From such experiments, the electron diffusivity could be deduced in a similar way as the spin diffusivity was obtained from lateral spin density profiles. Of course, the lateral electron temperature gradient must be taken into account as well. Additionally, it must be checked carefully that the measured photoreflectance signal is linearly proportional to the local electron density. The full implementation of this method was unfortunately beyond the scope of this work.

In order to investigate the relation between lateral spin diffusion and the lateral electron-temperature gradient, two established methods of optical spectroscopy were implemented with microscopic lateral resolution: First, the scanning magneto-optic Kerr microscopy for spin detection and secondly, hyperspectral photoluminescence imaging for electron-temperature studies. In the course of this work, the scanning MOKE microscopy was technologically improved to provide a lateral resolution of about $1.7\,\mu\mathrm{m}$, compared to the previously achieved $\approx 4\,\mu\mathrm{m}$ [CS05, QAO$^+$09]. Additionally, a wavelength-tunable pump laser was introduced, which allowed to observe the influence of optical excess energy on spin dynamics. For photoluminescence studies, an optical resolution of about $4.5\,\mu\mathrm{m}$ was achieved with a LN2-cooled CCD multi-channel detector. The overall performance of this setup may be improved further by a review of the optical design in combination with a survey of currently available detectors. Furthermore, the optical cryostat should be replaced by one which allows a smaller working distance. The use of a larger NA objective could then improve the lateral resolution considerably. On the theoretical side, a coherent mathematical model might be formulated, which links electron thermodynamics with nonequilibrium spin dynamics in a more fundamental way as it was done with the phenomenologically motivated spin-diffusion model in the present work. However, the difficulty lies in the correct treatment of the highly non-linear dependencies of electron-phonon interaction on electron density and energy. Especially close to the MIT, where electron localization must be taken into account, and in the presence of local density and energy gradients, this becomes a rather complex problem.

Regarding optical spin detection, it is commonly assumed that the optically induced MOKE under spin pumping conditions is directly proportional to the nonequilibrium spin density. In an attempt to gain a better understanding of the origins of this effect, basic theoretical considerations and spectral MOKE measurements supported this assumption. However, later experiments performed by HENN *et al.* revealed that the excitonic MOKE is also affected by the presence of hot electrons [HHB$^+$13]. In essence, the exciton linewidth increases with the electron temperature, which manifests directly in optically induced MOKE spectra. By calibrating this effect against the bath temperature, it was furthermore possible to demonstrate a good agreement between the electron temperature obtained from MOKE measurements and that obtained from the conduction-band-to-acceptor (e,A$^0$) photoluminescence. On the downside, the thermal broadening of the exciton resonance reduces the absolute Kerr signal at any given probe wavelength. As a consequence, the lateral spin profile cannot be deduced reliably from the lateral MOKE signal alone. Instead, the lateral dependence of the exciton spin splitting energy should be analyzed, which can be obtained from the MOKE spectrum. It was shown in [HHB$^+$13] that the splitting energy gives the best measure of the local spin density. Despite the complexity of this method, the results obtained are fully consistent with the phenomenological spin diffusion model introduced in the present work.

Subsequently, the Kerr microscope presented here was equipped with a supercontinuum white light source that emits picosecond laser pulses [HKO$^+$13a]. By means of two independently tunable monochromator setups, the pump and the probe wavelengths were selectable in a wide range of visible and near infrared light. Moreover, by means of motorized delay stages, a temporal offset

between pump and probe pulses of up to $\approx 4\,\mathrm{ns}$ could be introduced. From time- and spectrally-resolved lateral spin imaging — which was newly facilitated by this setup — a more detailed picture of hot electron spin diffusion was drawn [HKO$^+$13b]. It followed from the data that spin diffusion is initially very fast, where the initial diffusivity depends strongly on the excitation excess energy. As electrons relax thermally, spin diffusion slows down with a time constant of $\approx 400\,\mathrm{ps}$. For very long times, the spin diffusivity then approaches an intrinsic value, which is again fully consistent with the results obtained from the phenomenological spin diffusion model in the present work.

Recent results obtained by GÖBBELS *et al.* also agree with the results presented here [GGB15]. They investigated the spatio-temporal evolution of spin packets in $n$-GaAs by time-resolved Faraday-rotation spectroscopy. In addition to optical spin pumping, a continuous-wave heating laser was used to introduce thermal energy into the electron system. Here, the authors interpreted the enhanced spin outflow due to the electron-temperature gradient in terms of a spin Seebeck effect and determined the value of the corresponding coefficient as $\approx 170\,\mu\mathrm{V\,K^{-1}}$. It was discussed in chapter 4.4 of the present work that the observed effect of thermally driven spin diffusion can also be interpreted as a spin Seebeck effect. However, more importantly the authors of [GGB15] verified the validity of the non-classical Einstein's relation for moderately doped $n$-GaAs at low temperatures and thereby confirmed that electron degeneracy causes the residual discrepancy between electron mobility and spin diffusivity as discussed in chapter 4.4.

To summarize, the influence of hot electrons on optical spin imaging at low temperatures must not be neglected. The phenomenological hot-electron compensation for the spin diffusion model introduced in this work presents an easy way to obtain much better results as compared to the commonly used standard diffusion model, where the influence of hot electrons is not accounted for at all.

Finally, it must be noted that low-temperature spin diffusion is only one example where the subtle but significant influence of hot electrons is responsible for systematically inaccurate results. Not only in optical spectroscopy, but also in electrical transport experiments, the possibility of electron overheating should always be taken into account in order to avoid dubious interpretation of experimental data.

# A Sample materials

The experimental results of the present work were obtained on a series of increasingly doped $n$-type GaAs epitaxial layers (samples A to F) and two high purity GaAs layers (samples G and H). Their key properties are summarized in table A.1.

Table A.1: Summary of the investigated samples.

| Sample | Designation | Conductivity | $\lvert N_D - N_A \rvert$ ($\mathrm{cm}^{-3}$) | Thickness (µm) | Growth method |
|---|---|---|---|---|---|
| A | M3330 | n | $0.7 \times 10^{16}$ | 1.0 | MBE |
| B | M3331 | n | $1.0 \times 10^{16}$ | 1.0 | MBE |
| C | 11889 | n | $1.4 \times 10^{16}$ | 1.0 | MBE |
| D | M3332 | n | $2.5 \times 10^{16}$ | 1.0 | MBE |
| E | M3333 | n | $5.0 \times 10^{16}$ | 1.0 | MBE |
| F | M3334 | n | $7.0 \times 10^{16}$ | 1.0 | MBE |
| G | R333 | p | $2 \times 10^{13}$ | 70 | LPE |
| H | R291 | n | $3 \times 10^{13}$ | 70 | LPE |

Samples A to F were grown by molecular beam epitaxy (MBE). These samples, except for sample C, were provided by the Lehrstuhl für Technische Physik at the University of Würzburg. Sample C was provided by the Lehrstuhl für Angewandte Festkörperphysik at the University of Bochum. Samples G and H were grown by liquid phase epitaxy (LPE) and originate from the Max-Planck-Institut für Festkörperforschung in Stuttgart.

# B Electron mobility data

The electrical transport properties of sample C were measured by A. WIECK at the University of Bochum by the Van der Pauw method. The electron mobility obtained from these data is shown in figure B.1.

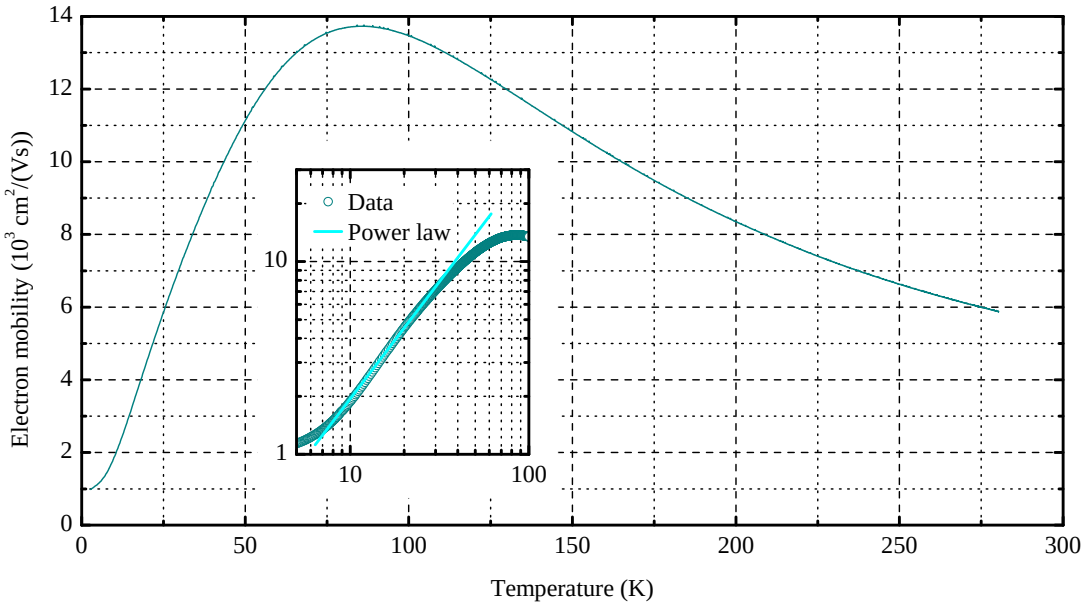


Figure B.1: Conduction electron mobility of sample C measured by the Van der Pauw method by A. WIECK at the University of Bochum. The inset shows the low-temperature range on a log-log scale to illustrate that the data can be approximated by a power law in a limited temperature interval.

# C List of physical quantities and material parameters

Table C.1: Summary of numerical values for selected physical quantities and material parameters. These values can be found in many text books and material specific encyclopedias like [Bla82] and [YC10].

| Symbol | Value | description |
|---|---|---|
| $e$ | $1.6 \times 10^{-19}\,\mathrm{C}$ | elementary charge |
| $\hbar$ | $1.05 \times 10^{-34}\,\mathrm{J\,s}$ | reduced Planck's constant |
| $k_B$ | $1.38 \times 10^{-23}\,\mathrm{J\,K^{-1}}$ | Boltzmann's constant |
| $\epsilon$ | $8.85 \times 10^{-12}\,\mathrm{C\,V^{-1}\,m}$ | vacuum dielectric constant |
| $m_0$ | $9.11 \times 10^{-31}\,\mathrm{kg}$ | free electron mass |
| $m_e$ | $0.067 m_0$ | GaAs conduction electron effective mass |
| $m_{hh}$ | $0.51 m_0$ | GaAs heavy hole effective mass |
| $m_{lh}$ | $0.08 m_0$ | GaAs light hole effective mass |
| $\epsilon_0$ | $12.5$ | GaAs DC dielectric constant |
| $\epsilon_\infty$ | $10.9$ | GaAs high frequency dielectric constant |
| $e_{14}$ | $0.16\,\mathrm{C\,m^{-2}}$ | GaAs piezoelectric coupling constant |
| $E_{\mathrm{LO},\Gamma}$ | $36\,\mathrm{meV}$ | GaAs LO phonon energy at $k = 0$ |

# Bibliography


[AB77] R.M.A. Azzam and N.M. Bashara. Ellipsometry and polarized light. North-Holland personal library. North-Holland Pub. Co., 1977.

[Ada87] S. Adachi. Model dielectric constants of GaP, GaAs, GaSb, InP, InAs, and InSb. Phys. Rev. B, 35(14):7454–7463, 1987.

[Ada90] S. Adachi. Excitonic effects in the optical spectrum of GaAs. Phys. Rev. B, 41(2):1003–1013, 1990.

[AS65] M. Abramowitz and I. A. Stegun, editors. Handbook of mathematical functions with formulas, graphs, and mathematical tables. Dover Publications, Inc., New York, 1965.

[AS73] D. E. Aspnes and A. A. Studna. Schottky-barrier electroreflectance: Application to GaAs. Phys. Rev. B, 7:4605–4625, 1973.

[Bal98] N. Balkan. Hot electrons in semiconductors: physics and devices. Number 5. Oxford University Press, 1998.

[BAP75] G. I. Bir, A. G. Aronov, and G. E. Pikus. Spin relaxation of electrons scattered by holes. Zh. Eksp. Teor. Fiz., 69:1382–1397, 1975.

[Bla82] J. S. Blakemore. Semiconducting and other major properties of gallium arsenide. Journal of Applied Physics, 53:123, 1982.

[Bla87] J. S. Blakemore, editor. Gallium Arsenide. American Institute of Physics, New York, 1987.

[Blo46] F. Bloch. Nuclear induction. Phys. Rev., 70:460, 1946.

[CAS95] S.A. Crooker, D.D. Awschalom, and N. Samarth. Time-resolved faraday rotation spectroscopy of spin dynamics in digital magnetic heterostructures. Selected Topics in Quantum Electronics, IEEE Journal of, 1(4):1082–1092, 1995.

[CC76] J. R. Chelikowsky and M. L. Cohen. Nonlocal pseudopotential calculations for electronic-structure of 11 diamond and zincblende semiconductors. Physical Review B, 14(2):556–582, 1976.

[CCC06] S. G. Carter, Z. Chen, and S. T. Cundiff. Optical measurement and control of spin diffusion in n-doped GaAs quantum wells. Phys. Rev. Lett., 97(13):136602, 2006.

[CCS09] S. Crooker, L. Cheng, and D. Smith. Spin noise of conduction electrons in n-type bulk GaAs. Phys. Rev. B, 79(3):035208, 2009.

[CFL+05] S. A. Crooker, M. Furis, X. Lou, C. Adelmann, D. L. Smith, C. J. Palmstrom, and P. A. Crowell. Imaging spin transport in lateral ferromagnet/semiconductor structures. Science, 309(5744):2191, 2005.

[CFL+07] S. A. Crooker, M. Furis, X. Lou, P. A. Crowell, D. L. Smith, C. Adelmann, and C. J. Palmstrøm. Optical and electrical spin injection and spin transport in hybrid Fe/GaAs devices. Journal of Applied Physics, 101(8), 2007.

[CS05] S. A. Crooker and D. Smith. Imaging spin flows in semiconductors subject to electric, magnetic, and strain fields. Phys. Rev. Lett., 94(23):236601, 2005.

[DKK+02] R. Dzhioev, K. Kavokin, V. Korenev, M. Lazarev, B. Meltser, M. Stepanova, B. Zakharchenya, D. Gammon, and D. Katzer. Low-temperature spin relaxation in n-type GaAs. Phys. Rev. B, 66(24):245204, 2002.

[DP71] M. I. Dyakonov and V. I. Perel. Spin relaxation of conduction electrons in noncentrosymmetric semiconductors. Fiz. Tverd. Tela, 13:3581–3585, 1971.

[Dre55] G. Dresselhaus. Spin-orbit coupling effects in zinc blende structures. Phys. Rev., 100(2):580–586, 1955.

[DU10] I. D'Amico and C. A. Ullrich. Coulomb interactions and spin transport in semiconductors: The spin Coulomb drag effect. physica status solidi (b), 247(2):235–247, 2010.

[DV00] I. D'Amico and G. Vignale. Theory of spin Coulomb drag in spin-polarized transport. Phys. Rev. B, 62(8):4853–4857, 2000.

[DV01] I. D'Amico and G. Vignale. Spin diffusion in doped semiconductors: The role of Coulomb interactions. Europhys. Lett., 55:566, 2001.

[DV02] I. D'Amico and G. Vignale. Coulomb interaction effects in spin-polarized transport. Phys. Rev. B, 65(8), 2002.

[Ehr60] H. Ehrenreich. Band structure and electron transport of GaAs. Phys. Rev., 120:1951–1963, 1960.

[EL87] S.E. Esipov and Y.B. Levinson. The temperature and energy distribution of photoexcited hot electrons. Advances in Physics, 36(3):331–383, 1987.

[Ell54] R. J. Elliott. Theory of the effect of spin-orbit coupling on magnetic resonance in some semiconductors. Phys. Rev., 96(2):266–279, 1954.

[ES70] A. I. Ekimov and V. I. Safarov. Optical orientation of carriers in interband transitions in semiconductors. Zh. Eksp. Teor. Fiz., 12:293–297, 1970.

[Far33] M. Faraday. Faraday's Diary, volume IV. London: George Bell and Sons, Ltd., 1933.

[FB00] M. E. Flatté and J. M. Byers. Spin diffusion in semiconductors. Phys. Rev. Lett., 84(18):4220–4223, 2000.

[FMAE+07] J. Fabian, A. Matos-Abiague, C. Ertler, P. Stano, and I. Žutić. Semiconductor spintronics. Acta Phys. Slov., 57(4 and 5):565–907, 2007.

[Frö43] H. Fröhlich. Theory of dielectric breakdown. Nature (Lond.), 151:339, 1943.

[FSC06] M. Furis, D. L. Smith, and S. A. Crooker. Bias-dependent electron spin lifetimes in n-GaAs and the role of donor impact ionization. Appl. Phys. Lett., 89:102102–102104, 2006.

[FSK+07] M. Furis, D. L. Smith, S. Kos, E. S. Garlid, K. S. M. Reddy, C. J. Palmstrom, P. A. Crowell, and S. A. Crooker. Local Hanle-effect studies of spin drift and diffusion in n:GaAs epilayers and spin-transport devices. New J. Phys., 9:347, 2007.

[FSU85] G. W. Fehrenbach, W. Schäfer, and R. G. Ulbrich. Excitonic versus plasma screening in highly excited gallium arsenide. J. Luminesc., 30(1-4):154–161, 1985.

[GES71] D. Z. Garbuzov, A. I. Ekimov, and V. I. Safarov. Measurement of the Lifetime and of the Spin-relaxation Time of Electrons in Semiconductors by the Optical-orientation Method. ZhETF Pisma Redaktsiiu, 13:36, 1971.

[GGB15] S. Göbbels, G. Güntherodt, and B. Beschoten. Hot-electron driven lateral spin Seebeck transport of optically generated spin packets in n-GaAs. ArXiv e-prints, 2015.

[GH78] E. O. Goebel and O. Hildebrand. Thermalization of the electron—hole plasma in GaAs. physica status solidi (b), 88(2):645–652, 1978.

[GOD+88] S. Geschwind, A. T. Ogielski, G. Devlin, J. Hegarty, and P. Bridenbaugh. Activated dynamic scaling and magnetic ordering in $Cd_{1-x}Mn_xTe$: Spin glass or random antiferromagnet? (invited). Journal of Applied Physics, 63(8):3291–3296, 1988.

[GS22] W. Gerlach and O. Stern. Der experimentelle Nachweis der Richtungsquantelung im Magnetfeld. Z. Phys., 9:349–352, 1922.

[HA10] B. Huang and I. Appelbaum. Time-of-flight spectroscopy via spin precession: The larmor clock and anomalous spin dephasing in silicon. Phys. Rev. B, 82(24):241202, 2010.

[Han24] W. Hanle. Über magnetische Beeinflussung der Polarisation der Resonanzfluoreszenz. Zeitschrift für Physik, 30(1):93–105, 1924.

[Hen11] T. Henn. Lateral Spin Diffusion in n-type Gallium Arsenide. Universität Würzburg, Diplomarbeit, Universität Würzburg, Fakultät für Physik und Astronomie, Am Hubland, 97074 Würzburg, 2011.

[HH74] U. Heim and P. Hiesinger. Luminescence and excitation spectra of exciton emission in GaAs. physica status solidi (b), 66(2):461–470, 1974.

[HHB+13] T. Henn, A. Heckel, M. Beck, T. Kiessling, W. Ossau, L. W. Molenkamp, D. Reuter, and A. D. Wieck. Hot carrier effects on the magneto-optical detection of electron spins in GaAs. Phys. Rev. B, 88:085303, 2013.

[HKO+13a] T. Henn, T. Kiessling, W. Ossau, L. W. Molenkamp, K. Biermann, and P. V. Santos. Ultrafast supercontinuum fiber-laser based pump-probe scanning magneto-optical kerr effect microscope for the investigation of electron spin dynamics in semiconductors at cryogenic temperatures with picosecond time and micrometer spatial resolution. Review of Scientific Instruments, 84(12), 2013.

[HKO+13b] T. Henn, T. Kiessling, W. Ossau, L. W. Molenkamp, D. Reuter, and A. D. Wieck. Picosecond real-space imaging of electron spin diffusion in GaAs. Phys. Rev. B, 88:195202, 2013.

[HRP94] A. P. Heberle, W. W. Rühle, and K. Ploog. Quantum beats of electron larmor precession in GaAs wells. Phys. Rev. Lett., 72:3887–3890, 1994.

[Jon41] R. C. Jones. A new calculus for the treatment of optical systems. J. Opt. Soc. Am., 31(7):488–493, 1941.

[KA98] J. M. Kikkawa and D. D. Awschalom. Resonant spin amplification in n-type GaAs. Phys. Rev. Lett., 80(19):4313–4316, 1998.

[KA99] J. M. Kikkawa and D. D. Awschalom. Lateral drag of spin coherence in gallium arsenide. Nature, 397(6715):139, 1999.

[Kau93] V. Kaufman. Wavelengths and energy levels of neutral $Kr^{84}$ and level shifts in all Kr even isotopes. Journal of research of the National Institute of Standards and Technology, 98(6), 1993.

[Kav01] K. Kavokin. Anisotropic exchange interaction of localized conduction-band electrons in semiconductors. Phys. Rev. B, 64(7):075305, 2001.

[Kav08] K. V. Kavokin. Spin relaxation of localized electrons in n-type semiconductors. Semicond. Sci. Technol., 23:114009, 2008.

[Kem69] J. C. Kemp. Piezo-optical birefringence modulators: new use for a long-known effect. J. Opt. Soc. Am., 59(8):950–953, 1969.

[Ker76] J. Kerr. On the magnetisation of light and the illumination of magnetic lines of force. Rep. Brit. Ass. S, 5:85, 1876.

[Kog63] Sh. M. Kogan. On the theory of hot electrons in semiconductors. Soviet Physics - Solid State, 4(9):1813, 1963.

[KSSA97] J. M. Kikkawa, I. P. Smorchkova, N. Samarth, and D. D. Awschalom. Room-temperature spin memory in two-dimensional electron gases. Science, 277(5330):1284–1287, 1997.

[LK34] L. D. Landau and A. Kompanejez. Z. Phys. Sovjetunion, 1934.

[Lyo86] S.A. Lyon. Spectroscopy of hot carriers in semiconductors. Journal of Luminescence, 35(3):121 – 154, 1986.

[MORH10] G. M. Müller, M. Oestreich, M. Römer, and J. Hübner. Semiconductor spin noise spectroscopy: Fundamentals, accomplishments, and challenges. Physica E: Low-dimensional Systems and Nanostructures, 43(2):569 – 587, 2010.

[MS81] H. Münzel and A. Steckenborn. Hot electrons in cold semiconductors: GaAs, InP and CdTe. J. Luminesc., 1981.

[MSDW76] J. B. Mullin, B. W. Straughan, C. M. H. Driscoll, and A. F. W. Willoughby. Lattice superdilation phenomena in doped GaAs. Journal of Applied Physics, 47(6):2584–2587, 1976.

[MZ84] F. Meier and B. P. Zakharchenya, editors. Optical Orientation, volume 8 of Modern Problems in Condensed Matter Sciences. North-Holland, Amsterdam, 1984.

[OHH+96] M. Oestreich, S. Hallstein, A. P. Heberle, K. Eberl, E. Bauser, and W. W. Rühle. Temperature and density dependence of the electron Landé g factor in semiconductors. Phys. Rev. B, 53(12):7911–7916, 1996.

[OR95] M. Oestreich and W. W. Rühle. Temperature dependence of the electron Landé g factor in GaAs. Phys. Rev. Lett., 74(12):2315–2318, 1995.

[ORHH05] M. Oestreich, M. Römer, R. Haug, and D. Hägele. Spin Noise Spectroscopy in GaAs. Phys. Rev. Lett., 95(21), 2005.

[Par69] R. R. Parsons. Band-to-band optical pumping in solids and polarized photoluminescence. Phys. Rev. Lett., 23(20):1152–1154, 1969.

[Pau27] W. Pauli. Zur Quantenmechanik des magnetischen Elektrons. Zeitschrift für Physik, 43(9-10):601–623, 1927.

[QAO+08] J.-H. Quast, G. V. Astakhov, W. Ossau, L. W. Molenkamp, J. Heinrich, S. Höfling, and A. Forchel. Lateral spin diffusion probed by two-color Hanle-MOKE technique. Acta Physica Polonica A, 114(5):1311–1316, 2008.

[QAO+09] J.-H. Quast, G. V. Astakhov, W. Ossau, L. Molenkamp, J. Heinrich, S. Höfling, and A. Forchel. Influence of light on spin diffusion in weak magnetic fields. Phys. Rev. B, 79(24):245207, 2009.

[Qua07] J.-H. Quast. Imaging of spins by magneto optical Kerr microscopy. Universität Würzburg, Diplomarbeit, Universität Würzburg, Fakultät für Physik und Astronomie, Am Hubland, 97074 Würzburg, 2007.

[RBM+10] M. Römer, H. Bernien, G. Müller, D. Schuh, J. Hübner, and M. Oestreich. Electron-spin relaxation in bulk GaAs for doping densities close to the metal-to-insulator transition. Phys. Rev. B, 81(7):075216, 2010.

[Say08] F. J. Sayas. A gentle introduction to the finite element method, 2008.

[SD90] D. Strauch and B. Dorner. Phonon dispersion in GaAs. Journal of Physics: Condensed Matter, 2(6):1457, 1990.

[Sei49] F. Seitz. On the theory of electron multiplication in crystals. Phys. Rev., 76:1376–1393, 1949.

[SL69] J. Shah and R. C. C. Leite. Radiative recombination from photoexcited hot carriers in GaAs. Phys. Rev. Lett., 22:1304–1307, 1969.

[SM81] B. Stébé and G. Munschy. Fine structure of neutral-acceptor bound excitons in direct gap semiconductors with zinc blende structure. Solid State Communications, 40(6):663–667, 1981.

[SPW97] M. Seck, M. Potemski, and P. Wyder. High-field spin resonance of weakly bound electrons in GaAs. Phys. Rev. B, 56(12):7422–7427, 1997.

[Tor56] H. C. Torrey. Bloch equations with diffusion terms. Phys. Rev, 104(3):563–565, 1956.

[Ulb73] R. Ulbrich. Energy relaxation of photoexcited hot electrons in GaAs. Phys. Rev. B, 8(12):5719–5727, 1973.

[Var67] Y. P. Varshni. Temperature dependence of the energy gap in semiconductors. Physica, 34(1):149 – 154, 1967.

[WGM+05] C. P. Weber, N. Gedik, J. E. Moore, J. Orenstein, J. Stephens, and D. D. Awschalom. Observation of spin Coulomb drag in a two-dimensional electron gas. Nature, 437(7063):1330–1333, 2005.

[WH77] C. Weisbuch and C. Hermann. Optical detection of conduction-electron spin resonance in GaAs, $Ga_{1-x}In_xAs$, and $Ga_{1-x}Al_xAs$. Phys. Rev. B, 15:816–822, 1977.

[Wil75] J. D. Wiley. Semiconductors and Semimetals, 10:91, 1975.

[Yaf63] Y. Yafet. Solid State Physics, volume 14. Academic Press, New York, 1963.

[YC10] P. Y. Yu and M. Cardona. Fundamentals of Semiconductors: Physics and Materials Properties. Springer, Berlin, Heidelberg, 2010.

[Zee97] P. Zeeman. The Effect of Magnetisation on the Nature of Light Emitted by a Substance. Nature, 55:347, 1897.

[ŽFS04] I. Žutić, J. Fabian, and S. Das Sarma. Spintronics: Fundamentals and applications. Rev. Mod. Phys., 76(2):323–410, 2004.